Spatiotemporal Scales of the Deep Circulation in the Eastern Gotland Basin/ Baltic Sea

Dissertation
zur
Erlangung des akademischen Grades
doctor rerum naturalium (Dr. rer. nat.)
der Mathematisch-Naturwissenschaftlichen Fakultät
der Universität Rostock

vorgelegt von
Gunda Wieczorek
geb. am 3.6.1975 in Münster
aus Glasgow

Glasgow, April 2011

urn:nbn:de:gbv:28-diss2012-0107-1

Die vorliegende Arbeit wurde am 2. Mai 2011 bei der Mathematisch-Naturwisschaftlichen Fakultät der Universität Rostock als Dissertation eingereicht und am 25. Mai 2012 erfolgreich verteidigt.

Die Gutachter waren:

- Dr. habil. Eberhard Hagen, Leibniz Institut für Ostseeforschung Warnemünde
- Prof. Dr. Jüri Elken, Tallinn University of Technology

Abstract

The Baltic Sea is surrounded by land, thus exchanges with the open ocean only take place through the North Sea. The Baltic Sea is divided into different deep basins connected by narrow sills and channels. Compared to the open ocean and the North Sea the salinity in the Baltic Sea is generally low due to large amounts of fresh water provided by river discharges. Inflowing saline water from the North Sea travels along the bottom and therefore produces a permanent halocline, separating the surface water from the deep water in the basins. Saline and also often oxygen-rich inflows are essential for the deep water renewal in the largest basin of the Baltic Sea, the Eastern Gotland Basin (EGB). These inflows occur only under certain meteorological conditions and thus so-called stagnation periods (periods without inflows) can occur for several years, oxygen depletion can lead to the formation of hydrogen sulfide in the Baltic deep water.

In this work two different inflows and their effects on the deep water in the Baltic Proper were investigated. First, the major warm and saline deep inflow into the Eastern Gotland Basin, lasting from the end of November 1997 until the beginning of May 1998, was investigated. Temporal fluctuations of the deep circulation were monitored at 170 m depth by two current meter moorings deployed at the north-eastern and south-western rim of the EGB between August 1997 - September 1998. Three-dimensional structures of stratification parameters were inferred from comparisons of two high-resolution hydrographic surveys carried out before and during the end of the 1997/1998 inflow. Results indicated a lifting of near-bottom isopycnals by more than 50 m during the inflow up to a depth of 170 m. Since the basin is enclosed at 170 m depth this implies a complete deep water renewal. Detected warm-water intrusions enhanced the temperature variability on isopycnal surfaces at intermediate depth, creating strong inverse temperature gradients below the halocline. Corresponding Turner angles suggest a significant contribution of diffusive convection to diapycnal mixing in this region. In contrast, for the deepest near-bottom layers which were only marginally affected by intrusions, basin-scale budgets of heat and salinity suggest comparable diffusivities ($\kappa_s = 1.3 - 2.1 \times 10^{-5}$ m^2/s for salt and $\kappa_\theta = 1.6 - 2.8 \times 10^{-5}$ m^2/s for potential temperature), implying that double-diffusion does not play a major role in mixing there. For intermediate layers between 90-170 m the basin is not closed, thus the budget method could not be adopted. Instead an idealised model for the decay of temperature variance associated with the intrusions was applied. Results indicate that the intrusions decay within a few weeks, corresponding to vertical diffusivities of a few times 10^{-5} m^2/s.

Secondly, a cold, oxygen-rich inflow in intermediate waters was captured in May 2006 in the Stolpe Channel and later in September of the same year in the EGB.

Temporal means of the zonal velocity of two ADCPs, deployed between September and December 2006 at the outlet of the Stolpe Channel, reveal a separation of the water column, where the eastward flow

at the northern side dominates depths between 65 - 71 m and depths of 52 - 71 m at the southern side of the channel. The layer above on the other hand shows a westward flow. The deep, mainly eastward flow exhibits fluctuations of about 2 - 4 days.

Hourly and daily volume transports estimated from ADCP measurements for this period agree well with modelled volume transports from the high spatial resolution (1 nautical mile) MOM4 model. All significant peaks in estimated transports were also captured by modelled volume transports. The mean volume transport through the Stolpe Channel for estimated volumes is 0.75 $\pm$ 2.32 km^3/d and slightly higher for modelled volumes 0.81 $\pm$ 3.15 km^3/d, both are well correlated with R= 0.79.

In the Stolpe Channel the following mechanisms can be derived from correlations. The sea level is directly steered by the regional wind and surface waters in the same direction as the wind. The deep current is mainly steered by changes in the sea level and is counteracting to the surface flow, i.e. during winds from the west the deep currents travel towards west and during winds from the east currents travel eastwards. Although, in times of weak westerly winds deep eastward currents still prevail, but then originate from a geostrophic flow. Hence, observed pulse-like currents in the Stolpe Channel are partly driven by the regional wind, i.e. up to 50 % and partly driven by sloping density gradients of dense bottom waters and therefore resulting geostrophic currents. Comparisons of the wind's frequency spectrum with the frequency spectra of the along-slope current of the two ADCPs reveal that the 2 - 4 day long current fluctuations originate from changes in the regional wind. Each of these fluctuations transports a volume of around 1.78 $\pm$ 1.15 km^3/d eastwards. These 2 - 4 day long fluctuations transport nearly the same volume in a single event as the 3-monthly mean.

Contents

Abstract **iii**

Contents **v**

List of Figures **xi**

List of Tables **xv**

1 Introduction **1**

1.1 Investigations of spatiotemporal scales in the Baltic Proper 1

1.2 Topography of deep Baltic basins 3

1.3 Basic hydrography 5

1.4 Pulsating inflows 6

1.5 Recent inflow history 9

1.6 Deep boundary currents 10

1.7 Methodical specifics 11

2 Data and Methods **13**

2.1 Data 13

2.1.1 MESODYN project 1997/98 13

2.1.2 RAGO project 2006/07 13

2.2 Analysis of observational data 15

2.2.1 Hydrographical data 15

2.2.2 Current records 16

2.2.3 Wind measurements and sea level gauges 17

2.3 Numerical model MOM4 18

2.3.1 Model specifications 18

2.3.2 Model data 21

3 A case study of thermal variability following deep water intrusions in the Eastern Gotland Basin **23**

3.1 The deep inflow event 23

3.1.1 Mooring data 23

3.1.2 MESODYN data 25

3.2 Thermal variability on isopycnals 28

3.2.1 Lateral patterns 28

3.2.2 Vertical transects 30

3.2.3 Vertical and temporal variability 33

3.2.4 Salinity and heat budgets 35

3.2.5 Decay of temperature variance 39

4 The Deep Circulation in the EGB (Inter-basin communication of deep Baltic basins and their effects for the deep circulation) **43**

4.1 Hydrography of the Eastern Gotland Basin 43

4.2 Propagation of temperature and current signals 45

4.3 The Stolpe Channel 52

4.3.1 Hydrography of the Stolpe Channel 52

4.3.2 Geostrophic velocities 52

4.3.3 Transports through the Stolpe Channel 56

4.3.4 Propagation of deep water from the Stolpe Channel to the Eastern Gotland Basin 63

4.3.5 Current fluctuations within the Stolpe Channel - steering mechanism . . . 80

5 Discussion and Conclusions **91**

5.1 Deep water intrusions 91

5.2 Deep boundary currents 92

5.3 Future Outlook 96

Bibliography **97**

Acknowledgement **104**

Appendix **106**

List of Abbreviations

ÅS	Åland Sea
ADCP	Acoustic Doppler Current Profiler
AB	Arkona Basin
BB	Bornholm Basin
BCh	Bornholm Channel
BoB	Bay of Bothnia
BMP	Baltic Monitoring Programme
BS	Bothnian Sea
BY	Baltic Year
CTD	Conductivity, temperature, depth measurements
d	Day
dbar	decibar
Δ	Difference
DaS	Darss Sill
DrS	Drogden Sill
DWD	German Weather Service (Deutscher Wetter Dienst)
FD	Farø Deep
EGB	Eastern Gotland Basin
FFT	fast Fourier transform
GB	Gdansk Basin
GE	Gedser
GoF	Golf of Finland
GoR	Golf of Riga
GrB	Great Belt
HB	Hoburg
HO	Hornbaek
IOW	Leibnitz Institute for Baltic Sea Research Warnemuende
K	Kattegat
KPP	k-profile parameterisations
LD	Landsort Deep
LO	Landsort gauge

M-7/M-8	Mesodyn hydrographic snapshots 7 and 8
MESODYN	MESO-scale DYNamics
MBI	Major Baltic Inflow
MOM	Modular Ocean Model
NE	Mooring north-east
nm	nautical mile
ØS	Øresund
O_2	Oxygen (ml/l)
R	Correlation Coefficient
RAGO	tiefe RAndströme im östlichen Gotlandbecken der Ostsee (deep boundary currents in the Eastern Gotland Basin)
RCM-7/8/9	Self recording current meter
S	Salinity (g/kg)
SA	Sassnitz
$SalEGB_{170}$	modelled Salt content of EGB below 170 m depth
$Saltrp55_{12}$	modelled positive/negative (northward/southward) salt transport through Gdansk Basin at 55°N filtered for salinities $\geq$ 12 g/kg salt
$Saltrp55_{12P}$	modelled positive salt transport through Gdansk Basin at 55°N
$Saltrp55_{12N}$	modelled negative salt transport through Gdansk Basin at 55°N
$Saltrp56_{12}$	modelled positive/negative (northward/southward) salt transport through Hoburg Channel at 56°N filtered for salinities $\geq$ 12 g/kg salt
$Saltrp56_{12P}$	modelled positive salt transport through Hoburg Channel at 56°N
$Saltrp56_{12N}$	modelled negative salt transport through Hoburg at 56°N
$SaltrpSF_{9.5}$	modelled positive/negative (eastward/westward) salt transport through Stolpe Channel at 17.5°E filtered for densities $\geq$ 9.5 kg/m^3
$SaltrpSF_{9.5P}$	modelled positive salt transport through Stolpe Channel at 17.5°E
$SaltrpSF_{9.5N}$	modelled negative salt transport through Stolpe Channel at 17.5°E
$SaltrpSF_{12}$	modelled positive/negative (eastward/westward) salt transport through Stolpe Channel at 17.5°
$SaltrpSF_{12P}$	modelled positive salt transport through Stolpe Channel at 17.5°E
$SaltrpSF_{12N}$	modelled negative salt transport through Stolpe Channel at 17.5°E
SE	Mooring south-east
SK	Skagerrak

SF	Stolpe Channel (Stolpe Furrow)
SFN	ADCP Stolpe Channel North
SFS	ADCP Stolpe Channel South
SL	Sea level (cm)
SLP	Sea level pressure (hPa)
Std Dev	standard deviation
SW	Mooring south-west
θ	Potential Temperature ($^{\circ}C$)
TU	Turner Angle (°)
Voltrp55_{12}	modelled positive/negative (northward/southward) volume transport through Gdansk Basin at 55°N filtered for salinities $\geq$ 12 g/kg salt
Voltrp55_{12P}	modelled positive volume transport through Gdansk Basin at 55°N
Voltrp55_{12N}	modelled negative volume transport through Gdansk Basin at 55°N
Voltrp56_{12}	modelled positive/negative (northward/southward) volume transport through Hoburg Channel at 56°N filtered for salinities $\geq$ 12 g/kg salt
Voltrp56_{12P}	modelled positive salt transport through Hoburg Channel at 56°N
Voltrp56_{12N}	modelled negative salt transport through Hoburg Channel at 56°N
$\text{VoltrpSF}_{9.5}$	modelled positive/negative (eastward/westward) volume transport through Stolpe Channel at 17.5°E filtered for densities $\geq$ 9.5 kg/m^3
$\text{VoltrpSF}_{9.5P}$	modelled positive volume transport through Stolpe Channel at 17.5°E
$\text{VoltrpSF}_{9.5N}$	modelled negative volume transport through Stolpe Channel at 17.5°E
VoltrpSF_{12}	modelled positive/negative (eastward/westward) volume transport through Stolpe Channel at 17.5°E filtered for salinities $\geq$12 g/kg salt
VoltrpSF_{12P}	modelled positive volume transport through Stolpe Channel at 17.5°E
VoltrpSF_{12N}	modelled negative volume transport through Stolpe Channel at 17.5°E
VoltrpSF_{ADCP}	positive/negative (eastw./west.) measured volume transport through Stolpe Channel (17.5°E) betw. 52 m (SFS) and 65 m (SFN) to bottom
VP	Ventspils
WGB	West Gotland Basin
z	standardised time series

List of Figures

1.1 Baltic Sea - bathymetric map of research area 4

1.2 Topographic map of Eastern Gotland Basin 9

2.1 Map of model configurations Baltic Sea 20

3.1 Daily temperatures and currents at NE and SW in 170 m 24

3.2 θ/S plots of CTD stations from MESODYN surveys M-7 and M-8 26

3.3 θ/S plots of M-7 and M-8 on selected σ_θ surfaces 27

3.4 $\Delta\theta$ between density surfaces $\sigma_\theta = 9.5$ kg/m^3 and $\sigma_\theta = 9.4$ kg/m^3 29

3.5 θ section at 57.24 °N of M-7 and M-8 31

3.6 Section of Turner angle at 57.24 °N for diffusive convective regime 32

3.7 Depth profiles of θ at BMP271 33

3.8 Depth profiles of Turner angles at BMP271 34

3.9 Sketch of salinity and heat budget calculations 36

3.10 Depth profiles of θ and salinity below 190 m at BMP271 37

3.11 θ vs. depth, time series of $\langle\theta'^2\rangle$, vertical intrusion scale vs. diffusivity of heat . . 40

4.1 NE to SW transects of Θ, S, σ_t,O_2 through EGB 44

4.2 NW to SE transects of Θ, S, σ_t,O_2 through EGB 45

4.3 Θ, S, O_2 profiles at BMP271 in 2006 46

4.4 Temperatures of mooring SE 47

4.5 Temperatures of mooring NE 49

4.6 Temperatures of mooring SW 50

4.7 Θ, S, O_2 profiles at BMP222 in 2006 53

4.8 Θ, S and O_2 sections across Stolpe Channel 54

4.9 Geostrophic velocities on 22 and 29 September 2006 of Stolpe Channel 56

4.10 Zonal and meridional velocities at SFN and SFS 57

4.11 Modelled velocities east at SFS 58
4.12 Daily zonal velocities at SFN and SFS 58
4.13 Mean vertical profiles of SFN and SFS 59
4.14 Sketch of volume transport calculations through Stolpe Channel 61
4.15 Modelled and measured volume transports through Stolpe Channel 62
4.16 Calculated volume of EGB 64
4.17 Total salt content of deep EGB 65
4.18 Baltic Sea map of modelled bottom salinity and currents 67
4.19 Modelled volume transport through Stolpe Channel, Gdansk Basin and Hoburg Channel 68
4.20 Modelled salt transport through Stolpe Channel, Gdansk Basin and Hoburg Channel 69
4.21 Cumulative volume through Stolpe Channel salt $\geq$ 12 g/kg 72
4.22 Cumulative salt through Stolpe Channel salt $\geq$ 12 g/kg 73
4.23 Cumulative volume through Gdansk Basin salt $\geq$ 12 g/kg 74
4.24 Cumulative salt through Gdansk Basin salt $\geq$ 12 g/kg 75
4.25 Cumulative salt through Hoburg Channel salt $\geq$ 12 g/kg 76
4.26 Modelled hourly, daily and 5-daily deep volume transport through Stolpe Channel 79
4.27 Daily wind <U>38 (Arkona-Hoburg) and daily along-slope velocities of SFN and SFS 82
4.28 Baltic Sea Map with sea level gauges and meteorological stations 84
4.29 Standardised time series of sea level difference SL Δ(Ventspils-Sassnitz) and regional wind <U>38 and regression of regional wind <U>38 (Arkona-Hoburg) with sea level difference SL Δ(Ventspils-Sassnitz) 86
4.30 Depth correlation of <U>38 with zonal SFN/ zonal SFS; depth correlation of sea level difference SL Δ (Ventspils-Sassnitz) with zonal SFN/zonal SFS and standardised time series of <U>38 and zonal velocity (66-71m) 87
4.31 Regression SL Δ(Ventspils-Sassnitz) with zonal velocity/ volume transport ($66-71$ m) Stolpe Channel 88
4.32 Regression sea level difference SL Δ (Ventspils-Sassnitz) with volume transport (below 9.5 kg/m^3) Stolpe Channel and wind <U>38 with volume transports Stolpe Channel 89

5.1 Currents at mooring SE 107
5.2 Currents at mooring NE 108

5.3 Currents at mooring SW 109
5.4 Power Spectral Density 110
5.5 Cumulative volume through Stolpe Channel salt < 12 g/kg 111
5.6 Cumulative salt through Stolpe Channel salt < 12 g/kg 112
5.7 Cumulative volume through Stolpe Channel whole water column 113
5.8 Cumulative salt through Stolpe Channel whole water column 114
5.9 Power spectrum of wind <U>38 115
5.10 Power spectral density Stolpe Channel 115
5.11 Spectral density SE 116
5.12 Power spectral density NE 117
5.13 Power spectral density SW 118

List of Tables

3.1 Mooring NE and SW: averaged velocities and max. speeds 25

3.2 Vertical averaged density ratio and Turner angle of BMP271 35

3.3 Volume averaged salinities and temperatures 39

3.4 Lower bounds for vertical fluxes and diffusivities 39

4.1 Stolpe Channel: comparison of measured and modelled volume transports 63

4.2 Cross-correlations of volume and salt transports of Stolpe Channel, Gdansk Basin, Hoburg Channel and salt content EGB 70

4.3 Cumulative volume and salt of Stolpe Channel, Gdansk Basin and Hoburg Channel for salt $\geq$ 12 g/kg 77

4.4 Mass balance of cumulative volume and salt of Stolpe Channel 78

4.5 Mean volume transports Stolpe Channel 80

Chapter 1

Introduction

1.1 Investigations of spatiotemporal scales in the Baltic Proper

The Baltic Sea is mainly surrounded by land, thus water exchanges with the North Atlantic Ocean take place indirectly through transition areas such as the Kattegat (K), which connects the Baltic Sea with the North Sea. To reach the Baltic Sea, its waters have to pass through the narrow sound and straights. All inflowing water is topographically trapped for a certain time in several deep basins, which are connected by channels and separated by shallow sills of different depth. The largest basin of the Baltic Sea is the Eastern Gotland Basin (EGB) with a maximum depth of 249 m. Due to its landlocked position and large amounts of river run-off the Baltic proper is strongly stratified and the density is predominantly determined by salinity. Between 60 - 90 m a strong halocline prevents mixing of the whole water column in the EGB. Exchanges of saline and oxygen-rich waters from the North Sea occur sporadically yet are essential for the ventilation of the deep EGB, since dense water masses travel along the bottom. Driving mechanism of inflows are well investigated (Matthäus and Franck, 1992), but associated spatiotemporal effects are still subject to research and crucial for the understanding of overall mechanism. The majority of inflows occur as barotropic inflows between November and January, the so-called 'inflow season' (Matthäus and Franck, 1992), when the water column in the Kattegat is well mixed and oxygenated. However, not all inflows are cold, oxygen-rich inflows, especially when the inflow occurs in summer under calm wind conditions. These inflows still manage to exchange the deep layers of the EGB, but not with the desired effect of renewing the oxygen.

The following questions arise from the effects saline inflowing water masses from the North Sea have on the deep water of the Baltic Sea and will be addressed in this thesis: What kind of

effects on the small-scale do saline inflows have on ambient water masses in the EGB? How do hydrographic parameters change due to different inflows? On what kind of spatiotemporal scale do dense water masses travel through the Stolpe Channel and what effect do they have on the deep EGB? What kind of pathways are used? How much water and salt is transported through the Baltic Proper and into the EGB? How can these dense pathways be modelled accurately? What steers these dense water masses? These questions will be attended to in the two main Chapters: Chapter 3: *A case study of thermal variability following deep water intrusions in the Eastern Gotland Basin* and in chapter 4: *The Deep Circulation in the EGB (Inter-basin communication of deep Baltic basins and their effects for the deep circulation).*

In Chapter 3 the effects of exactly such a warm inflow on water masses in the EGB will be investigated and their role in small-scale dynamics and mixing. Its waters can be clearly distinguished from those of the ambient water of the EGB by positive temperature anomalies. However, this hydrographic situation resulted in a number of unusual stratification properties in the deep EGB that have so far received only little attention. Chapter 3 focuses on changed stratification conditions due to upward mixing within near-bottom layers. Realistic mixing parameters will be discussed, especially under the aspect of double-diffusive processes. The data is based on results from the rather unique data set sampled by the MESODYN (MESO-scale DYNamics) project. These results were already published in Wieczorek et al. (2008). In contrast to those of previous intrusion studies, which were based on two-dimensional hydrographic transects as in Kuzmina et al. (2005) this approach enables a three-dimensional analysis of the mixing conditions. Two densely spaced CTD surveys with a station spacing of 2.5 nm (dots in Fig. 1.2) were carried out before and after the inflow event and some aspects of the thermohaline deep water transformation were described by Wieczorek et al. (2008) as well as in chapter 3.

However, temporal changes of the nature of such mixing conditions still remained unanswered and will be investigated in chapter 4. Therefore, two ADCPs measured currents and temperature simultaneously for three months between September and December 2006. This time span is characterised by the inflow event described in Matthäus and Franck (1992). The instruments were deployed at 75 m depth in the north and in the south of the eastern gate-way of the Stolpe Channel. Simultaneously, records of three subsurface moorings, each equipped with three current meters, were used to study associated fluctuations in the deep circulation above topographic flanks of the deep EGB between May 2006 and March 2007. The Stolpe Channel, which connects the deep Bornholm Basin like a trench with the deep Eastern Gotland Basin, is thought to be a key area for the generation of pulse-like deep water intrusions forcing corresponding fluctuations in the deep water circulation of the EGB.

In this key area the time scales of detected fluctuations will be analysed, as well as related steering mechanisms. The quantification of transports through the Stolpe Channel could be estimated from these records and obtained volume transports were compared with those obtained from model simulations. For the first time high spatial resolution current and hydrographic modelled data from MOM4 is going to be analysed in comparison with measured data. Some attention is drawn to the salt transport and pathways from the Stolpe Channel into the EGB. Thus, the question will be answered of how much of the salt then arrives in the largest basin of the Baltic Sea, the EGB, and how the resulting overall salt content varies over time. An important question is what kind of spatiotemporal resolution is required for exact model simulations, to model transports accurately. The deep water ventilation is discussed by the observations of a cold, oxygen-rich intermediate inflow in the Stolpe Channel and along two diagonal hydrographic transects crossing the EGB.

1.2 Topography of deep Baltic basins

The Baltic Sea is mainly surrounded by land, thus water exchanges with the North Atlantic Ocean take place indirectly through transition areas such as the Kattegat (K), which connects the Baltic Sea with the North Sea. To reach the western Baltic Sea, its waters have to pass three straights, the narrow Øresund (Øs) in the east and the Little Belt and Great Belt (GrB) in the west. Behind this entrance area, all inflowing water is topographically trapped for a certain time in several deep basins, which are connected by channels and separated by shallow sills of different depth, Fig. 1.1 and Fig. 2.1. Before entering the Arkona Basin (AB), the westernmost of a chain of deep basins, the inflowing water from the two Belts has to pass the only 18 m deep Darss Sill (DaS). While the water flowing through the Øresund has to pass the 7 m deep Drogden Sill (DrS) to spread into the next deep basin. The AB has a maximum depth of about 45 m and is connected with the Bornholm Basin (BB) by the Bornholm Channel (BCh). The somewhat deeper BB has a maximum depth of approximately 100 m. Its topographic contours are almost circular with a diameter of about 80 km. Further to the east, the adjacent Stolpe Channel (or Stolpe Furrow, SF) connects the BB with the Gdansk Basin (GB) as well as with the Eastern Gotland Basin (EGB). The SF exhibits a maximum depth of about 93 m and forms a channel with an extension of nearly 80 km in the west-east direction. However, dense water spreading further eastward have to pass the Stolpe Sill with a peak level of about 60 m depth at its eastern gateway to reach the GB in the southeast as well as the EGB in the northeast.

The central and largest deep basin of the Baltic Sea, the EGB, is closed from the elliptic 170 m

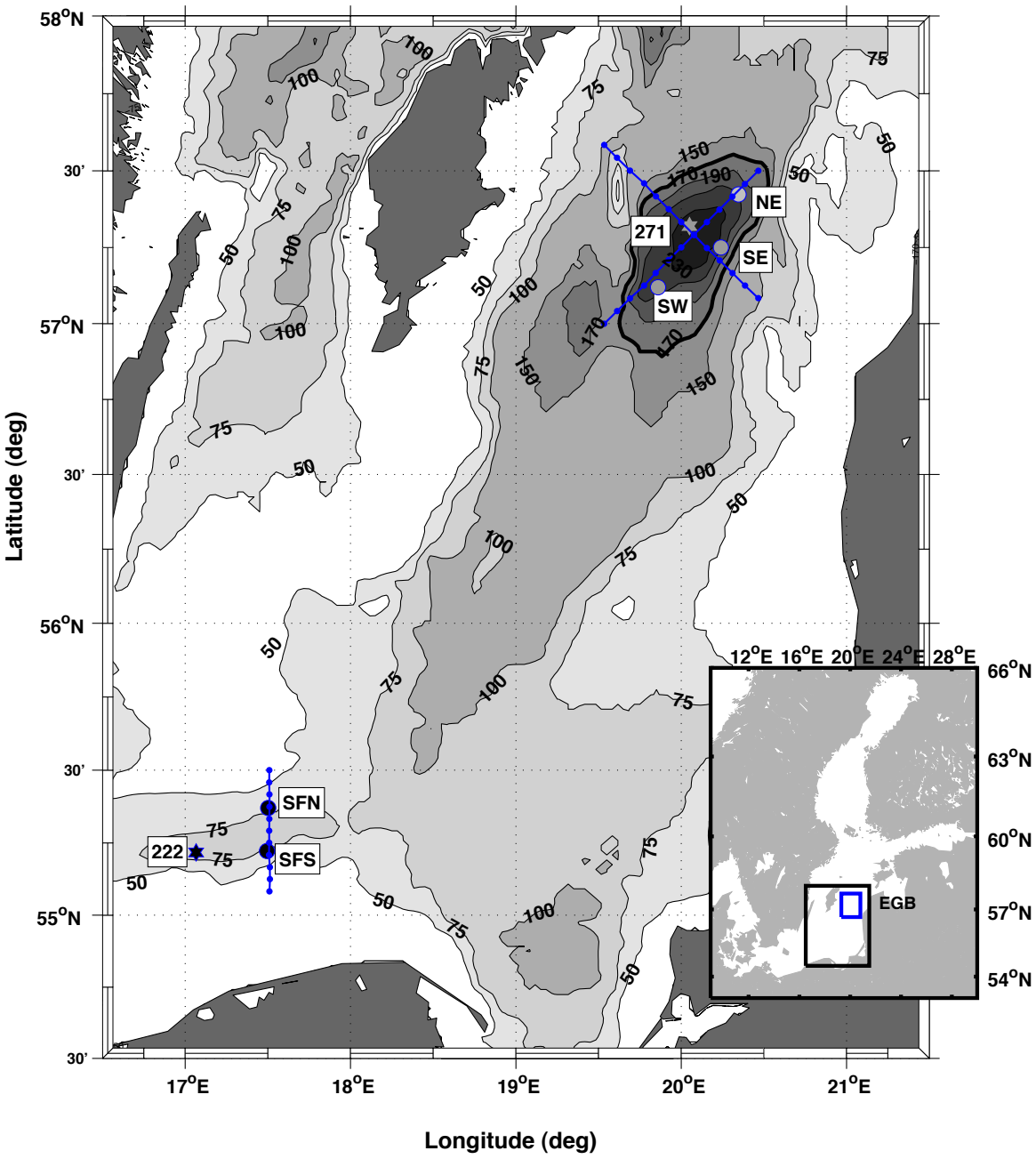

Figure 1.1: Bathymetric map of research area (inserted Eastern Gotland Basin, EGB, blue Square) in the Baltic Sea. SFN and SFS are ADCP mooring positions within the Stolpe Channel (SF); Dots mark mooring positions SE, NE and SW within the EGB. Stars mark the positions of central HELCOM-monitoring stations 222 (SF) and 271 (EGB). Dotted blue lines indicate CTD transects across the Stolpe Channel and through the EGB.

isobath downwards and has a maximum depth of 249 m, Fig. 2.1, while the so-called Landsort Deep (LD) marks the deepest location of the Baltic Sea with a depth of about 490 m in the Western Gotland Basin (WGB). Turning back to the EGB and looking further to the northeast,

the Gulf of Riga (GoR) is located in the east, while the Farø Deep (FD) continues the chain-like alignment of deep basins more in the north. Towards the northeast, the Gulf of Finland (GoF) constitutes the easternmost part of the Baltic Sea by an east-west extension. Finally, at higher latitudes, the Baltic Sea is closed by the Gulf of Bothnia which is separated from the central Baltic Sea (Baltic Proper) by the Åland Sea (ÅS). It constitutes of the Bothnian Sea (BS) in the south and the Bay of Bothnia (BoB) in the north.

1.3 Basic hydrography

Due to restricted water exchanges with the North Sea and the location in the belt of the humid west-wind zone, the whole Baltic Sea is filled by brackish water of low salinity. Consequently, all saline inflows from the North Sea produce/ maintaining a strong lateral surface gradient in salinity throughout all layers of the whole Baltic Sea. Relatively low values around 5 g/kg characterise the surface conditions in the Gulf of Bothnia while peak values of about 25 g/kg dominate corresponding conditions in the transition area of the Kattegat. Compared to the North Atlantic and the North Sea, the overall salinity in the Baltic Sea is much lower. Following Brogmus (1952) and HELCOM (1993), the overall Baltic water balance is positive with an annual freshwater surplus of about 481 km^3. The associated riverine run-off amounts to 428 km^3, the precipitation to 237 km^3, and the evaporation to 184 km^3. Consequently, the resulting annual Baltic outflow of near-surface layers is compensated by an appropriate inflow of nearly 500 km^3 saline and well oxygenated water from the Kattegat.

The basic hydrography of all deep basins reflects a permanent halocline separating the brackish near-surface water from the dense, more saline deep water in near-bottom layers. For example, the halocline in the western AB is found between 35 m and 40 m depth. In contrast, it is located significantly deeper within the EGB and occupies layers between 70 m and 90 m depth, cf. Stigebrandt (1987) and Elken (1996). However, the vertical location of this perennial halocline roughly coincides with that of the persistent pycnocline in all deep Baltic basins. The core depth of the pycnocline varies with the seasonal cycle and acts like a barrier for all vertical exchange processes between upper and deeper layers. In addition, a seasonal thermocline develops in the western and central Baltic Sea at depths between 10 m and 30 m, due to intense solar radiation during summer environmental conditions (Matthäus, 1984). During the rest of the year, however, this shallower thermocline disappears due to downward mixing, released by intense radiative cooling and enhanced wind-stirring at the sea surface. Nevertheless, this downward mixing within intermediate layers is not able to significantly affect the thermohaline properties of deep

water below the perennial pycnocline. In other words, eastward spreading Baltic deep water can be considered to be independent from the seasonal cycle of vertical mixing, observed in intermediate and upper layers. However, thermohaline properties of the deep water persistently change on its path way from one deep basin to the next deep basin (Kouts and Omstedt, 1993). Upward mixing (entrainment) in turn transforms the thermohaline conditions in intermediate and upper layers. These processes involve bottom friction and related vertical sheer in near-bottom currents triggering the breaking of internal waves on different time-scales.

Because all tidal motions are negligible in the Baltic Sea, core velocities of these deep currents are low and associated upward mixing of water properties is significantly suppressed through stable stratification conditions. Finally, the thermohaline diffusion controls all deep patterns observed by hydrographic field campaigns and the overall residence time of the Baltic deep water was estimated to be about 25-30 years, cf. Stigebrandt et al. (2002), Meier and Kauker (2003) and Meier (2007). Such a long residence time underlines the importance of sporadically occurring inflow events that reach the EGB to maintain and/ or to regenerate the deep benthic flora and fauna in the entire Baltic Proper. These events persist for days up to weeks and interrupt the deep water conditions which are commonly characterised by the so-called 'stagnation periods' lasting frequently for several years. This means, however, that the oxygen content in the Baltic deep water commonly becomes depleted and the tendency increases for the production of hydrogen sulphide, affecting the deep Baltic ecosystem for long periods of time. For example, the slow thermohaline transformation of Baltic deep water is visible by the conservation of their thermohaline characteristics after the replacement of 'old' by 'new' deep water. For instance, in the western Baltic Sea, only 50% of the 'old' Arkona Deep Water can be replaced by inflowing 'new' Arkona Deep Water for the case that the exchanged overall volume of deep water exceeds about 100 km^3. Such drastic inflow events are called 'major inflows' in the literature, Omstedt and Axell (1998). The nature of involved upward mixing will be studied in more detail in chapter 1.5 and chapter 3. Specific points of the latter also contributed to investigations already presented by Reissmann et al. (2009).

1.4 Pulsating inflows

The inflow of saline waters from the North Sea can penetrate into the south-western Baltic Sea only under certain meteorological circumstances. The transition zone of the Belt Sea has to be either well homogenised (barotropic inflows) or stratified (baroclinic inflows). Accompanying wind conditions are either very strong or very calm for of several weeks. According to Krauss

and Brügge (1991) and Schinke and Matthäus (1998), a high gradient in air pressure with strong easterly winds lasting for more than about ten days are needed to lower significantly the water level of the central Baltic and to enlarge that in the Kattegat. The established sea level (SL) gradient releases barotropic pressure gradients with down-slope currents towards the western Baltic Sea. Moreover, such a weather situation with prevailing easterlies also reduces the precipitation over Baltic catchment areas as well as the resulting river run-off. This, however, maintains a barotropic pressure gradient with positive sea level anomalies in the Kattegat and negative anomalies in the central Baltic Sea. However, it became also clear that these sea level differences fluctuate on the synoptic scale ($2-6$ d), due to corresponding variations in easterly winds. Thus, pulsating Major Baltic Inflows (MBIs) are generated on the synoptic scale (Matthäus and Franck, 1992) especially if these easterlies are suddenly replaced by westerlies lasting for about two weeks. Consequently, such MBIs are characterised by two weather phases: easterly winds dominate the pre-inflow period with lower than normal the sea level anomalies in the central Baltic; replaced by strong westerly winds initiating the mature-inflow period with the inflow of huge amounts of saline, well oxygenated Kattegat water. Such events finally weaken the barotropic pressure gradients between the Kattegat and the central Baltic Sea by pushing their waters into the first deep basin, the Arkona Basin. Only if this 'new' deep water is denser than ambient deep water of the Bornholm Basin, it enters further basins in the northeast (Hagen and Feistel, 2001). Such favourable inflow conditions usually occur in late autumn, winter, and early spring when the saline water of the Kattegat is vertically well ventilated/ oxygenated due to downward convection and wind-stirring. According to Matthäus and Franck (1992), associated volume transports through the Belts and the Sound must exceed 10 km^3/d to renew completely all deep water of the central Baltic Sea. Hydrographic long-term observations clearly show that such MBIs happen on the multi-year scale. Their irregular repetition occurs all 3-5 years. Following Wyrtki (1954), Franck et al. (1987), Matthäus and Franck (1992), Fischer and Matthäus (1996) and Feistel et al. (2003a) such MBIs convey about 200 km^3 deep water with about 2 Gt salt and about 1 Mt Oxygen towards the western Baltic Sea. In contrast, the nature of baroclinic inflows is mainly determined by lateral occurring salinity gradients in the Kattegat. They maintain corresponding baroclinic pressure gradients, especially during calm wind conditions in the late summer. Associated inflow events already described by Knudsen (1900), Thiel (1938), Hela (1944), Wüst et al. (1957), Welander (1974), Jacobsen (1980), Matthäus et al. (1983), Feistel et al. (2003c), Feistel et al. (2004) and Mohrholz et al. (2006) suggest that the frequency of such phenomena increased, probably due to changes in prevailing wind directions during the last two decades. Once triggered, these baroclinic inflows reveal a somewhat weaker volume transport

and prefer the pathway through the Great Belt via the Darss Sill. They reach the Arkona Basin after several days. Consequently, salt is frequently transported from the western Baltic Sea towards the Baltic Proper, however, on a much lower level as that released by the barotropic MBIs. Nevertheless, via triggered entrainment, they are able to change prevailing hydrographic conditions and ventilate intermediate and/ or deep layers to a certain degree. This follows from observations showing a somewhat better oxygenation of much lower efficiency. Thus, they also contribute to the development/ maintenance of the deep marine ecosystem in the Baltic Proper (Reissmann et al., 2009).

Multi-year current records which have been carried out above the eastern topographic slope of the EGB (Hagen and Feistel, 2004). Their results suggest an overall velocity of 3 cm/s for the cyclonic deep circulation. Its core velocity reflects a topographically steered rim current, which is highly geostrophic and accelerates up to a factor of 3 during such baroclinic inflow events. During and after such events, large lateral pressure and salinity gradients between the central EGB (low pressure) and its rim (high pressure) cause saline water to follow the bottom topography and circulate cyclonically within it (Lehmann and Hinrichsen, 2000).

Internal pressure gradients react to changes in wind forcing and river discharges releasing vertical and lateral meanders into the rim currents (Elken, 1996). Such current meanders are thought to be formed by rhythmic inflows and temporal changes in the actual wind-stress curl as well as by the conservation of the potential vorticity of the deep current field behind irregularities in the bathymetry like that of the well known Klints Bank in the EGB. In hydrographic fields within and below the main pycnocline, these meanders form eddy-like features with diameters between 5 km and 15 km and a vertical thickness of several decametres. Repeated hydrographic surveys suggest that their life time exceeds one week (Elken, 1996). These meso-scale features rotate cyclonically or anti-cyclonically with core velocities reaching up to 20 cm/s, although their lateral displacement velocity is only $2-3$ cm/s (Hagen, 2004). However, when hitting such obstacles as that of the Klints Bank, these features can also be destroyed on much shorter time-scales. Recently, there is some speculation that the decay of such phenomena also contributes to the erosion of the main pycnocline on the basin-scale. Following Kuzmina et al. (2005), a great portion of their kinetic energy should be lost through turbulent mixing when these features collide with the boundaries of the basin. From the methodical point of view, Reißmann (2005) developed objective methods for an adequate recognition of such meso-scale patterns in the mass-field. He called these Baltic eddies 'Beddies', in analogy to the so-called 'Meddies' observed at the latitude of the Strait of Gibraltar in the Atlantic Ocean.

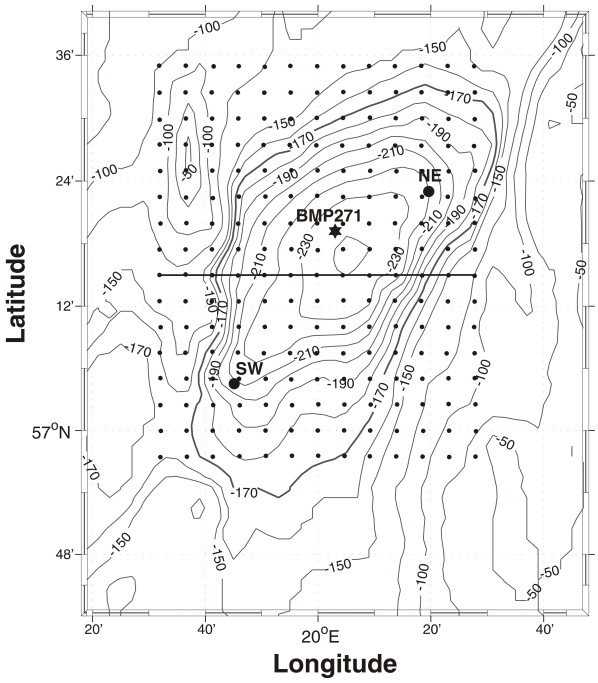

Figure 1.2: Bathymetric map of the Eastern Gotland Basin (blue square in Fig. 1.1) with positions of the mooring sites northeast (NE) and south-west (SW) deployed 1997-98, the central Baltic monitoring station BMP271 of the HELCOM programme (star) and hydrographic stations of the MESODYN M-7 (13×16 stations) and M-8 (13×15 stations) campaigns (small dots). The horizontal line marks the position of the vertical sections in Fig. 3.5. Note the 170 m isoline bounds the enclosed parts of the deep basin.

1.5 Recent inflow history

Matthäus and Franck (1992) show that the so-called MBIs mainly appear between October and April. Their frequency of occurrence is very irregular, from once per year to once per ten years separated by infamous stagnation periods. The longest observed stagnation period of nearly 16 years occurred between 1976 and 1993, during which only some weak inflow events were observed between 1976 and 1983. Therefore, they were classified to be insufficient for renewing the near-bottom water of all basins. This long stagnation period was terminated by a substantial inflow event observed in 1993. It was the objective of a number of investigations. Changes in meso-scale thermohaline variability and driving mechanisms of intrusions as a result of this inflow were analysed on the base of field observations as well as by scenarios simulated by hydrographic circulation models, Zhurbas and Paka (1997), Zhurbas and Paka (1999), Zhurbas et al. (2003) and Kuzmina et al. (2005). Zhurbas and Paka (1997) and Zhurbas and Paka (1999) used closely spaced CTD profiles ranging from the Stolpe Channel to the Gotland Basin three months after the 1993 inflow to also investigate intrusive layering and its most important

features. Thus, these authors presented results which describe several consequences of such deep water intrusions, especially with respect to the generation of eddy-like features on the meso-scale. Kuzmina et al. (2005) also studied associated driving mechanisms and concluded that embedded diffusive convection also works in the Baltic halocline. It triggers diapycnal mixing, regardless of the overwhelming stratification. Due to the observed homogenisation of the deep water, this inflow event was classified as 'moderate' by Matthäus (1993). Somewhat later, on the base of an increased data density, Matthäus et al. (2008) reclassified this event as MBI. It became evident that most of involved deep waters entered the southern Baltic Sea via the Drogden Sill and not, as assumed before, through the Darss Sill. These authors also described the next notable strong inflow event. It entered the EGB (Fig. 1.2) in November 1997 and lasted until May 1998. This event was extraordinary in many respects and several specifics are highlighted in chapter 3. This inflow can be considered to be the starting point of an unusual series of so-called warm inflow events, cf. Feistel et al. (2003a), Feistel et al. (2003b), Feistel et al. (2006). The intermediate intrusions of these warm water masses originate from near-surface layers of the Kattegat formed under summer environmental conditions. In contrast to the barotropic inflows occurring usually during the winter season, this baroclinic warm water inflow started in the late summer. However, this hydrographic situation of positive temperature anomalies resulted in a number of unusual stratification properties in the deep EGB that have so far received only little attention. Therefore, the main objective of the chapter 3 focuses on changed stratification conditions due to upward mixing within the enclosed deep basin. Realistic mixing parameters will be discussed, especially under the aspect of double-diffusive processes.

1.6 Deep boundary currents

Several studies about the mass/ volume fluxes through the Stolpe Channel can be found in the literature. These used numerical experiments by applying appropriate circulation models as well as hydrographic data sets with a different station spacing. However, the most pioneering study about such transports was a mix of both approaches and published by Krauss and Brügge (1991). Their results suggest that the renewal of the deep water in the EGB is a combination of wind-driven currents within the near-surface layers and density-driven, geostrophically adjusted currents within near-bottom layers. Easterly winds produce sea level gradients with low values in the east and high values in the west of the Baltic Proper. This, however, forces down-slope gradient currents towards the east. Whereas the density-driven flow is slow but persisting, strong easterly and northerly winds fluctuate on the synoptic scale and accelerate transports

of dense deep water through the Stolpe Channel. For example, Kouts and Omstedt (1993) investigated these conditions for two decades ($1970 - 1990$) and estimated a mean deep volume transport of 0.28 km^3/d carrying an overall mean salinity of 13 g/kg towards the east. Starting in 2002 and ending in 2003, Piechura and Beszczyńska-Möller (2004) carried out altogether six detailed hydrographic surveys to monitor the 2003 inflow in the Arkona Basin, the Bornholm Basin, the Stolpe Channel, and in the Gdansk Basin. They concluded that mainly mixed water from intermediate layers of the Bornholm Basin makes its way into the Stolpe Channel. The largest volume of saline deep water which entered the deeper layers of the Stolpe Channel $2 - 3$ months after the inflow was first recorded at the Darss Sill in January 2003. Borenäs et al. (2007) investigated whether the hydraulic theory is suitable to quantify maximal transports. For comparisons with real data long-term observations from monitoring stations in the Bornholm Basin and in the Gdansk Basin were used. These observations revealed that the hydraulic theory is only of limited use to estimated transports through the Stolpe Channel. Meier and Kauker (2003b) found that a small positive west wind anomaly causes a systematically reduced eastward salt flow above the bottom of the Stolpe Channel during stagnation periods. Furthermore, there is some observational evidence that strong precipitation over the central Baltic catchment area with enhanced river discharges also reduces the net deep eastward flow through the Stolpe Channel. In contrast to Kouts and Omstedt (1993), these authors calculated the value of 2.69 km^3/d. It is higher by factor of about ten for the time period between 1902 and 1998. Independently from involved methodical uncertainties, this discrepancy clearly points to the importance of longer lasting changes in prevailing winds and associated precipitation conditions for the generation of spatiotemporal modifications in internal pressure gradients and the Baltic deep water circulation.

To obtain somewhat more insight into related processes, for the first time, current measurements were conducted by two ADCPs at the eastern gateway of the Stolpe Channel at 75 m water depth, just above the northern and the southern flank of the channel. Their records cover three months (September - December 2006). Chapter 4 describes detected fluctuations as well as related steering mechanisms.

1.7 Methodical specifics

This study applies the unit g/kg for the salinity. The numerical value of absolute salinity in grams of salt per kilogram of seawater is somewhat higher than that of the Practical Salinity Scale (PSS-78), roughly by 0.5%, as discussed in more detail by Jackett et al. (2006). Such a

deviation is considered to be irrelevant for most estimates made in this paper. Here, values of the absolute salinity rather than those of the usual Practical Salinity Scale are used to estimate saline fluxes/ transports. It seems to be that the best estimate for the absolute salinity of the so-called 'Standard Seawater' is given by the Reference-Composition Salinity proposed by Millero et al. (2008). In the following, all salinity values represent the unit g/kg of this new salinity scale by using algorithms developed by Reissmann et al. (2009).

Chapter 2

Data and Methods

2.1 Data

2.1.1 MESODYN project 1997/98

In the following the hydrographic and current data of this study are summarised ordered by project:

- CTD grid, EGB, Aug./Sep 1997, Apr. 1998:
  CTD measurements in the EGB: MESODYN-7 (M-7) August/September 1996, series of 13×16 CTD stations, MESODYN-8 (M-8) April 1998, series of 13×15 CTD stations with a distance of 2.5 nautical miles (4.6 km) between the stations.

- CTD station BMP271, EGB, 1997 - 98
  Central monitoring station EGB BMP271: 57°19.2′ N, 20°3.0′ E

- Mooring Northeast (NE), EGB, Aug. 1997 - Sep 1998:
  deployed at 57°22.16′ N, 20°20.0′ E in 220 m with continuous current meter and temperature measurements for almost 9 years (1999-2006). Only the overlapping time period with mooring SW was looked at in this case.

- Mooring Southwest (SW), EGB, Aug. 1997 - Sep 1998:
  was deployed at 57°04.53′ N, 19°45.12′ E in 210 m depth on 29 August 1997 and recovered on 15 September 1998.

2.1.2 RAGO project 2006/07

- Moored ADCP, Stolpe Channel, Sep. 2006 - Feb. 2007:
  Deployment (22 September 2006) of two Teledyne RDI WorkHorse Monitor ADCPs (Acous-

tic Doppler Current Profiler) at the outlet of the Stolpe Channel in 75 m depth: ADCP SFN (600 kHz) located at 55°22.23′ N,17°30.12′ E recorded data until 18 December 2006. ADCP SFS (300 kHz) located at 55°13.34'N, 17°29.67′ E recorded data until 7 February 2007.

- 2 CTD sections, Stolpe Channel, 22. + 29. Sep. 2006:
  across the Stolpe Channel (11 CTD stations) on 22 September 2006 at $55.1 - 55.5°$ N, 17.5° E; section repeated on 29 September 2006.

- 2 CTD sections, EGB, 26./27. + 27./28. Sep. 2006:
  two diagonal sections (13 CTD stations each) in the EGB from northeast to southwest ($26 - 27$ September 2006) and from northwest to southeast ($27 - 28$ September 2006).

- Moorings SE, NE and SW, EGB:
  Deployment (7 May 2006) of 3 moorings within the EGB (SE, NE & SW) in 224 m depth recorded current and temperature data, mooring SE at 57°15.40′ N, 20°14.40′ E and mooring SW at 57°7.20′ N, 19°51.60′ E until 30 March 2007. Mooring NE failed to be recovered, therefore it was replaced on the 27 September 2006 at (57°22.16′ N, 20°20.0′ E) and recorded current and temperature data until 30 March 2007.

- CTD station BMP222, Stolpe Channel, 2006:
  Monitoring station Stolpe Channel: BMP222 at 55°13.0199′ N, 17°3.9417′ E.

- CTD station BMP271, EGB,:
  Monitoring station BMP271 at 57°19.2′ N, 20°3.0′ E.

- Meteorological stations, Arkona buoy and Hoburg, Gotland, 2006 - 2007:
  Wind data from Arkona buoy at 54°55.92′ N, 13°51.58′ E and wind data from Hoburg (HB), Gotland at 56°55′ N, 18°09′ E.

- Sea Level gauges, several stations, 2006 - 2007:
  Hornbaek (HO, 56°06′ N, 12°28′ E), Gedser (GE, 54°34′ N, 11°56′ E) Sassnitz (SA, 54°30.5′ N, 13°38′ E), Ventspils (VP, 57°24′ N, 21°33′ E) and Landsort (LO, 58°45′ N, 17°52′ E).

- Model data from MOM4/IOW model, 2006 - 2009:
  MOM4/IOW Model data with a high horizontal resolution of 1 nautical mile (nm) covering the whole Baltic Sea. In this study: 5-day mean values of temperature, salinity and currents for three transects in the Stolpe Channel ($54.9 - 55.7$°N,17.5°E), the Gdansk Basin

(55°N, 18.4 – 19.9°E) and Hoburg Channel (56°N, 18.2 – 19.6°E) between 2002 – 2009. Hourly values for Stolpe Channel (54.9 – 55.7°N, 16 – 18°E) between June 2006 and June 2007.

2.2 Analysis of observational data

2.2.1 Hydrographical data

Measurements of temperature, T, salinity, S, oxygen, O_2 and depth, D, are regularly carried out by the Leibniz Institute for Baltic Sea Research Warnemuende (IOW) under the umbrella of the Baltic Monitoring Programme (COMBINE) of the Helsinki Commission (HELCOM). Resulting CTD data sets between 1968 – 1998 and 2006 were used to describe the overall hydrographic regime at the central station BMP271 (57°19.2′ N, 20°3.0′ E, see Fig. 1.2). This position roughly coincides with that of the former Baltic Year station BY-15A. Here, the water depth is about 242 m (Hagen and Feistel, 2001), and hydrographic profiles were available five times per year. Sampling followed the standard guidelines for the COMBINE programme at standard depths, and is considered to be representative for the description of trends in the hydrographic regime of the whole Baltic Proper (Fig. 1.1). This data set illustrates that the seasonal variability of deep water stratification parameters is relatively small. Consequently, most of the overall deep T-S profiles are found to be in a narrow range, compared to the surface water variability. This made it possible to calculate an average profile characterizing thermohaline properties between the upper halocline (60 m) and 225 m depth (see Fig. 3.2.

Beyond these single-point measurements, spatial CTD data from the MESODYN project were evaluated. Two campaigns were carried out in August/ September 1997 (M-7), and in April 1998 (M-8), i.e. just before and at the end of the warm inflow event, respectively. Data for M-7 were obtained on a 13×16 station grid sampled from 29 August to 04 September 1997. CTD profiles for M-8 were obtained on a coinciding grid from 19 – 24 April 1998, except for the southernmost zonal section that was not sampled due to severe weather conditions. Available for our analysis were therefore 208 CTD stations from the M-7 survey and 195 CTD stations from the M-8 survey (see Fig. 1.2). Both field campaigns started in the northwest and followed zonal transects towards the southern deep basin. In each case, the station spacing was 2.5 nm (4.6 km). This was sufficient to resolve eddy-like patterns of the mass field larger than about 9 km, smaller eddies cannot be resolved. The internal Rossby radius is therefore marginally resolved but for even smaller features aliasing effects have to be expected. Note that the two

grid stations closest to the central station BMP271 were formally identified with BMP271 to increase the temporal resolution in the centre of the basin (see Fig. 1.2).

Data acquisition and validation procedures are described in more detail by Hagen and Feistel (2001). Potential temperature, θ, and potential density, σ_θ, were computed according to the thermodynamical relations suggested by Feistel and Hagen (1995) with the required reference level placed at the sea surface. Finally, all vertical profiles were low-pass filtered with a 3 m running window in order to suppress high-frequency noise, and to avoid aliasing errors.

For the 2006/07 study within the RAGO (tiefe RAndströme im östlichen Gotlandbecken der Ostsee, English: deep boundary currents in the Eastern Gotland Basin of the Baltic Sea) project, two diagonal CTD transects with 13 CTD profiles each were carried out. The first transect went from northeast to southwest on $26-27$ September 2006 and the other transect went from northwest to southeast on $27-28$ September 2006. The stations were chosen from the MESODYN project's grid and both transects had a spacing of around 3.5 nm, shown as a dotted cross in Fig. 1.1. These transects provided a snapshot of the hydrographic situation in the EGB and were then compared to data from the central monitoring station (BMP271), the model data and also to the temperature data from the three moorings to complete the general picture.

The two CTD transect across the Stolpe Channel carried out on the 22 and 29 September 2006 were also first established and part of the MESODYN project described in detail by Reissmann (1999), Reißmann (2002) and Reissmann (2006). From the transects with its 11 CTD stations (marked as dotted line in Fig. 1.1) and a station spacing of 2.5 nm not only the hydrographic situation was revealed, but also geostrophic velocities could be calculated. The hydrographic situation of the Stolpe Channel in 2006 was further described by CTD data from its central monitoring station BMP222 (Fig. 1.1).

2.2.2 Current records

Two sub-surface moorings, deployed in August 1997 along the 220 m isobath of the EGB in the northeast (NE) and the southwest (SW), measured currents and temperature at 170 m depth with a recording Aanderaa current meter (RCM7). The NE mooring was positioned at 57°23.0′ N, 20°19.5′ E and the SW mooring at 57°04.0′ N, 19°45.0′ E, see Fig. 1.2. Both moorings simultaneously recorded current velocity and direction as well as the temperature

with a sampling interval of one hour from the 30 August 1997 until 21 July 1998. On this basis, the zonal (u) and meridional current components (v) were computed. Thereafter, daily averages and corresponding variances were computed for both current components and the temperature series. These time series recorded the 1997/98 warm inflow, described in the case study of chapter 3.

The two ADCP's (positions shown in Fig. 1.1) overlapping deployment time of 87 days was primarily used for the analysis described in chapter 4. From these measurements the zonal (u), meridional (v) and vertical (w) velocities were obtained to estimate volume transports across the channel which were later compared with transports obtained from the MOM4 model simulations. Furthermore temperature records provided information on possible inflows.

Long-term current measurements from May 2006 until March 2007 of three subsurface moorings, each equipped with three current meters (Aanderaa RCM7/9) monitored the deep circulation within the EGB. The three moorings were deployed above topographic flanks in about 224 m depth. Mooring SE and mooring SW were deployed on 7 May 2006 shown in Fig. 1.1. Mooring NE could not be recovered either in May 2006 or in September 2006, thus no data coverage for that period. A new mooring was deployed on the 27 September 2006 to record current and temperature data until it was recovered on 30 March 2007. The along-shelf and across-shelf components of mooring SE and SW were obtained by calculating the rotation angle between the vertical average of $175 - 220$ m for SE (14.98°) and between $175 - 220$ m for SW with 86.7°. The current components of mooring NE were not rotated, for a rotation angle of -0.6° can be neglected. The current meters of SE and SW measured for 326 days, whereas the length of the NE time series was 182 days.

2.2.3 Wind measurements and sea level gauges

Hourly Wind measurements from the Arkona buoy in the Arkona Basin (AB) at 54°55.92′ N, 13°51.58′ E (altitude above sea level: 10 m) and 6 hour wind data from Hoburg (HB), Gotland (56°55′ N, 18°09′ E, altitude above sea level: 39 m)[1] were obtained (Fig. 4.28). To match the currents the Arkona and Hoburg winds were rotated by 180°. The mean wind between Arkona and Hoburg was calculated and rotated by 38° (<U>38) along the major axis of the Stolpe Channel to estimate its effect on the filling level of the Baltic Proper.

Daily data of sea level (SL) gauges Hornbaek (HO, 56°06′ N, 12°28′ E), Gedser (GE, 54°34′ N,

[1] http://meteo.infospace.ru

11°56′ E) Sassnitz (SA, 54°30.5′ N, 13°38′ E), Ventspils[2](VP, 57°24′ N, 21°33′ E) and Landsort (LO, 58°45′ N, 17°52′ E) were used to calculate daily sea level differences and to determine the general in- and outflow between the Kattegat and the western Baltic Sea (HO-GE) and the sea levels differences in the Baltic Proper (VP-SA), see Fig. 4.28. The data of sea level gauging stations VP, SA and LO was detrended with the mean of each data set (1 January 2006 – 24 August 2007) removed to make the data comparable. For the analysis the 87 day deployment period of the ADCPs between 23 September and 18 December 2006 was then extracted.

2.3 Numerical model MOM4

The interpretation of the measurements, analysed in this study, is completed by comparisons with data from a high-resolution circulation model of the Baltic Sea. The three-dimensional (3D) fields of hydrographic state variables extracted from a realistic model simulation complement the observational findings since they provide a description of the full system which is continuous in space and time.

The model, applied at IOW, is a specific Baltic Sea adaptation of the Modular Ocean Model (MOM), which is a state-of-the-art model used world-wide in the scientific community for local, regional and global ocean circulation. The MOM provides a toolbox of well established advection and mixing schemes, which are continuously improved by contributions of the user group. The MOM code is fully documented in a detailed manual, see Griffies et al. (2004). Examples of MOM based model simulations for the Baltic Sea are summarised in Schmidt et al. (2008).

2.3.1 Model specifications

The model data utilised for this study rely on a simulation of the Baltic Sea which is based on the code version MOM-4. Essential features of the MOM adaptation for the Baltic Sea at IOW are:

- High resolution digital Baltic bathymetry of Seifert et al. (2001),
- A tracer conserving treatment of fresh water fluxes, see Griffies et al. (2001),
- An atmospheric boundary layer module, computing air-sea fluxes of heat and momentum from standard weather model data (wind, air pressures, air temperature, humidity and cloudiness),

[2]http://www.meteo.lv/pdf_base/juras_2003.html

- Coupling of salinity and water temperature at the open boundary in Skagerrak to monthly climatological means derived from Janssen et al. (1999); the sea level is prescribed according to sea level gauge observations at Kungsvik provided by Swedish Meteorological-Hydrological Institute (SMHI, Norrköping),
- Average monthly discharge of fresh water by rivers derived from Bergström and Carlsson (1993) and adapted to the total yearly runoff which is continuously updated by HELCOM (2009).

The model configuration is illustrated in Fig. 2.1. The model comprises the whole Baltic Sea between $9^\circ\,20' - 15^\circ\,20'$ E and $53^\circ\,50' - 56^\circ\,20'$ N with a regular grid referring to a spherical earth of 6371 km radius. The horizontal grid spacing of 1 minute with respect to geographical longitude and 2 minutes in longitude corresponds to a horizontal resolution of 1 nautical mile or 2 km, respectively. The horizontal grid is of the so-called B-type, thus grid points of current components (u, v) are half a grid step staggered against the grid points where scalar quantities, like temperature and salinity, are set-up. Vertically, the water body is divided into 77 layers of prescribed thickness (geopotential or z-coordinates). For the upper 27 m, layers have a thickness of only 1.5 m in order to resolve the shallow sills in the southwestern Baltic Sea. Below 27 m, the layer thickness is smoothly stretched to 5 m to a maximum depth of 268 m. At the sea bottom partial grid cells of at least 0.5 m thickness are applied to approximate topographic slopes. The undisturbed surface layer has a thickness of 2.6 m which allows realistic sea level variations of up to approximately ± 1.5 m. Such a high vertical and horizontal resolution is needed to resolve the processes relevant in the Baltic Sea, since the long-term thermohaline circulation is dependent on various short-term events like minor and major inflows, drifting eddies and coastal jets. The spatial scale of these processes is small in comparison with the horizontal scale of the sub-basins and channels, the baroclinic Rossby radius is in the order of only $1 - 7$ km (Fennel et al., 1991), small in comparison with the horizontal scale of the sub-basins and channels.

Vertical mixing processes are modelled by the k-profile parameterisation (KPP), a non-local scheme described in detail by Large et al. (1994), whereas horizontal mixing and viscosity are calculated from current shear using a Smagorinski scheme, see Smagorinsky (1963), Smagorinsky (1993) and Griffies and Hallberg (2000).

The meteorological forcing of the Baltic Sea MOM4 simulations is provided by the Deutscher Wetterdienst (DWD, German Weather service) running the regional model COSMO-EU[3] (formerly known as DWD/LME) which covers the whole European region with a grid spacing of

[3]http://www.cosmo-model.org/content/tasks/operational/dwd/default_eu.htm

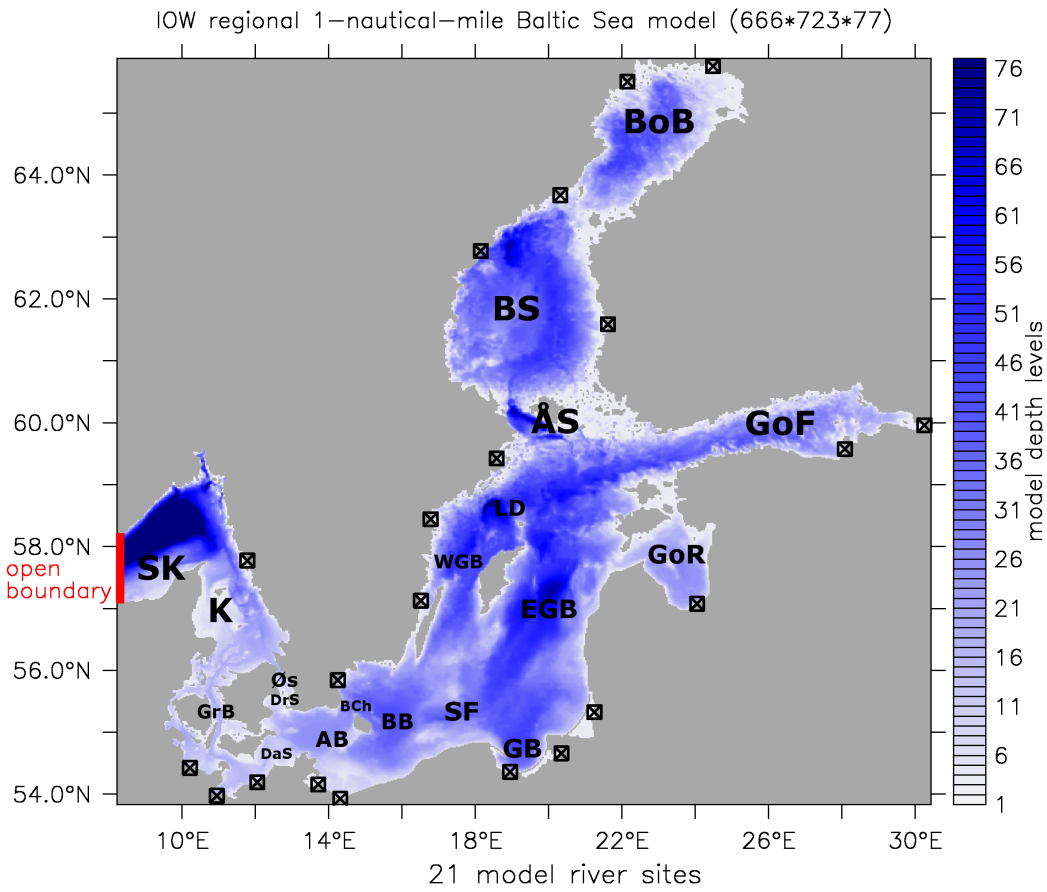

Figure 2.1: Map of model configurations Baltic Sea with river discharges (black crosses) and model boundary (red line). Skagerrak (SK), Kattegat (K), Great Belt (GrB), Darss Sill (DaS), Drogden Sill (DrS), Øresund (Ø), Arkona Basin (AB), Bornholm Channel (BCh), Borhnholm Basin (BB), Stolpe Channel (SF, Stolpe Furrow), Gdansk Basin (GB), Western Gotland Basin (WGB), Eastern Gotland Basin (EGB), Landsort Deep (LD), Golf of Riga (GoR), Golf of Finland (GoF), Åland Sea (ÅS), Bothnian Sea (BS), Bay of Bothnia (BoB).

7 km. Output from the operational forecasts at $3-15$ hours is archived twice daily at IOW with a time resolution of 3 hours. Air-sea fluxes of mass, momentum and energy are calculated from air pressure, air temperature, dew point temperature, wind, precipitation, cloudiness, and downward short wave and long wave at the sea surface according to standard parameterisations taken from Beljaars (1995).

2.3.2 Model data

Because of its high resolution the Baltic model requires high computation and storage capacity. The simulations are carried out on the high-performance parallel computers of Norddeutscher Verbund für Hoch- und Höchstleistungsrechnen (HLRN) at Berlin and Hannover. The model runs (in time slices of 30 days) are finished with storage of a restart snapshot. Full 3D model fields are saved as 5-day averages since every parameter requires 140 MB per time step. High frequency model time series are produced by model restarts using the MOM4 option of restricted output for confined areas and periods.

In this study the 5-day mean values of a model run for the period September 2002 to September 2009 were used to calculate volume and salt transports through three transects across Stolpe Channel ($54.9 - 55.7°$N, $17.5°$E), the Gdansk Basin ($55°$N, $18.4 - 19.9°$E) and across the Hoburg Channel ($56°$N, $18.2 - 19.6°$E). Positions are marked in Fig. 4.18. For the EGB time dependent salt volumes for the deep layers ($170 - 241$ m) were obtained from the 5-day means.

Hourly temperature, salinity and current values were only computed for small selected areas and short time periods for example the Stolpe Channel ($54.9 - 55.7°$N, $16 - 18°$E) between June 2006 and June 2007. Modelled deep hourly transports through the Stolpe Channel were then compared to deep transports obtained from measured ADCP data (SFN and SFS).

Chapter 3

A case study of thermal variability following deep water intrusions in the Eastern Gotland Basin

3.1 The deep inflow event

3.1.1 Mooring data

The deep warm-water inflow was recorded at 170 m depth by the two temperature sensors at the moorings NE and SW shown in Fig. 1.2. Resulting records illustrate that exceptional warm deep water reached mooring NE on 28 November 1997 after a quiescent period with little temporal variability (Fig. 3.1 a). This cyclonically travelling thermal signal was not observed before 27 December 1997 at moorings SW, i.e. it was visible with a delay of approximately 30 days. Superimposed fluctuations suggest that the warm-water inflow was not continuous. Both temperature records exhibit a total of eight large pulse-like events, each with an average duration of about 20 days. Associated temperature changes were somewhat stronger at position NE than at SW, reaching peak temperatures of 6.7 °C on 13 March 1998, and 6.6 °C on 23 March 1998, respectively (Fig. 3.1 a). Following Lehmann and Hinrichsen (2000) and assuming that such temperature anomalies travel in some geostrophically adjusted way along isobaths between both positions, the observed time-lag suggest an overall propagation speed of approximately 3 cm/s. This estimate is consistent with the averaged along-slope inflow velocities as discussed in the following.

Obtained daily current records from mooring NE illustrate that pre-inflow velocities were di-

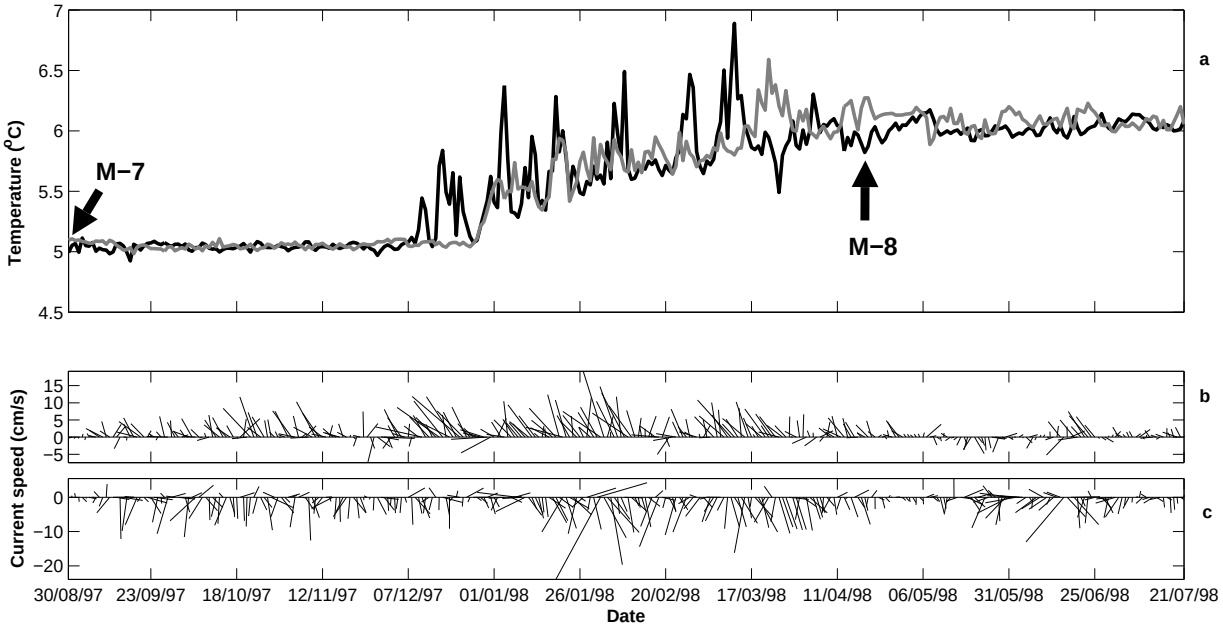

Figure 3.1: Daily temperature and current series of Aanderaa current meters deployed at 170 m depth at positions shown in Fig. 1.2 and statistics compiled in Table 3.1: a) Daily temperature records (°) of the NE (black) and SW moorings(grey). Two arrows mark the CTD surveys M-7 (before) and M-8 (during the end of the inflow). Note that the warm deep water inflow reached the NE mooring around the 27 November 1997, but the SW position 30 days later. b) Stick plot of daily current speed (cm/s) of mooring NE and c) stick plot of mooring SW; note the different vertical scales of b) and c). Date displayed as dd/mm/yy.

rected towards the northwest, while those of mooring SW mainly pointed to the south, cf. Fig. 3.1 b and c and Table 3.1. At 170 m depth, both moorings also recorded an increase in velocity during the inflow period, just after the arrival of thermal fronts. Consequently, the accelerated deep water circulation was observed with some delay after the temperature fronts have passed the mooring positions. During the main inflow period, the current directions exhibit increased variability but their overall tendency remained that of the pre-inflow situation. This, however suggests that the currents of this layer roughly followed the local topography. The northwestward currents at NE (Fig. 3.1 b) were somewhat stronger than the currents at SW, where southward currents dominated the whole measuring period (see Fig. 3.1c). Note the different vertical scales of Fig. 3.1 b and Fig. 3.1 c. With the beginning of May, the current speed at NE became weak and its direction changed to the south for several weeks. This is seen to be a clear indicator that the inflow period terminated completely above the eastern topographic flank of the EGB in May. Such a change in the overall current direction accompanied by a relaxed deep water circulation was much lesser pronounced at the position SW. Here, the over-

Mooring	*Time Periods*	$\langle u \rangle (cm/s)$	$\langle v \rangle (cm/s)$	$\lvert V \rvert_{max} (cm/s)$
	Pre-inflow			
NE	30.8.1997 - 27.11.1997	−1.9	2.4	22.6
SW	30.8.1997 - 26.12.1997	0.5	−3.0	19.1
	Inflow			
NE	28.11.1997 - 6.5.1998	−3.1	4.2	29.0
SW	27.12.1997 - 25.5.1998	0.9	−4.0	32.2
	Post-inflow			
NE	7.5. - 21.7.1998	−0.5	0.3	12.1
SW	26.5. - 21.7.1998	−1.7	−2.5	20.6

Table 3.1: Averaged zonal $\langle u \rangle$ and meridional $\langle v \rangle$ velocities at moorings NE and SW before, during and after the inflow, as well as maximum hourly speeds ($|V|_{max}$).

all southward direction continued for the entire recording time although the current strength slightly weakened.

In summary, these two synchronous current series suggest a cyclonic deep water circulation at 170 m depth on a basin scale which is forced and/or maintained by rotationally deflected near-bottom gravity currents entering the EGB above its eastern topographic flank. Associated fluctuations in their forcing generate pulses of warm water intrusions propagating roughly along the deep isobaths from the mooring NE towards that of the position SW. Thus, these observations confirm the scenario of the deep water circulation in the EGB proposed by Lehmann and Hinrichsen (2000) and Zhurbas et al. (2003) developed on the base of numerical experiments from different hydrodynamic models.

3.1.2 MESODYN data

The two hydrographic snapshots, part of the MESODYN project, compare stagnant deep water conditions (M-7) with those measured after the inflow event (M-8) at the times indicated in Fig. 3.1 a. The overall θ-S diagrams of the two hydrographic surveys (Fig. 3.2) describe the changes in water composition and variability induced by the inflow for layers deeper than 60 m. Obtained relations are compared with the 'climatological state' monitored at the BMP271 station (1968-1998). Before the inflow, potential temperatures are below the 30 year averages, and their θ-S cluster is located inside the standard deviations of the climatological data (Fig. 3.2 a). Associated thermohaline changes can be described by comparing these pre-inflow characteristics with those of the M-8 campaign. The isopycnal variability of θ-S properties, embedded in the potential density layer of the halocline (σ_θ = 6.8-8.5 kg/m^3) was very small during the pre-inflow period. This is confirmed by the spatially computed standard deviations on selected

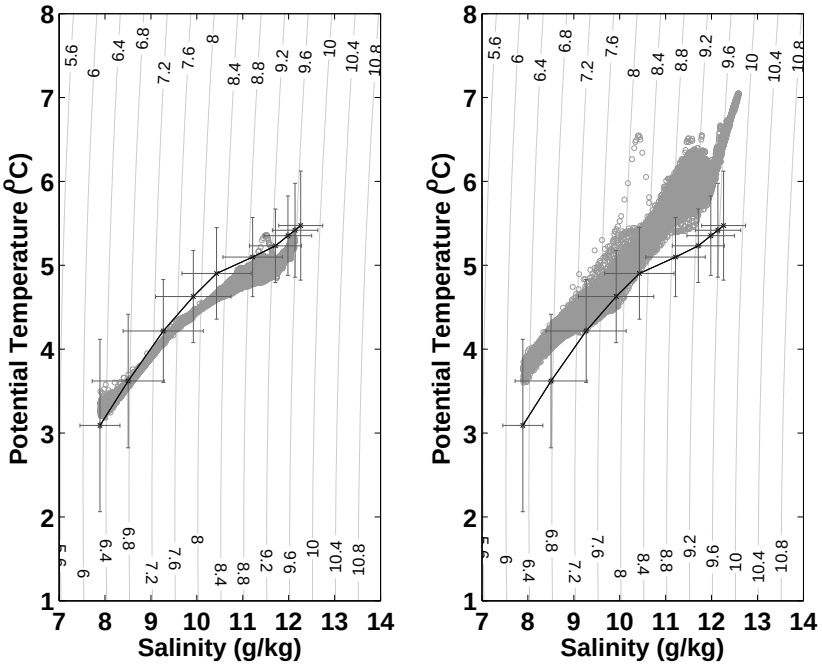

Figure 3.2: θ/S plots of hydrographic stations M-7 (grey circles, left panel) and M-8 (grey circles, right panel) below 60 m. M-7 was conducted between 29 August - 04 September 1997, M-8 between 19 - 24 April 1998. The black line is the 30 yr mean with standard deviations of potential temperature (θ) and salinity (S) of BMP271. BMP271 and station grid of M-7/M-8 are shown in Fig. 1.2.

density surfaces. Further towards the sea bed, ($8.5 \leq \sigma_\theta \leq 9.2$) kg/m^3, the standard deviation increases by about 0.4 °C on the basin-scale.

Dramatic changes in the thermohaline properties were observed especially in the near-bottom region as a result of the inflow (see Fig. 3.2 b). Taking into account that isobaths are closed up to a depth of approximately 170 m (bold isobath in Fig. 1.2), it becomes evident that the former cold deep water of the basin was completely replaced by warm water with densities exceeding $\sigma_\theta = 9.8$ kg/m^3. It also becomes clear that the former densest water ($\sigma_\theta = 9.57$ kg/m^3) was uplifted to reach depths shallower than 170 m. All temperatures that were measured during the M-8 campaign exceed those of the M-7 survey as well as those of the 30 year climatology measured at BMP271 in layers beneath the halocline (60 m). This can also be seen, for example, by comparing vertical temperature sections crossing the central basin at 57 °14.40′ N, Fig. 3.5 a, b. Potential temperatures of the deepest layers rose from 5.35 °C (M-7) to 7.06 °C (M-8) and salinities increased from 12.1 to 12.6 g/kg, respectively. The spatial variability in θ peaked within the range $8.8 \leq \sigma_\theta \leq 9.2$ kg/m^3 and decreased towards layers embedded within the pycnocline for $\sigma_\theta < 7.2$ kg/m^3.

In order to obtain some estimates on changes in the isopycnal distribution of hydrographic

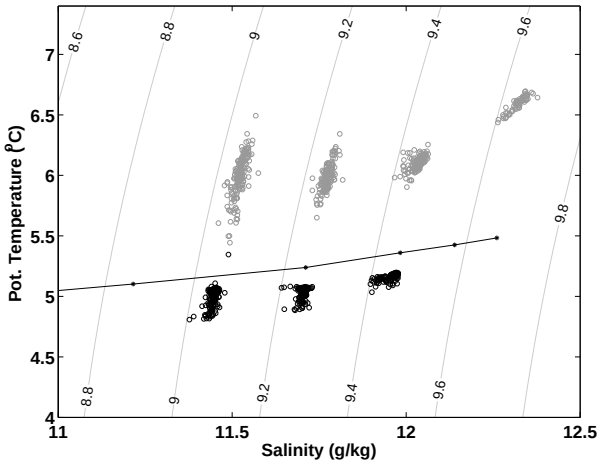

Figure 3.3: θ/S plots of survey M-7 (black) and M-8 (grey) on potential density surfaces (σ_θ) of $9.0 \leq \sigma_\theta < 9.1$ kg/m^3, $9.2 \leq \sigma_\theta < 9.3$ kg/m^3, $9.4 \leq \sigma_\theta < 9.5$ kg/m^3, $9.6 \leq \sigma_\theta < 9.7$ kg/m^3, before and during the terminating deep water inflow; thin lateral line corresponds to 30 year averages of station BMP271.

properties of the EGB, four 'sub-volumes' below the pycnocline were defined:

i) $9.0 \leq \sigma_\theta < 9.1$ kg/m^3,

ii $9.2 \leq \sigma_\theta < 9.3$ kg/m^3,

iii) $9.4 \leq \sigma_\theta < 9.5$ kg/m^3,

iv) $9.6 \leq \sigma_\theta < 9.7$ kg/m^3.

The θ-S properties of these volumes are plotted in Fig. 3.3. Before the inflow (M-7, black circles) all densities were lower than $\sigma_\theta = 9.6$ kg/m^3, and waters of category (iv) were thus missing. More or less, the resulting θ-S clusters scattered around a single point, implying that deep water properties were relatively homogeneous along isopycnal surfaces. After the inflow (M-8, grey circles), θ increased by about 1.5 °C, while at the same time the isopycnal variability strongly increased. Peak values occurred within the upper layer (i), where θ values varied between 5.2 °C and 6.5 °C ($\Delta\theta = 1.3$ °C). Somewhat deeper, layer (ii) only exhibited a thermal variability between 5.6 °C and 6.5 °C ($\Delta\theta = 0.9$ °C). This variability further decreased to be in the range of $\Delta\theta = 0.4$ °C within the layers (iii) and (iv). Consequently, the isopycnal θ-S variability drastically decreased towards the sea bed.

These changes in thermohaline properties on four selected isopycnal surfaces confirm that all near-bottom waters were replaced completely during that inflow event. In providing a substantial ambient density stratification, the EGB can be considered as an effective filter for inflowing waters masses with variable properties. Only the densest and most compact water masses are "allowed" to reach the bottom as dense bottom gravity currents. Less dense waters, originating either from less dense source waters or from "detrainment" of interfacial fluid from the bottom

gravity current (Baines (2002) and Özgökmen et al. (2006)), continue as isopycnal intrusions at their equilibrium density level. Therefore, a greater variability of thermohaline water properties is frequently observed in such intermediate layers. In the following, associated three-dimensional changes will be investigated in somewhat more detail.

3.2 Thermal variability on isopycnals

3.2.1 Lateral patterns

The increase of variance on isopycnals due to vertically only weakly correlated warm-water intrusions may be an effective mechanism for creating vertical temperature gradients. In order to estimate this effect for a typical deep isopycnal surface, the distribution of θ has been studied as an example for the two surfaces $\sigma_\theta = 9.4$ kg/m^3 and $\sigma_\theta = 9.5$ kg/m^3 obtained from the M-8 campaign during the late-stage of the inflow event. The difference in potential temperature between these two neighbouring isopycnals is illustrated in Fig. 3.4 a revealing that strong, locally confined temperature gradients have indeed been established.

In order to determine the stratification regime prevailing under these conditions we use the density ratio

$$R_\rho = \frac{\alpha \partial_z \theta}{\beta \partial_z S} \,, \tag{3.1}$$

and the so-called 'Turner angle' proposed by Turner (1965) on the base of laboratory experiments to characterise spatially different stratification regimes,

$$Tu = \tan^{-1}\left(\frac{\alpha \partial_z \theta + \beta \partial_z S}{\alpha \partial_z \theta - \beta \partial_z S}\right). \tag{3.2}$$

This methodical approach follows that of Turner (1979), Ruddick (1983), Zhurbas and Paka (1999), Kuzmina et al. (2005). The thermal expansion coefficient is given by α and β is the saline contraction coefficient. The physical information contained in R_ρ and Tu is equivalent, but the Turner angle allows a particularly simple sub-division of the different stratification regimes:

(i) the diffusive convective regime $-90\,^\circ < \mathrm{Tu} < -45\,^\circ$ (or $0 < R_\rho < 1$),
(ii) the stable regime $-45\,^\circ < \mathrm{Tu} < +45\,^\circ$ ($-\infty < R_\rho < 0$),
(iii) the salt-fingering regime $+45\,^\circ < \mathrm{Tu} < +90\,^\circ$ ($1 < R_\rho < \infty$), and
(iv) the gravitational unstable regime $\mathrm{Tu} \geq +90\,^\circ$.

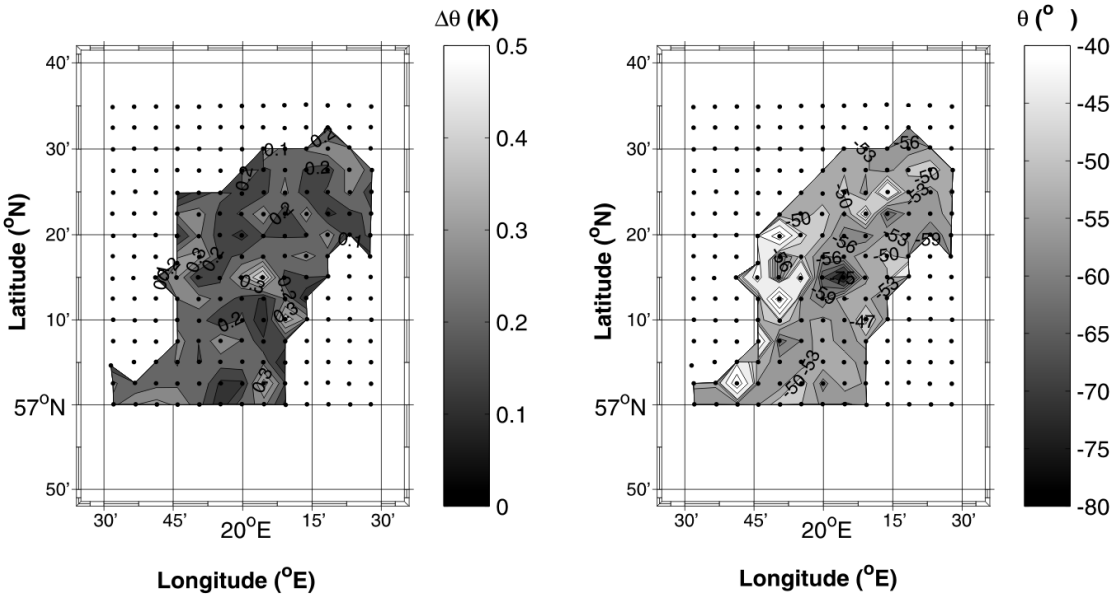

Figure 3.4: a) Difference in potential temperatures ($\Delta\theta$) between the potential density surfaces σ_θ = 9.5 kg/m^3 and σ_θ = 9.4 kg/m^3 measured during the end of the deep water inflow (M-8). b) The Turner angle on potential density surface σ_θ = 9.5 kg/m^3 at the end of the deep water inflow (M-8). Values between $-90\,^\circ$ and $-48.81\,^\circ$ (or $1/15 < R_\rho < 1$) suggest diffusive convective mixing (lighter grey to black).

Apart from rare exceptions, the stability of the water column in the Baltic Sea is dominated by a stable salinity gradient (Zhurbas and Paka (1999), Kuzmina et al. (2005)). Consequently, regime (ii) is the most frequently observed in the deep EGB. However, warm-water intrusions, as observed here, may create inverse temperature gradients sufficient for a shift to regime (i), where diffusive convection may occur. In the observations and investigations of Baltic Sea intrusions during the 1993 inflow, Kuzmina et al. (2005) suggested the slightly more stringent condition $1/15 < R_\rho < 1$ (i.e. $-90\,^\circ < \mathrm{Tu} < -48.81\,^\circ$) for effective diffusive convection to occur. Kuzmina et al. (2005) derived this limitation consequence from Huppert (1971), who based it on laboratory experiments by Turner (1965), where $\kappa_S/\kappa_T \approx 0.15 R_\rho$ ($R_\rho < 0.5$ with κ_S, κ_T as apparent diffusivities for heat and salt). In the following these bounds will be used to determine whether diffusive convection convection can be considered to be a general consequence of such warm deep-water intrusions.

For the late-stage inflow conditions (M-8), values of Tu were computed and projected on the deep σ_θ = 9.5 kg/m^3 surface (see Fig. 3.4 b). Comparing Fig. 3.4 a with Fig. 3.4 b, it becomes evident that strong "diapycnal" temperature gradients, computed over a relatively large vertical distance of around 20 - 30 m (compare Fig. 3.5), favour the local appearance of regime (i) values of Tu. Altogether, these estimates suggest that the patterned temperature distribution on deep

isopycnals is favourable for diffusive convection on selected isopycnals, in particular near the centre of the basin (Fig. 3.4 b). In the absence of appropriate fine-scale and direct turbulence measurements, it is, however, not possible to quantify the relative importance of this process with respect to mixing driven by shear instabilities resulting, e.g. from internal waves motions.

3.2.2 Vertical transects

The zonal transect at 57 °14.4′ N across the basin's centre during stagnant deep water conditions (M-7) illustrates that the temperature distribution on isopycnals was quite homogeneous ($\theta \leq$ 5.3 °C) in layers deeper than 60 m depth (see Fig. 3.5 a). No intrusions were visible during that time. Associated values of Tu point to a slight tendency for diffusive convective mixing (see Fig. 3.6 a). The comparison of these conditions with those of the campaign M-8 (Fig. 3.6 b) clearly shows that the inflow of deep warm water was associated with an upward displacement of deep isopycnals. For instance, the density surface σ_θ = 9.4 kg/m^3 was located at a depth of about 170 m before the inflow (Fig. 3.6 a). During its end (M-8, Fig. 3.5 b), however, it was found between 140 and 150 m, thus uplifted by 37 m above the basin's centre to occupy about 71% of the MESODYN station grid. The zonal transect of M-8 reveals that the core of the uplift was located over the steep eastern topographic flank of the basin.

Consequently the thermohaline deep water regime dramatically changed after the inflow event (Fig. 3.5 b). The mean vertical temperature gradient had strongly increased due to the replacement of colder bottom water by warm inflow water. This points to a dominance of the diffusive convection regime (i), producing numerous local warm temperature anomalies below the halocline down to a depth of approximately 180 m. A particularly strong intrusion was centred around 20.07 °E at a depth of approximately 170 m. In contrast, no such intrusions could be detected within comparable layers during pre-inflow conditions, Fig. 3.5 a. Here, estimated Tu values ($\sim$ -45°) point to a much weaker diffusive convective mixing with a slight tendency for the stable regime (ii).

From the methodical point of view, it must be noted that the detected horizontal extent of such intrusive patches is almost always below the CTD grid resolution. The well known sampling theorem postulates that the smallest resolved spatial scale is just twice of the station spacing used. This means for the MESODYN hydrographic data sets with the station resolution of 2.5 nm that any patterns smaller than about 9 km can be biased methodically.

Presented observations from the M-8 field campaign however show that the detected mesoscale patterns are vertically coherent over larger spatial scales. These phenomena probably result

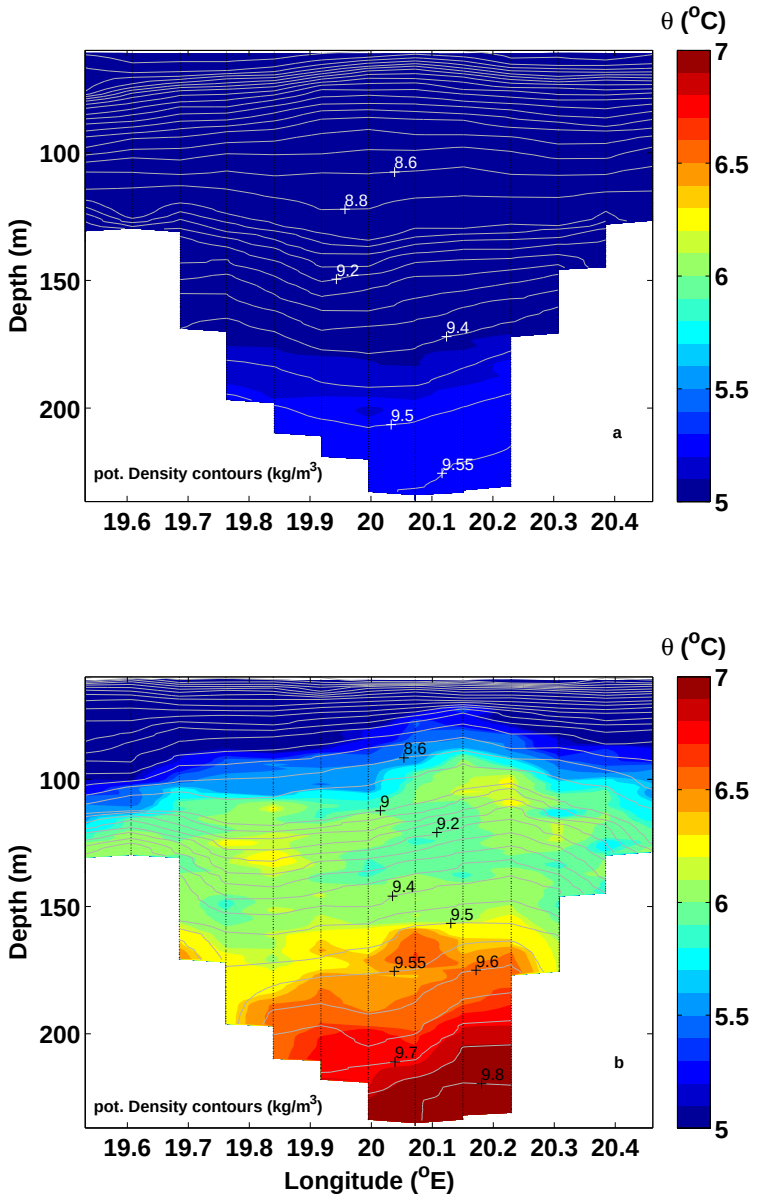

Figure 3.5: Horizontal section of potential temperature vs. depth and density contours of M-7 (a) and M-8 (b) at latitude 57.24 °N. Its position is marked as a horizontal line in Fig. 1.2.

from different processes acting on different spatiotemporal scales. It may be speculated that intrusions, which have been initially coherent over larger spatial scales were, at this late-stage of the inflow, already distorted by the strain field of mesoscale motions. The σ_θ contours in Fig. 3.5 b suggest that there were a few eddies in and below the halocline during M-8. For example, accepting the geostrophic adjustment within such eddy-like features, the shape of the isopycnals suggests differently rotating features in and below the main halocline, Fig. 3.6 b. Here, the feature with an anticyclonic rotation occurred at 19.65 °E in the halocline (70 - 90 m), while the cyclonic one was placed directly beneath it in 90 - 120 m. Their generation mechanisms are

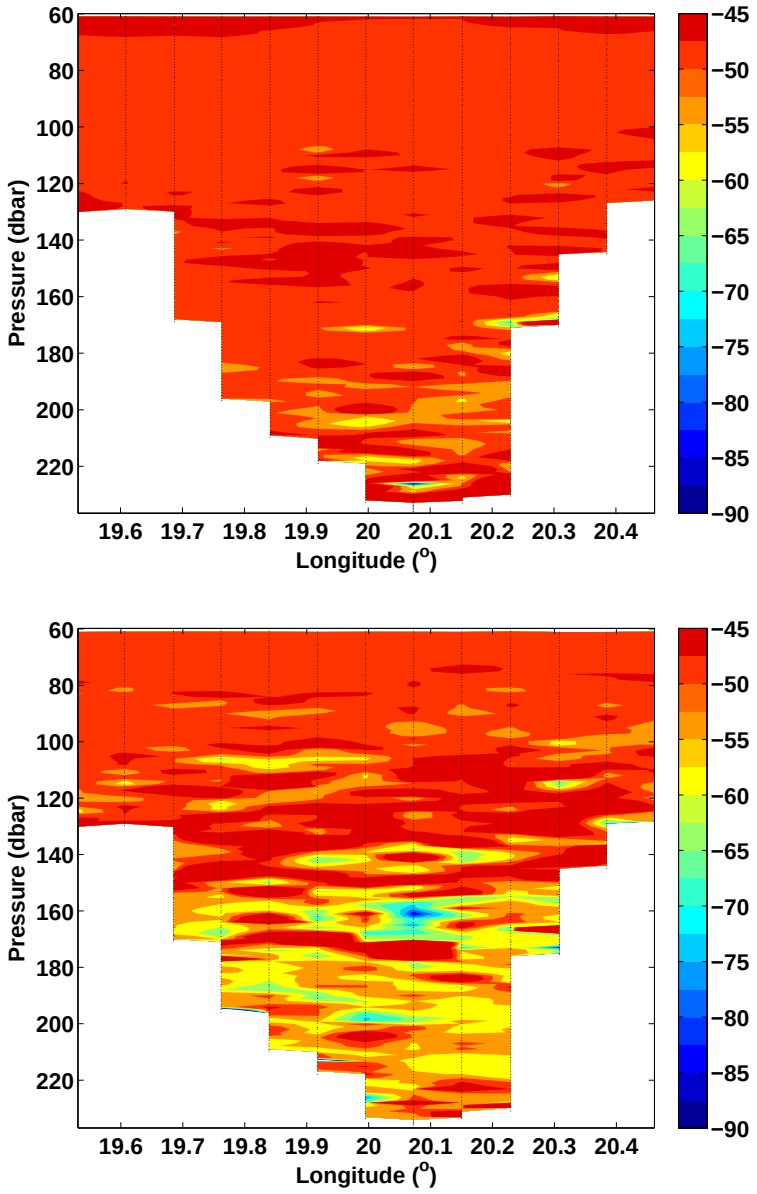

Figure 3.6: Transect as in Fig. 3.5, but for Turner angles in the diffusive convective regime, with Tu $< -48.81°$ (dark red) or $R_\rho > 1/15$ as the lower bound of diffusive convection.

considered to be outside the scope of this study, but were examined in more detail by Reißmann (2002), Reißmann (2005) and Zhurbas and Paka (1997).

Looking for associated mixing conditions, all estimated values of Tu suggest that there was a predominance of the diffusive convective regime in the whole deep domain (Fig. 3.6 b). All Tu values between $-90\,° <$ Tu$< -60\,°$ (or $0.25 < R_\rho < 1$), indicated a large tendency for diffusive convection, were generally found on top of the warm intrusions. This is nicely illustrated for the particularly strong intrusion in Fig. 3.6 b (between 19.99 °E and 20.15 °E). This intrusion was topped at around 161 m depth by a single cell with a peak value of Tu $= -83.9\,°$ (or $R_\rho = 0.81$).

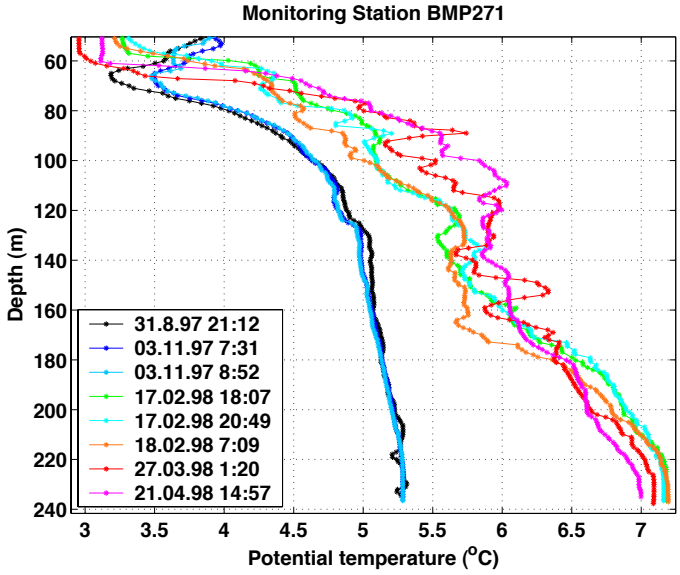

Figure 3.7: Potential temperature vs. depth of the monitoring station BMP271 below 50 m to the bottom, see Fig. 1.2. Sampling time given as dd.mm.yy HH:MM UTC.

The lateral extension of this patch stretched over the distance of 10 km $(19.99 - 20.15)\,°$E.

3.2.3 Vertical and temporal variability

The temporal evolution of temperature and salinity between the two basin-scale field campaigns M7 and M8 discussed above is illustrated by a series of CTD profiles taken at or near the central monitoring station BMP271 (see Fig. 3.7). The initial three profiles measured in August and November 1997 show very little vertical and temporal variabilities, and comparatively low bottom temperatures. No signs of inflow activity could be identified at this early stage. However, the profiles taken on 17-18 February 1998, more than 3 months later, exhibit a dramatically different picture. The potential temperature had strongly increased below 60 m, and peak values near the bottom increased from 5.3 °C (31 August 1997) to 7.2 °C (18 February). The near-bottom potential densities rose from $\sigma_\theta = 9.55$ kg/m^3 to $\sigma_\theta = 9.85$ kg/m^3, and water denser than the pre-inflow maximum were then found in the entire depth range below 165 m (not shown).

The inflowing water masses are seen to occur as intrusions, causing high vertical and temporal variability in the temperature profiles. Note that only very little vertical/ temporal variability was observed below approximately 210 m depth. This suggests that the renewal of the near-bottom waters was already completed on the 18 February 1998. Above this level, however, especially in the intermediate layer (90-170 m), these intrusions generated strong vertical

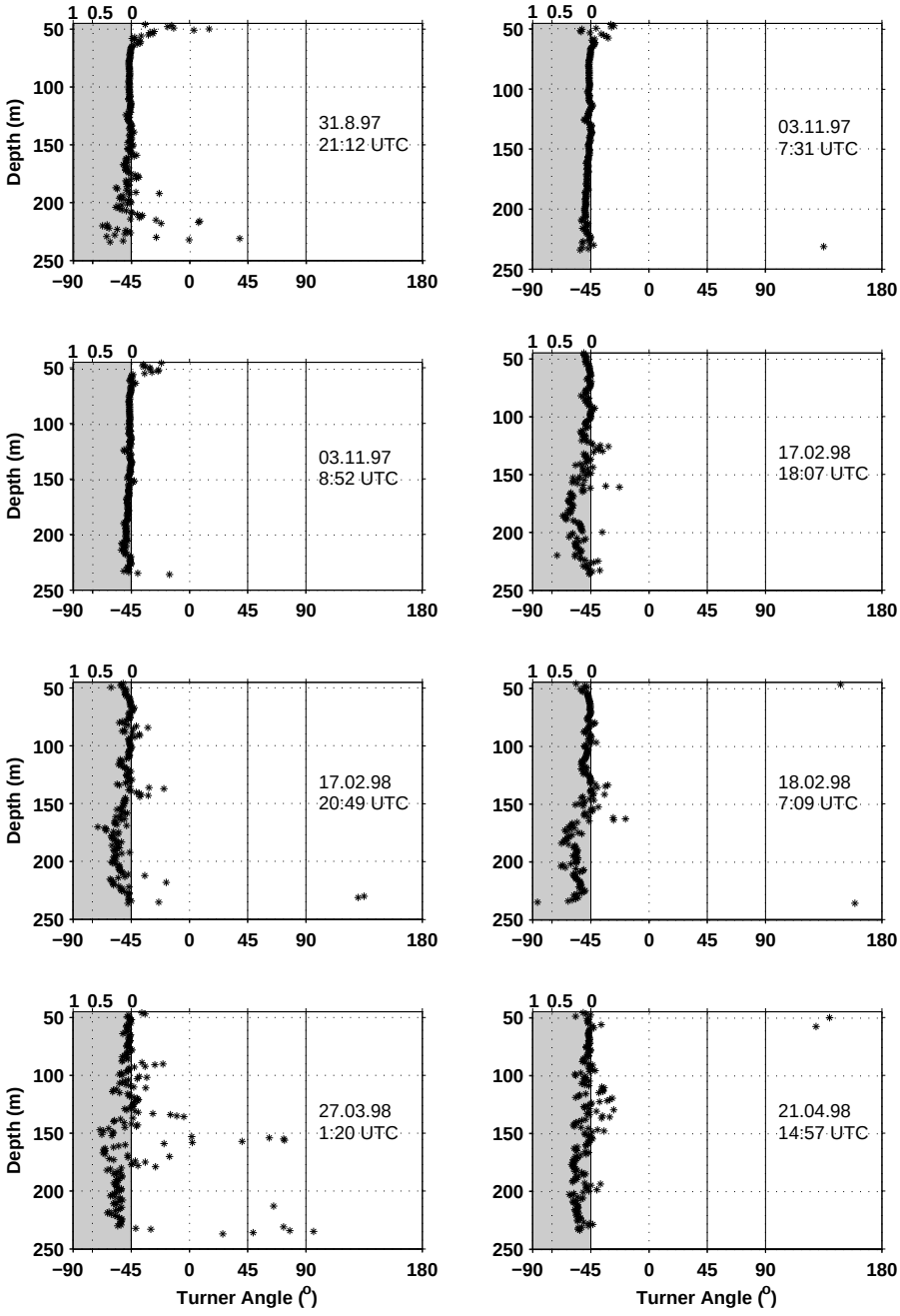

Figure 3.8: Turner angles vs. depth profiles of monitoring station BMP271 between 31 August 1997 and 21 April 1998. Grey area indicates diffusive convective regime ($-90\,^\circ < \mathrm{Tu} < -45\,^\circ$). Top x-axis indicates associated density ratios for $R_\rho = 0$, 0.5, and 1. Sampling time given as dd.mm.yy HH:MM UTC.

temperature gradients which may have affected the stability parameters in the double-diffusive regime. To investigate this effect, the Turner angles defined in (3.2) were computed for all measured profiles. The results are displayed in Fig. 3.8, and illustrate that diffusive-convective conditions prevail, consistent with the stabilising effect of salinity and the destabilising effect of high temperatures from the inflowing water.

Date	31.8.1997,	03.11.1997,	03.11.1997,	17.2.1998,	17.2.1998,	18.2.1998,	27.3.1998,	21.4.1998,
UTC	21:12h	07:31h	08:52h	18:07h	20:49h	07:09h	01:20h	14:57h
$\langle R_\rho \rangle$	0.044	0.060	0.059	0.220	0.221	0.238	0.164	0.184
Std Dev $\langle R_\rho \rangle$	1.219	0.032	0.035	0.133	0.165	0.116	0.458	0.090
$\langle Tu \rangle$	−47.49	−48.45	−48.39	−57.38	−57.44	−58.39	−54.30	−54.45

Table 3.2: Vertical averaged density ratio $\langle R_\rho \rangle$ with the standard deviation (Std Dev) and vertically averaged Turner angles $\langle$Tu$\rangle$ of BMP271 between 170 - 235 m for profiles shown in Fig. 3.8.

According to Zhurbas and Paka (1999) and Kuzmina et al. (2005) active turbulence in diffusive convection requires values of $R_\rho \sim 1/15 = 0.067$ (Tu $= -48.81\,^\circ$). Resulting vertical averages were computed for R_ρ and TU with corresponding standard deviations for the fully enclosed part of the basin below 170 m depth (Table 3.2). Here, vertically averaged θ and S gradients were used to calculate R_ρ and Tu. In general, all averages suggest a shift of Tu towards values reflecting diffusive convective conditions triggered by the deep warm-water intrusion. The only exception results from the profile sampled in March, Fig. 3.8. Its R_ρ values exhibits the highest standard deviation (see Fig. 3.8) of all profiles with Tu values pointing to the above mentioned cases (ii) and (iii), i.e. to the stable and salt-fingering mixing domains. However, such extreme values of Tu near the bottom are irrelevant for double-diffusive processes given the fact that the dominating process here is bottom boundary mixing. The two profiles from 17 February 1998 had the highest values of the density ratio close to 0.5 at 223 and 170 m, respectively. In all other profiles (except the two November profiles) values close to $R_\rho \approx 0.25$ could be detected. Due to the absence of direct turbulence measurements it is difficult to conclude if double-diffusion did actually occur. Nevertheless, presented estimates of the R_ρ / Tu values suggest that diffusive convection essentially controls the diapycnal mixing within intermediate layers (90-170 m), especially in the wake of deep warm-water intrusions reaching the EGB.

3.2.4 Salinity and heat budgets

Estimates for the effective diffusivities in the deepest layers of the EGB may be obtained from basin-scale scalar budgets as suggested e.g. for the Baltic Sea by Stigebrandt (1987) and Axell (1998), as well as for some semi-enclosed deep basins off the Californian coast by Ledwell and Hickey (1995).

Here, the starting point is selected to be the salinity budget for a fixed control volume, V, underneath a level surface, A_t, located at the vertical position $z = z_t$,

$$\frac{\mathrm{d}}{\mathrm{d}t}\int_V S\,\mathrm{d}V = -\int_{A_t} Sw\,\mathrm{d}A - \int_{A_t} F_S\,\mathrm{d}A\ , \tag{3.3}$$

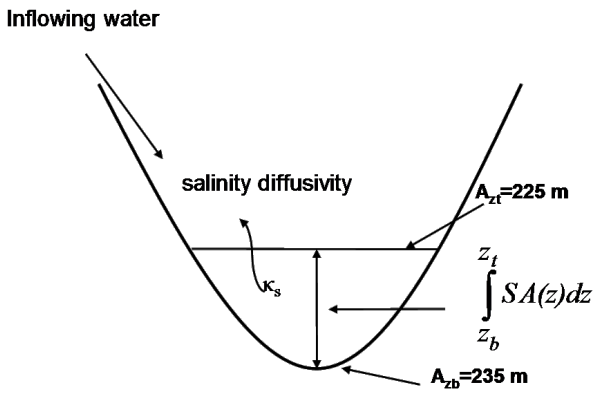

Figure 3.9: Sketch of salinity/ heat budget calculations in the EGB for profiles in shown Fig. 3.10.

where w and F_S denote the vertical (upward) components of the velocity and the turbulent salt flux, respectively. The only assumption involved in the derivation of (3.3) is the absence of advective and diffusive fluxes at the sediment-water interface. Defining the volume-averaged salinity,

$$\langle S \rangle_V = \frac{1}{V} \int_V S \, \mathrm{d}V \ , \tag{3.4}$$

the salinity budget, (3.3), can be re-written without further assumptions as an expression for the area-averaged turbulent salt flux across A_t,

$$\bar{F}_S = \frac{V}{A_t} \left(\frac{\bar{S}_I - \bar{S}_O}{T_R} - \frac{\mathrm{d}\langle S \rangle_V}{\mathrm{d}t} \right) \ , \tag{3.5}$$

where $T_R = V/Q$ denotes the formal residence time determined by the overall flux, Q, of water entering the control volume through A_t with upward velocities $w < 0$. $\bar{S}_I$ and $\bar{S}_O$, respectively, denote the transport-weighted average salinities of inflowing (I) and outgoing (O) waters. Hence, the turbulent salt flux can be estimated from the evolution of the average salinity inside the control volume, and the properties of incoming and outgoing advective fluxes. Equation (3.5) can be also developed for potential temperature, as well as for any other scalar quantity with negligible sediment fluxes and internal sources.

On the other hand, it becomes clear that any advective fluxes affecting (3.5) will, in general, not be known. Nevertheless this equation is still useful to obtain minimum values for the vertical fluxes and diffusivities under certain conditions. One of them is given by the fact that below the enclosing isobath of 170 m the deep water renewal is driven by dense saline gravity currents. Associated saline intrusions enter the control volume as a volume flux, Q, across the level surface, A_t, with high salinity, $\bar{S}_I$, causing upwelling of an equal flux, Q, of low-salinity water at other locations due to continuity. This scenario implies that the first term on the right-hand side of

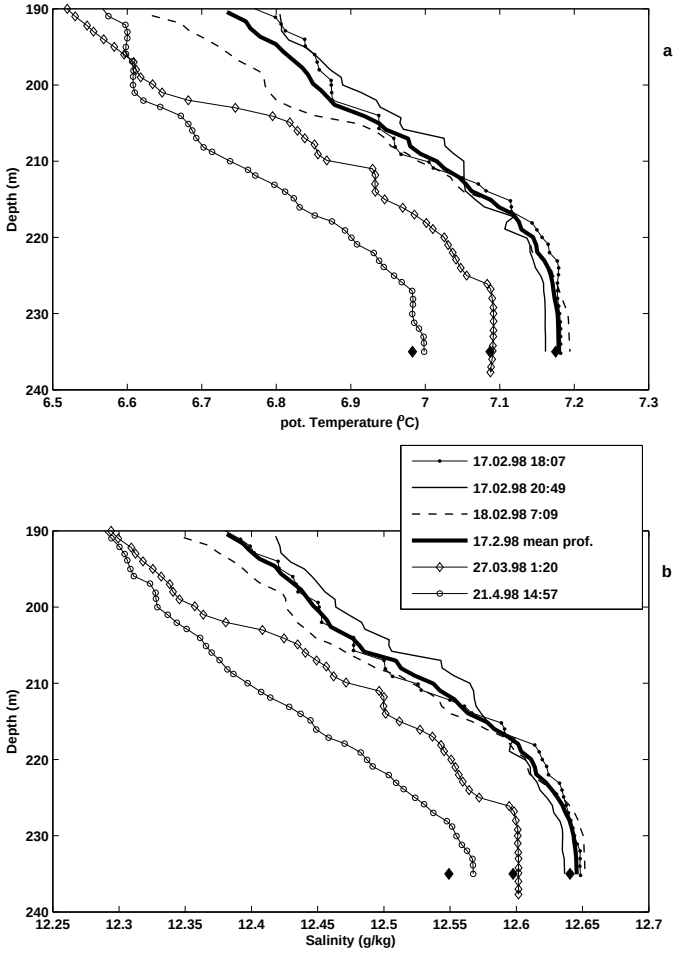

Figure 3.10: (a) Potential Temperature vs. depth, (b) salinity vs. depth of BMP271 on 17-18 February 1998, 17 February 1998 (mean profile), 27 March 1998 and 21 April 1998. Sampling time given as dd.mm.yy HH:MM UTC. Diamonds represent the corresponding potential temperature and salinity averages of the basin's volume between 225-235 m.

(3.5) will be positive. In situations where the rate term on the right-hand side of (3.5) is negative, i.e. where deep water renewal by advection is weak but not necessarily negligible compared to vertical mixing, expression (3.5) yields

$$\bar{F}_S = -\bar{\kappa}_S \overline{\frac{\partial S}{\partial z}} \geq -\frac{V}{A_t} \frac{\mathrm{d}\langle S \rangle_V}{\mathrm{d}t} \ , \tag{3.6}$$

corresponding to lower bounds for the averaged flux, $\bar{F}_S$, and the average vertical diffusivity, $\bar{\kappa}_S$, at $z = z_t$. Note that $\bar{\kappa}_S$ is only implicitly defined by the first equality in (3.6), and by the way the averaged vertical gradient, $\overline{\partial S/\partial z}$, is computed.Interestingly, for so-called warm inflow events, as observed here, incoming waters are characterised by high salinities *and* high temperatures, such that identical arguments lead to lower bounds, analogous to (3.6), for the potential temperature flux, $\bar{F}_\theta$, and diffusivity, $\bar{\kappa}_\theta$.

The rate term appearing in (3.6) was estimated from finite differencing the volume average, $\langle S \rangle_V$, at three different dates starting on 17 February 1998 (see Table 3.3). CTD-profiles taken near the centre of the basin (Fig. 3.7) illustrate that after a strong increase of bottom temperatures during the warm inflow event, all near-bottom temperatures and salinities (compare Fig. 3.10 b) following 17 February 1998 continuously decreased. This indicates that by this date bottom-water renewal by advection is no longer the dominating process such that the necessary conditions for the applicability of (3.6) are satisfied. Using the regression in equation 4.10 suggested by Hagen and Feistel (2001), the volume-averaged salinities at the dates shown in Table 3.3 were estimated from salinity profiles taken at the central monitoring station BMP271 according to

$$\langle S \rangle_V = \frac{1}{V} \int_{z_b}^{z_t} S(z) A(z) \, \mathrm{d}z \ , \tag{3.7}$$

where horizontal homogeneity is assumed. An analogous procedure was used to obtain estimates of the volume averaged rate of change of potential temperature.

Two questions immediately arise from this approach: (a) How representative are temporal snapshots from a CTD profile in the presence of possible short-term fluctuations, and (b) to what extent can profiles measured in the basin's centre be used to represent basin-scale volume averages? To obtain an answer for the first question, the temporal variability from short-term fluctuations, likely caused by near-inertial wave motions, has been investigated. Three different CTD casts were compared, obtained between 17 - 18 February 1998 within a period of 13 h, i.e. within slightly less than one inertial period of about 14 h. Resulting profiles(Fig. 3.10) demonstrate that in the lowest 20 m of the water column the temporal variability is much smaller than the long-term spatial decay of salinity and temperature. The average of these three profiles will be identified as "Profile 1" on 17 February 1998 (see Table 3.3).

Although the above mentioned assumption of spatial homogeneity in S and θ turned out to be more demanding, it can be justified only for densest water masses below 225 m depth where both quantities exhibit a small lateral variability, see Fig. 3.3 and Fig. 3.5. Therefore, equation (3.7) was evaluated for a volume below $z_t = -225$ m with a small volume correction for profiles that did not reach the deepest part of the basin. The resulting averaged salinities and temperatures for the three dates are compiled in Table 3.3 and marked in Fig. 3.10.

Based on the profiles shown in Fig. 3.10, the mean gradients $\overline{\partial S/\partial z} \approx -0.0075$ (g/kg)/m were estimated for salinity and $\overline{\partial \theta/\partial z} \approx -0.0118$ K/m for potential temperature between 205 and 225m. Thereafter the lower bounds for the fluxes and diffusivities were computed, Table 3.4. Finite-differencing over the whole time window of these three profiles resulted in $\kappa_S = 1.6 \times 10^{-5}$

Date (ID)	$\langle S \rangle_V$ (g/kg)	$\langle \theta \rangle_V$ (°C)
17.02.98 (1)	12.64	7.18
27.03.98 (2)	12.60	7.09
21.04.98 (3)	12.55	6.98

Table 3.3: Volume averaged salinities and temperatures, computed at the dates indicated in the first column. For later reference, the profile IDs are given in brackets.

Profiles	$\bar{F}_S \times 10^{-7}$ (g/kg m/s)	$\bar{F}_\theta \times 10^{-7}$ (K m/s)	$\kappa_S \times 10^{-5}$ (m^2/s)	$\kappa_\theta \times 10^{-5}$ (m^2/s)
Δ_{31}	1.2	2.5	1.6	2.1
Δ_{21}	0.9	1.9	1.3	1.6
Δ_{32}	1.5	3.3	2.1	2.8

Table 3.4: Lower bounds for vertical fluxes and diffusivities computed according to (3.6) using the values compiled in Table 3.3.

m^2/s and $\kappa_\theta = 2.1 \times 10^{-5}$ m^2/s. Corresponding values computed for the first and second half of the interval are consistently lower or higher, respectively, than these average values. Overall, however, diffusivities computed by this method agree within approximately 30 %.

3.2.5 Decay of temperature variance

Higher up in the water column, the application of the budget method is a less reasonable tool to estimate diffusivities associated with the mixing between intrusions and ambient waters. The main difficulties arise from the fact that above approximately 170 m the basin cannot be considered as "closed" any more, and lateral advection becomes an uncontrollable parameter. Nevertheless, it is clearly desirable to obtain diffusivities also for the regions directly below the halocline where the intrusion activities are strongest. As a useful alternative to the budget method, we suggest here an idealised model for the decay of temperature variance associated with the intrusions that, as will be shown in the following, leads to an order-of-magnitude estimate for the diffusivity of heat.

To this end, a statistically homogeneous volume of water is considered where temperature variance, $\langle \theta'^2 \rangle$, is created due to temperature fluctuations, θ', associated with the presence of intrusions. Ignoring all processes creating temperature variance for the moment, and assuming that mixing between intrusions and ambient water is dominated by vertical diffusion, temperature fluctuations evolve according to

$$\frac{\partial \theta'}{\partial t} = \kappa_\theta \frac{\partial^2 \theta'}{\partial z^2} \ . \tag{3.8}$$

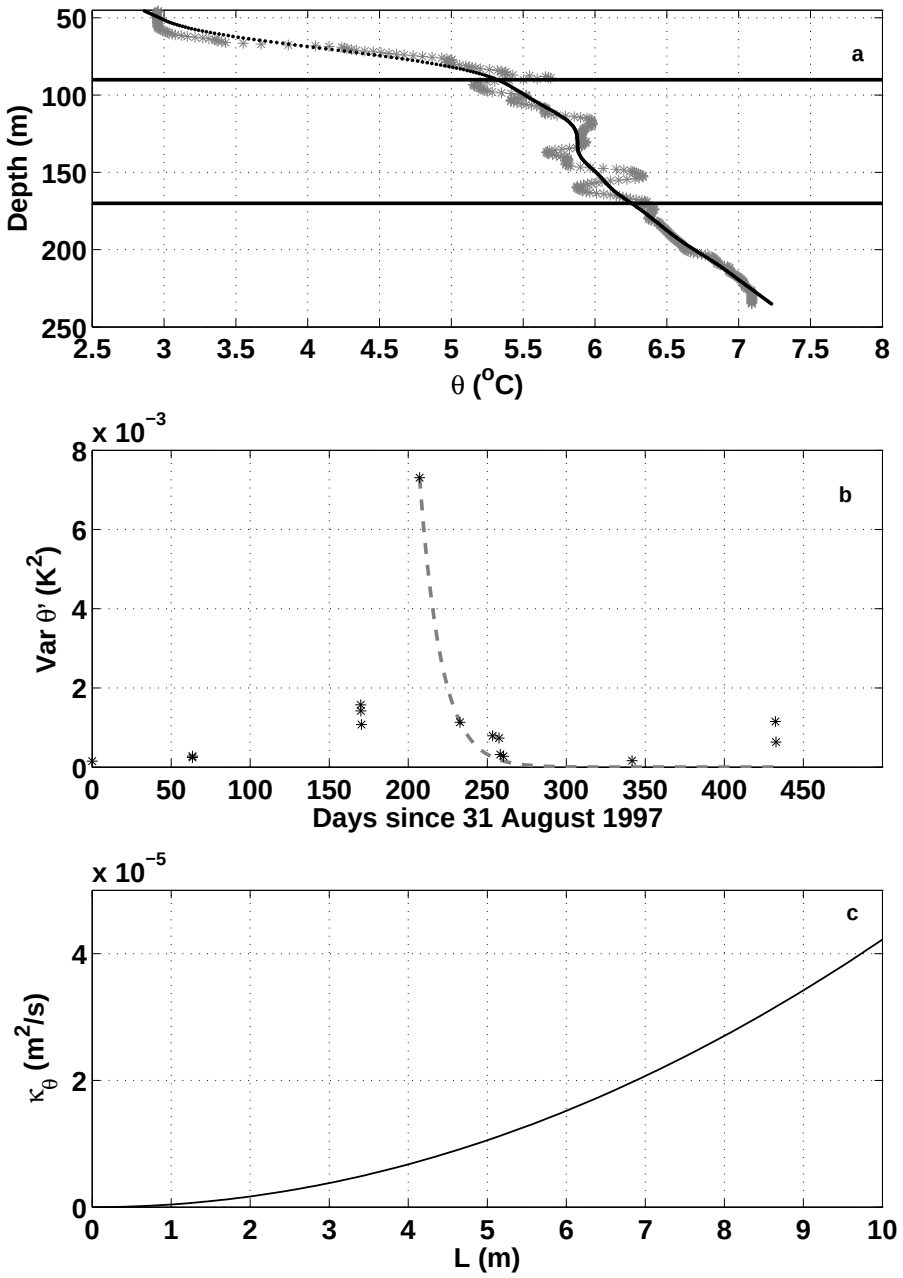

Figure 3.11: (a) Potential temperature profile from 27 March 1998, filtered with a cut-off length of 3 m (grey stars) and 50 m (black dots). Horizontal lines indicate the intrusion layer (90-170 m) used for the analysis; (b) time series of $\langle \theta'^2 \rangle$ (stars) for all available temperature profiles between 31 August 1997 and 7 November 1998, and exponential fit (dashed line); (c) vertical intrusion scale, L, vs. diffusivity of heat, κ_θ.

Multiplying this equation by θ' and averaging leads to an evolution equation for the temperature variance associated with the intrusions,

$$\frac{\partial \langle \theta'^2 \rangle}{\partial t} = -2\kappa_\theta \left\langle \left(\frac{\partial \theta'}{\partial z} \right)^2 \right\rangle \approx -2\kappa_\theta \frac{\langle \theta'^2 \rangle}{L^2} \ , \tag{3.9}$$

where in the last step we have assumed that vertical gradients are characterised by the standard

deviation of the temperature fluctuations, and a single, constant length scale, L, associated with the vertical scale or wave-length of the intrusions. Equation (3.9) has a simple exponential solution of the form $\langle \theta'^2 \rangle = C \exp\left(-(t - t_0)/\tau\right)$, where C denotes the variance at $t = t_0$, and $\tau = L^2/(2\kappa_\theta)$ is the time scale of decay of temperature variance.

Clearly, in realistic applications, temperature variance does not only decay. The most important additional effects not accounted for in (3.9) in our application are (a) advection of temperature variance from neighbouring regions that may either increase or decrease the locally observed variance, and (b) the local generation of temperature variance due to advective effects, i.e. the interleaving of newly generated intrusions.

In view of our limited data, we estimated θ' for individual temperature profiles by computing the difference between unfiltered and filtered temperature profiles, where the cut-off length (50 m here) was subjectively chosen such that essentially all variance associated with the intrusions was removed. The variance of θ' was then computed over the depth range 90-170 m, where the strongest intrusive activity was observed. Our estimates are based on the CTD profiles near the central monitoring station BMP271 already discussed above, and a few additional profiles from the standard monitoring program in order to study the late-stage of evolution of the intrusions. The additional profiles were taken on 12 May, 16 May, 17 May, 19 May, and 8 August 1998, and two profiles on 7 November 1998. An example illustrating the filtering procedure for the θ profile from 27 March 1998 is given in Fig. 3.11 a.

A times series of $\langle \theta'^2 \rangle$ for all available profiles near the central station is depicted in Fig. 3.11 b. This time series illustrates that variance is quickly generated during the inflow event, reaches a maximum on 27 March 1998, and then rapidly decays. During later times, the temperature variance is seen to increase intermittently, most likely due to advection into the measuring site and some small additional intrusions, but values are generally much lower than during the time of the inflow. Fitting the exponential solution to (3.9) to the period of decaying tracer variance, estimates for the decay time, τ, and thus for the diffusivity, κ_θ, may be obtained. To capture the initial period of strongest decay, we used the point of maximum variance and the following point (Fig. 3.11 b) for the fit, resulting in a decay time scale of $\tau = 13.7$ days. The diffusivity then follows from $\kappa_\theta = L^2/(2\tau)$. The quantity that is probably the least well-known in this analysis is the vertical intrusion scale, L. We have therefore plotted κ_θ for a range of plausible scales (Fig. 3.11 c); the result suggesting that κ_θ is of the order of a few times 10^{-5} m^2/s. This estimate is a lower bound, since we may not have sampled exactly at the time of largest variance, and we cannot exclude that during the decay period some variance has been created during the late-stage of the inflow event. The diffusivity during the inflow is therefore clearly enhanced

with respect to values during stagnation periods, however, it is difficult to conclude if this is a result of double-diffusive mixing or enhanced shear mixing associated with the motions of the intrusions.

Chapter 4

The Deep Circulation in the EGB (Inter-basin communication of deep Baltic basins and their effects for the deep circulation)

4.1 Hydrography of the Eastern Gotland Basin

During the RAGO field campaign in September 2006 two diagonal cross-sections were conducted to monitor the current hydrographic situation of the EGB. The first transect was conducted on the 26 September 2006 starting in the northeast corner of the basin travelling to the southwest corner. The transect contained 13 CTD profiles measuring potential temperature, salinity, oxygen and pressure (see Fig. 4.1). The second transect conducted a day later covered the area from the northwest to the southeast corner (Fig. 4.2). The location of both transects is marked in Fig. 1.1. Both transects revealed a cold, oxygen- rich inflow just below the halocline in $90-150$ m with core temperatures of 5.6°C and an oxygen concentration of 1 ml/l. The inflowing waters are easy to distinguish from the surrounding water, which contains somewhat higher temperatures (6°C) and is anoxic (0 ml/l). The inflowing water masses slope from east to west across the basin. In the East they were located directly below the halocline in depths between $90-150$m, whereas in the west they appeared in depths between 110-175 m.

Since the two transects in September 2006 only provided a snapshot of the hydrographic situation in the EGB, further investigations were made to unravel the development of the timescale of the inflow. A reliable source is the central monitoring station (BMP271, see Fig. 1.2) of the EGB,

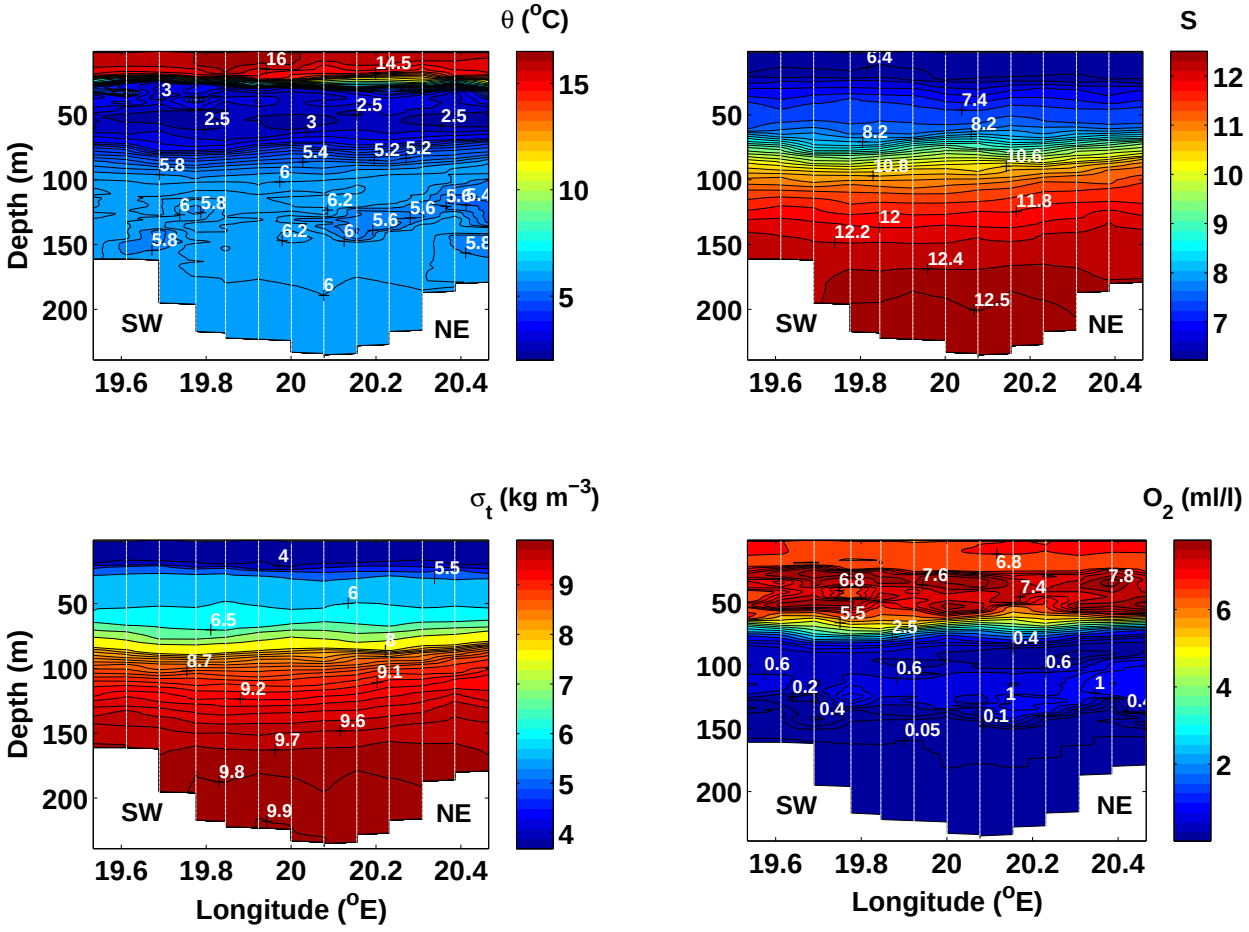

Figure 4.1: Cross-sections through the EGB from NE to SW of potential temperature (upper left), salinity (upper right), density (lower left) and oxygen (lower right panel) on 26 September 2006. The position of the cross-section is marked in Fig. 1.1.

where depth profiles of temperature, salinity and oxygen conducted in January/February, May, July, September and November 2006 revealed a high variability in temperatures and oxygen between 100 – 150 m depth (Fig. 4.3 A, B and E). Even in the rather stable salinity profiles (Fig. 4.3 C) small fluctuations were made out in those depths. Below 150 m temperatures clearly divide between warmer (January to July) and colder temperatures (September to November), Fig. 4.3 B. The oxygen in the area below the halocline exhibits a similar variability as the temperature, although there is no clear distinction between individual profiles. Highest oxygen concentrations in were measured in May 2006 in mid layers with concentrations of up to 2 ml/l. Apart from the maximum oxygen concentration in May, concentrations were rather variable. In the deepest layers of the EGB (150 – 240 m) oxygen concentrations seemed fairly uniform only in September and November they were marginally higher, but concentrations can still be

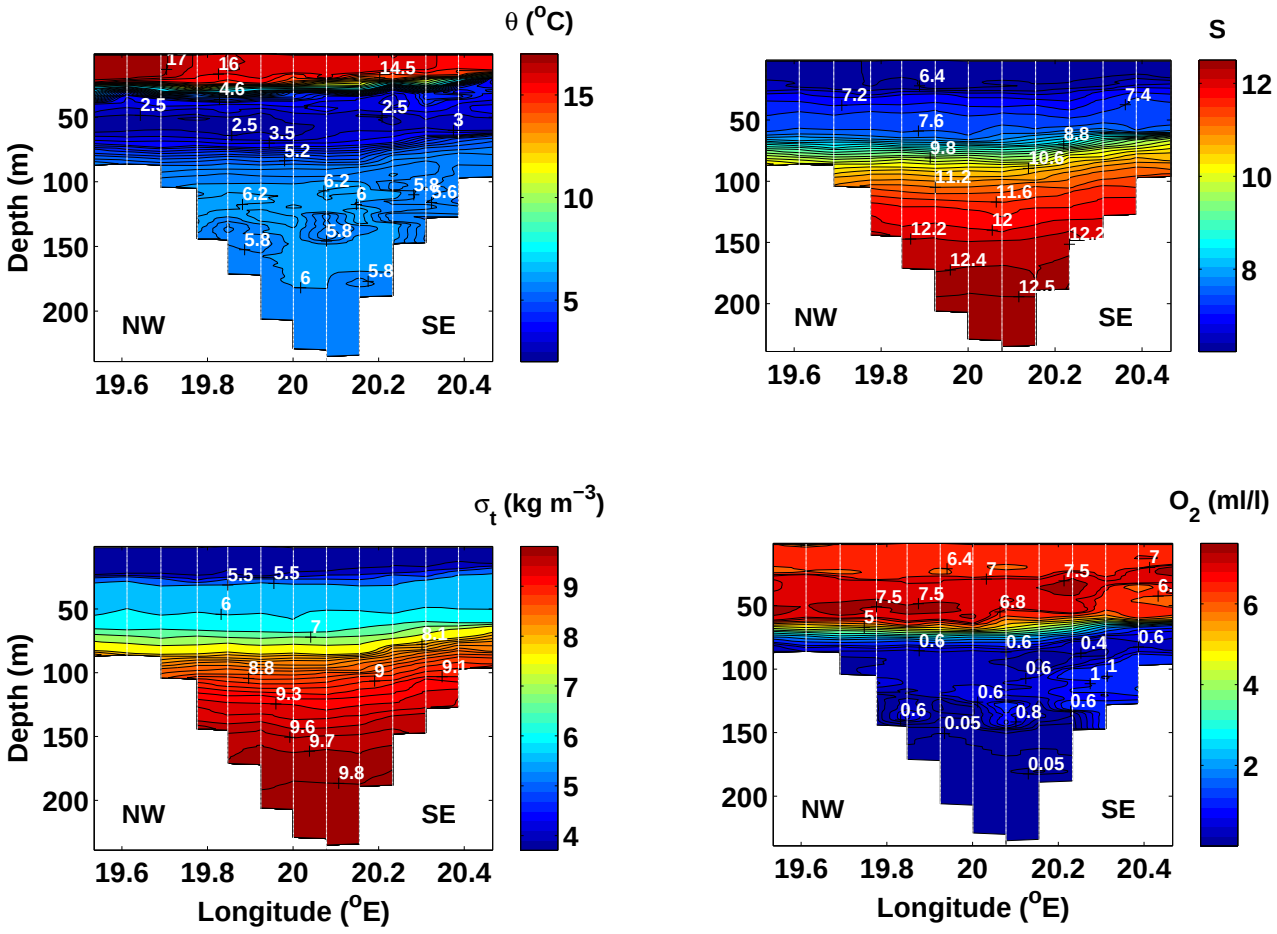

Figure 4.2: Cross-sections through the EGB from NW to SE of potential temperature (upper left), salinity (upper right), density (lower left) and oxygen (lower right panel) on 27 September 2006. The position of the cross-section is marked in Fig. 1.1.

considered as anoxic (Fig. 4.3 F). The only exemption was the 13 November when an increase in oxygen to 0.12 ml/l was measured. At the same time as the rise in oxygen, highest salinities were measured in the bottom layer (Fig. 4.3 D). From these findings it can be concluded that the inflow started in September 2006 and was visible in depths down to 230m in November 2006, when some of it reached the bottom of the basin (Fig. 4.3 F).

4.2 Propagation of temperature and current signals

The CTD profiles taken at BMP271 and the CTD transects across the basin produce a picture of the hydrographic changes in the EGB over the course of the year, but the question remains how the observed inflowing water actually circulates within the basin. Some valuable information on

the advection of the temperature signal in the EGB is provided by the three deep moorings (SE, NE and SW) deployed between May 2006 and March 2007; their positions are marked in Fig. 1.1. Unfortunately the long-term mooring NE failed to be recovered on two previous occasions and

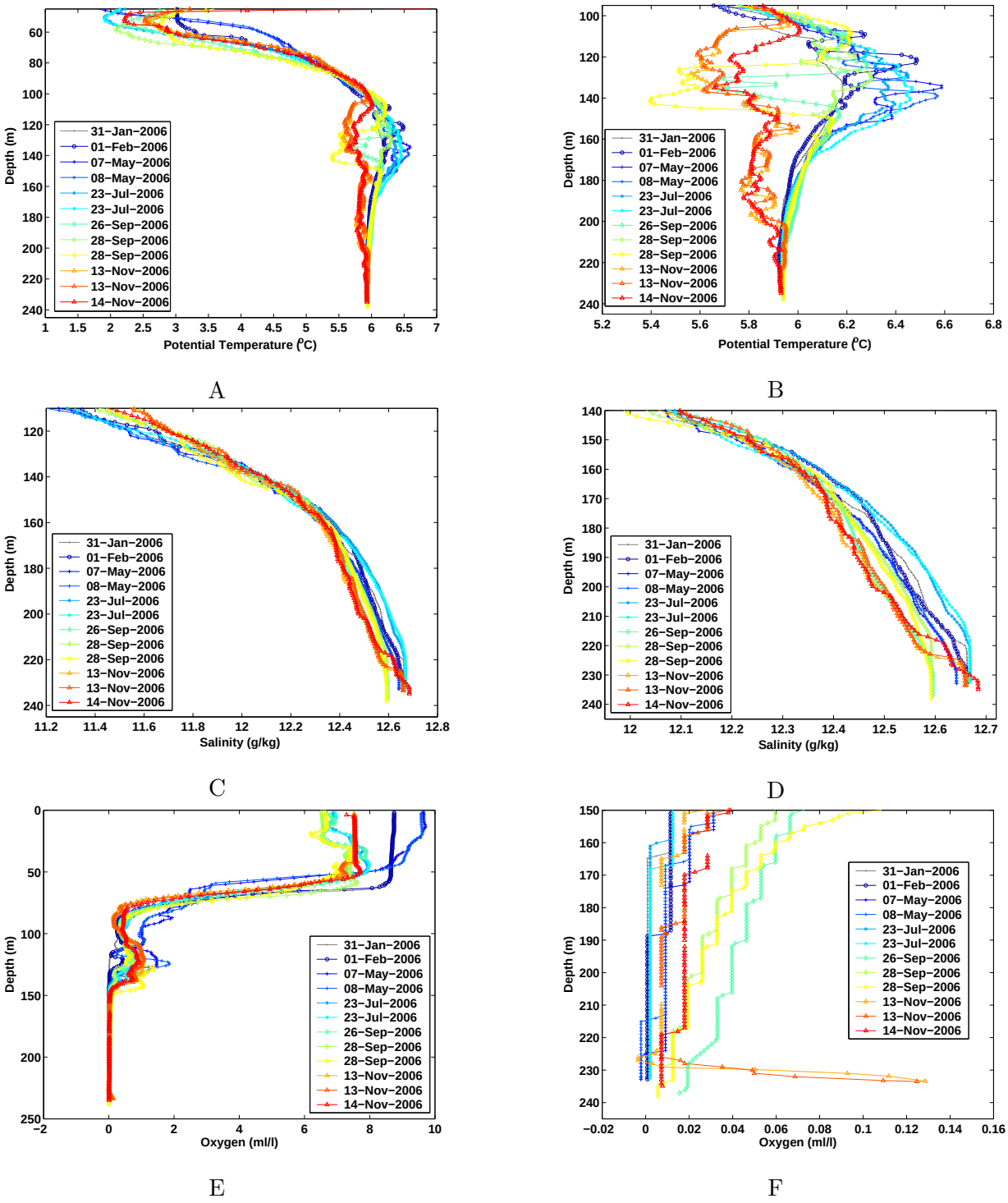

Figure 4.3: Potential temperature (A and B), Salinity (C and D) and Oxygen (E and F) depth profiles at central monitoring station of EGB (BMP271) in January, February, May, July, September and November 2006. The position is marked in Fig. 1.2.

therefore had to be replaced by a new mooring in September 2006. For this reason, the displayed temperature values in Fig. 4.5 exhibit a shorter time period than the two other moorings SE and SW. Having said that the inflow entered the basin in intermediate layers in September 2006 and as a result large parts of it were also captured by the NE mooring.

First daily temperature recordings of all three currents meters of mooring SE are analysed. The deployed instruments cover the whole enclosed deep basin with current meters in 175 m, 205 m and 220 m depth. Daily temperatures recorded by the upper most sensor (175 m) of mooring SE oscillated around 5.95°C before the inflow and were marginally higher than temperatures measured by both the mid (205 m) and lower sensor (220 m). Before the inflow was registered by the temperature sensors of the mid and lower current meter, temperatures seemed to be quite stable over larger periods of time and displayed only little fluctuations. These stable periods are not necessarily caused by well mixed water masses, but could also be due to a lack of accuracy of current meter's temperature sensors (accuracy of ±0.05°C). The inflow (see Fig. 4.4) was first recognised by the uppermost sensor around 7 September 2006 and ended around 20 September 2006. Coldest temperatures of 5.65°C were recorded by the sensors in 205 m and 220 m depth. At the end of the inflow period temperatures of upper current meter decoupled from the two lower layers. Whereas temperatures in the deeper layers between 205 m and the bottom were

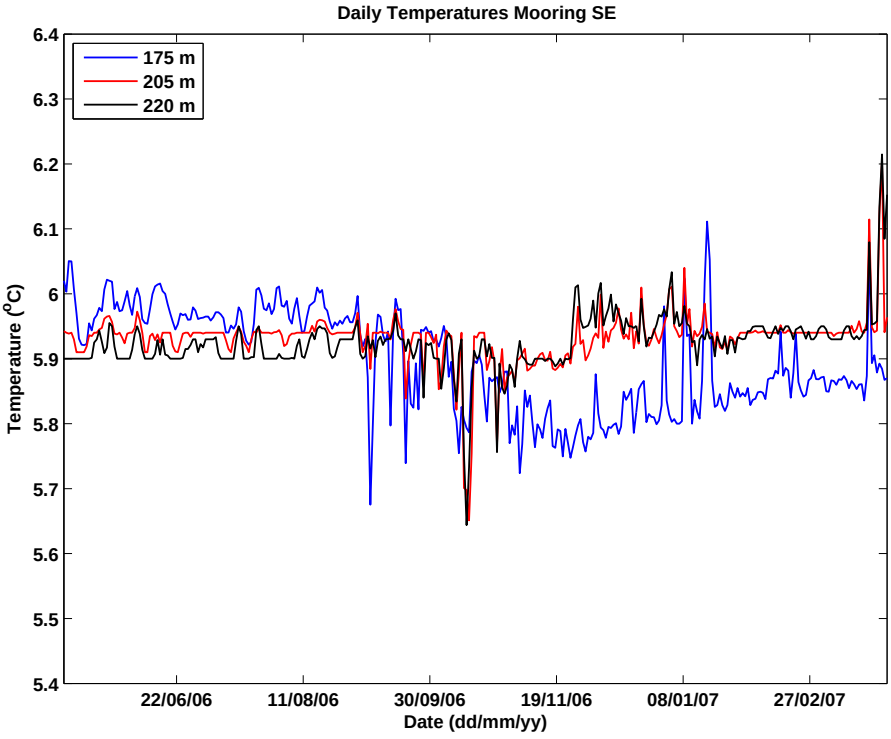

Figure 4.4: Temperatures in 175, 205 and 220 m depth of mooring SE.

warmer than in the mid layer. Temperatures in the top layer showed a higher variability during the whole measuring campaign than temperatures below 175 m depth. Two large peaks in temperature were monitored in all three sensors around 8 January 2007 and at the end of March 2007. Between those dates temperatures in 205 m and below were even more invariable than before the inflow.

The hourly current meter records (coloured red in Fig. 5.1 in the appendix) of mooring SE revealed that currents in all three depths were flowing mainly in a northeastern direction. Only on a few occasions they turned into a southerly direction. Current speeds were between $15 - 20$ cm/s until the 2 November 2006 when speeds increased to nearly 50 cm/s in around 200 m. The increase was due to a storm between the 2 and 3 November and was visible in all three current meters, although the wind had no instantaneous effect on the deep water. Peak velocities were recorded by the top current meter in 175 m on the 3 November between $0 - 6$ am, by the current meter in 205 m on the 3 November at 12 pm and by the bottom current meter in 220 m 20 hours later on the 4 November at 8 am. These delays in maximum currents speeds show that the storm event affected the whole deep basin, but not equally across the whole water column. After the storm event current speeds were higher in general with the deepest current meter recording the highest speeds, the mid current meter lower speeds, whereas the speeds of top current meter were even lower than in 205 m. Only on one occasion speeds rose to over 30 cm/s at around the end of January 2007.

Further north in the EGB the first noteworthy sharp decrease in its daily temperature records was recognised by the top current meter of mooring NE (see Fig. 4.5) at around 12 October. These large temperature variations continued until 9 November 2006. Though it cannot be ruled out that the start of the inflow was not recorded by mooring NE since recordings from the beginning of September are not available. Lowest temperatures (5.67°C) were visible in the mid and lower temperature records of current meters in 208 and 223 m depth, a few days after the first decrease was recognised by the top sensor. Daily temperatures measured by the top sensor in 178 m were slightly lower after the inflow than temperatures measured by the mid and lower sensor. After temperature variations of all sensors decreased by 9 November temperatures measured by the top current meter were colder and had decoupled from temperatures of the mid and bottom sensor until the beginning of January, when a temperature rise was noted by all three sensors. Between mid January and mid March daily temperature records of all three current meters were quite similar, whereas the highest variability appeared in 178 m and near the bottom temperatures were almost homogeneous. By mid/end of March a rise in temperature of all three current meters was recorded.

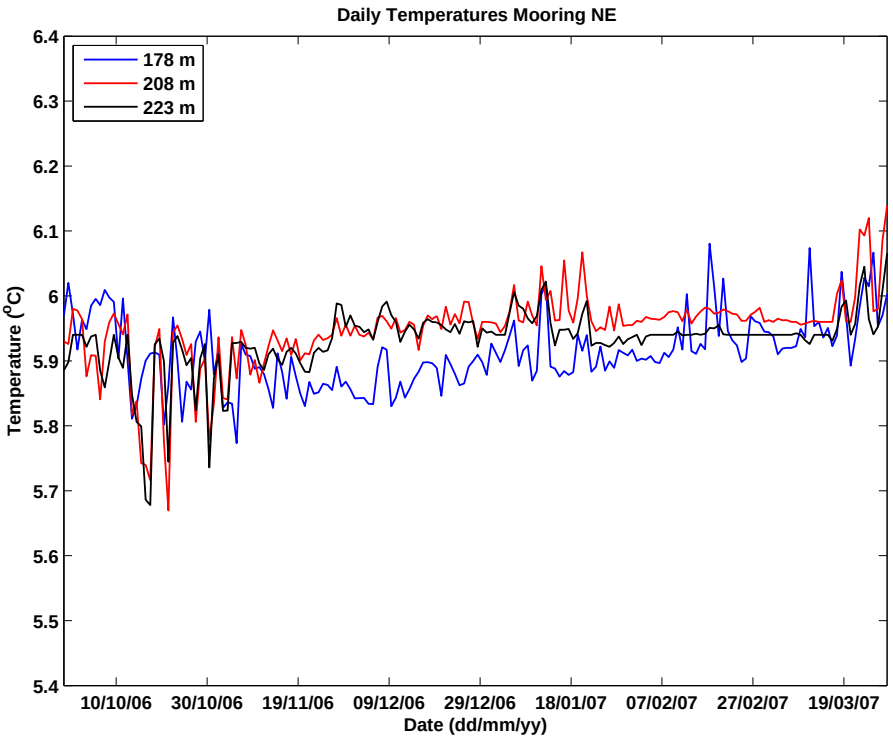

Figure 4.5: Temperatures in 178, 208 and 223 m depth of mooring NE. Note the different time scale compared to other two moorings.

Comparing hourly values of mooring NE's current directions with the directions of mooring SE, it is noticeable that mooring NE's current directions are not as a stable as directions of mooring SE. Although the general direction of currents measured by NE was north, alternating between northeast and northwest (see Fig. 5.2 in the appendix). Changes to southerly directions occurred more often than in mooring SE. Two pronounced events with high current speeds are noteworthy, the first on the 3 November 2006 with speeds between 25 cm/s and 30 cm/s and the second at around mid-end of January 2007 with speeds of around 25 cm/s. Before the increase in January 2007 speeds were on average around 10 cm/s, afterwards slightly higher. In general current speeds were far more varied and not as homogeneous as in mooring SE and changes in direction seemed to occur in pulses.

At the start of the recordings daily temperature records of mooring SW in 170 m (Fig. 4.6) were more varied and also somewhat warmer than temperatures in 200 m and 215 m depth. Temperatures measured by the deepest sensor showed the least variability. The cold inflow recorded by mooring SW was first recognised on 30 September by the top sensor in 170 m and lasted until 14 December 2006. The inflow signals had a delay of nearly two weeks before a drop in temperatures was recognised by the mid sensor. Temperatures recorded by the deepest current meter

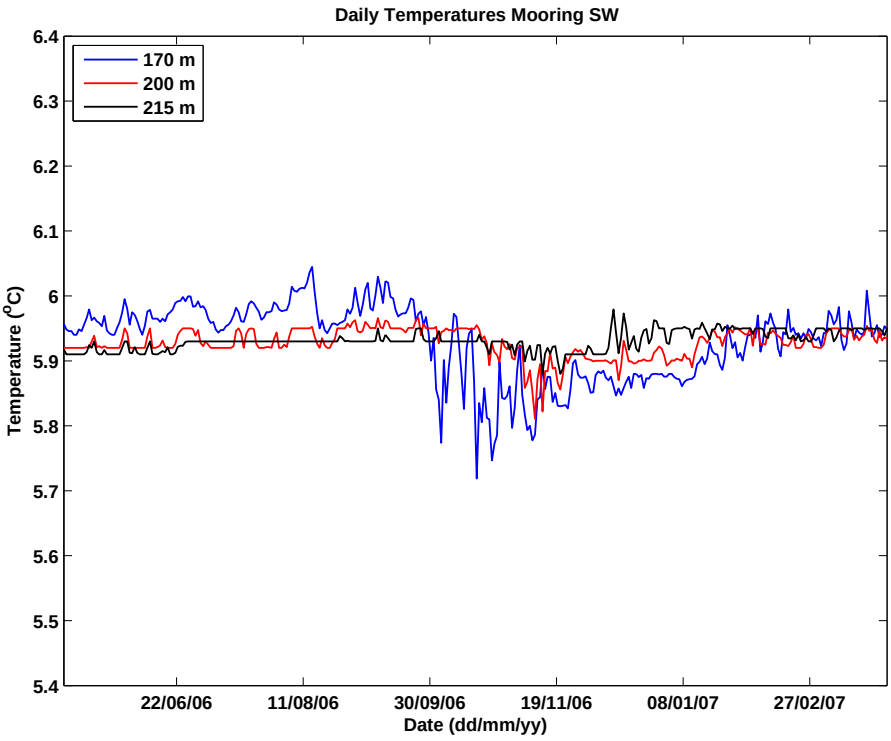

Figure 4.6: Temperatures in 170, 200 and 215 m depth of mooring SW.

showed only minimal changes and little variations. Coldest temperatures (5.7°C) and biggest variations where recorded by the sensor in 170 m depth. For about a month temperatures of all three sensors were separated, with the coldest temperatures in 170 m, temperatures in 200 m becoming slightly warmer and the deepest sensor in 215 m recording the highest values, until around 20 January 2007 when temperatures in the upper and mid sensor rose and temperatures of the water column below 170 m oscillated around 5.95°C. Naturally the top temperature sensor in 170 m showed the biggest temperature variations throughout the whole deployment period, since the basin is closed from 170 m downwards and intrusions are more likely in these parts than in the deep enclosed parts of the basin. The deep parts of the basin are expected to be much more quiet and homogeneous unless inflowing waters cause disturbances. Variances calculated for all temperatures confirm that temperatures of mooring SE and SW's top temperature sensors showed highest variances and bottom sensors showed lowest variances. Mooring NE's mid temperature sensor had highest variances of all three temperature sensors, whose values are biased due to its shorter time series.

Mooring SW exhibited the lowest hourly and daily current speeds (see Fig. 5.3 in the appendix) of all three moorings. Current meters of all three depths recorded low hourly current speeds of around $5-10$ cm/s. Current directions frequently change between northeasterly and south-

westerly directions in which a general direction can not be determined. During the storm event highest currents of about 35 cm/s were recorded by the mid and deep current meters (slightly lower speeds in the top current meter) travelling in a northerly direction on 2 November 2006 around 0 am and alternated to a southerly direction with speeds up to 25 cm/s 20 hours later. Two other pronounced increases in current speed could be made out, one in the middle of December 2006 and the other at end of January 2007. The event in January although was the stronger one of the two with speeds again of about 20 cm/s both in northeasterly and southwesterly directions. After the storm event current speeds were in general higher than in the first 6 months of the recordings.

Summing up, by looking at all three depths the highest temperature range was recorded by mooring SE, mooring NE exhibited a slightly smaller range and a strongly limited temperature range was encountered in the SW mooring. Mooring SW showed the least temperature variability of all three moorings. Comparing all the uppermost current meters sitting in about 50 m depth above the bottom, it's not clear whether the inflow was noted first by mooring SE or NE, mainly because the records of NE started on 20 September due to the re-deployment of the mooring. Looking at mid sensors at about 20 m above the bottom and lowest sensors sitting at 5 m above the bottom the inflow was first visible in mooring SE, then in mooring NE and last in mooring SW. The time lag between mooring SE and mooring SW amounted to about three weeks, the lag between mooring SE and mooring NE cannot be determined due to missing data. The current meter records do not show any evidence of the inflow, in comparison to the temperature signals. The variability mainly corresponds to wind effects rather than to the inflowing water masses. This becomes obvious when examining the current speeds of moorings SE and SW before and after the storm event where current speeds were faster after the storm than before. It seems the storm initiated an additional oscillation in deep EGB.

The moorings deployed within the EGB give an impression on the circulation and the development of inflowing waters which leads to the question on how much of the beforehand described effects are due to external steering or other choke points on its way from the Kattegat to the EGB, i.e. the Stolpe Channel. To investigate the role of the Stolpe Channel in more detail, two ADCPs were deployed at 17.5°E on either side of the channel in 75 m depth.

4.3 The Stolpe Channel

4.3.1 Hydrography of the Stolpe Channel

Prior to the deployment of the two ADCPs SFN and SFS (location see Fig. 1.1) at the outlet of the Stolpe channel two hydrographic sections were conducted in a north-south direction at 17.5°E on 22 September and repeated seven days later on 29 September 2006. The two CTD transects are marked in Fig. 1.1. In both transects a core of cold (2.1°C) and oxygen-rich (7.8 ml/l) water was detected in depths between $40 - 55$ m. Similar conditions were also captured some months earlier in May 2006 in the monitoring data of the Stolpe Channel's central station BMP222 (Fig. 4.7, position see Fig. 1.1). Since water masses with low temperatures and high oxygen levels were recorded in the hydrographic cross-sections of the EGB, it is likely that these water masses passed the Stolpe Channel either in May 2006 and arrived in the EGB in September of the same year. Or, another possibility is that the inflow water passed the Stolpe Channel some time between May and July, since bottom temperatures in July were cold and salinities high, but on the other hand oxygen values were very low (1 ml/l) so this alternative seems more unlikely.

The summerly thermocline reached to depths of 30 m both on the 22 and 29 September, see Fig. 4.8 A and B. Similar to the EGB, lowest temperatures are found just below the thermocline in depths between 30 m and 60 m. The temperature minimum was measured close to the position of ADCP SFN in a depth of $50 - 55$ m. Below 60 m temperatures were highest apart from the summerly surface waters, whereas the temperature gradient in this depth coincides with a salinity/density gradient.

On the 29 September 2006 between $60 - 70$m depth convex shaped isotherms and isohalines suggest an eddy spreading over most of the width of the channel. A strong slope in salinities and oxygen from south to north suggests an eastward geostrophic flow on the northern flank of the channel and a westward flow on the southern flank of the channel. This will be further investigated by calculating the geostrophic velocities.

4.3.2 Geostrophic velocities

As already indicated in the CTD sections of the Stolpe Channel the density interface of the deeper layers is tiled; the 7.8 kg/m^3 density interface for example is found in a depth of 52 m at SFS, but in 65 m at SFN. The mean vertical current profile of the ADCP's u-component (averaged over the 87 days of deployment) indicates a change in direction from a westward flow

to an eastward flow in a depth of 52 m in ADCP SFS. Fig. 4.13 (left panel) shows the zero crossing of the mean current of ADCP SFN from westward to an eastward direction is in a depth of 65 m.

In the *geostrophic balance* horizontal pressure gradients balance the Coriolis force resulting from horizontal currents. In the vertical the dominant acting forces are the vertical pressure gradient and the weight of the water. In the horizontal the acting forces are the pressure gradient and the Coriolis force (Stewart, 2004).

The geostrophic velocities displayed in Fig. 4.9 were calculated by calculating the geopotential anomaly between two pressure surfaces (Pond and Pickard, 1983).

$$u = \frac{\Delta\Phi_B - \Delta\Phi_A}{fL}, \tag{4.1}$$

where L is the length between the stations in m, f is the Coriolis frequency in s^{-1}. $\Delta\Phi_A$ is the anomaly of the geopotential distance between two pressure surfaces P_1 and P_2:

$$\Delta\Phi_A = \int_{P_{1A}}^{P_{2A}} \delta \, dp, \tag{4.2}$$

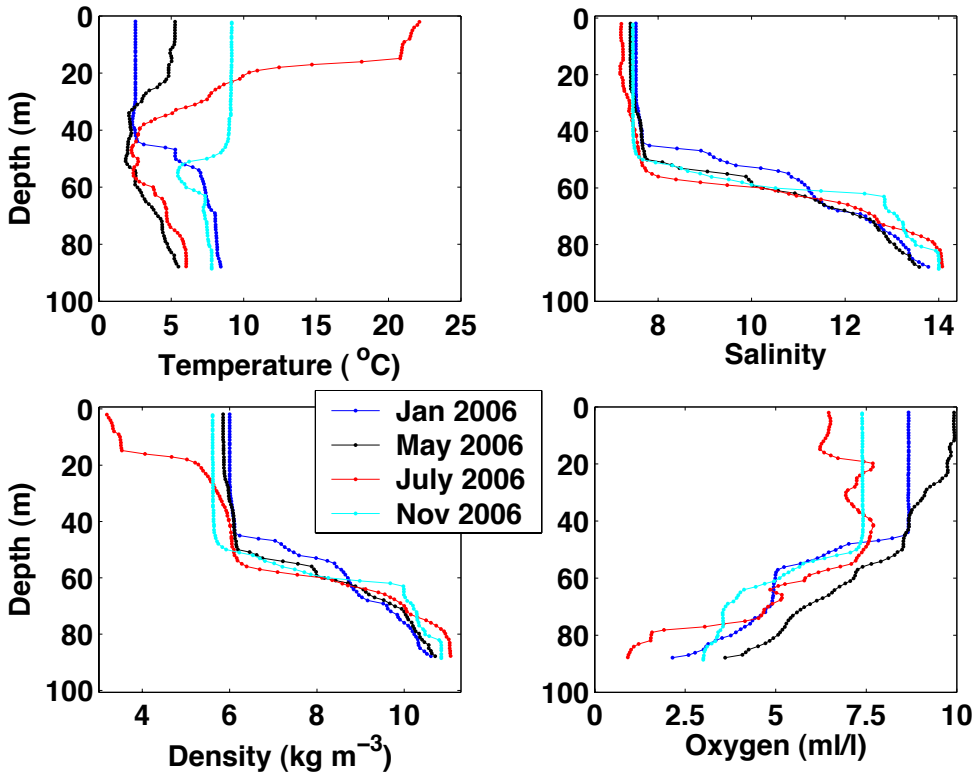

Figure 4.7: Depth profiles of temperature, salinity, density and oxygen of the central monitoring station of the Stolpe Channel (BMP222) for January, May, July and November 2006.

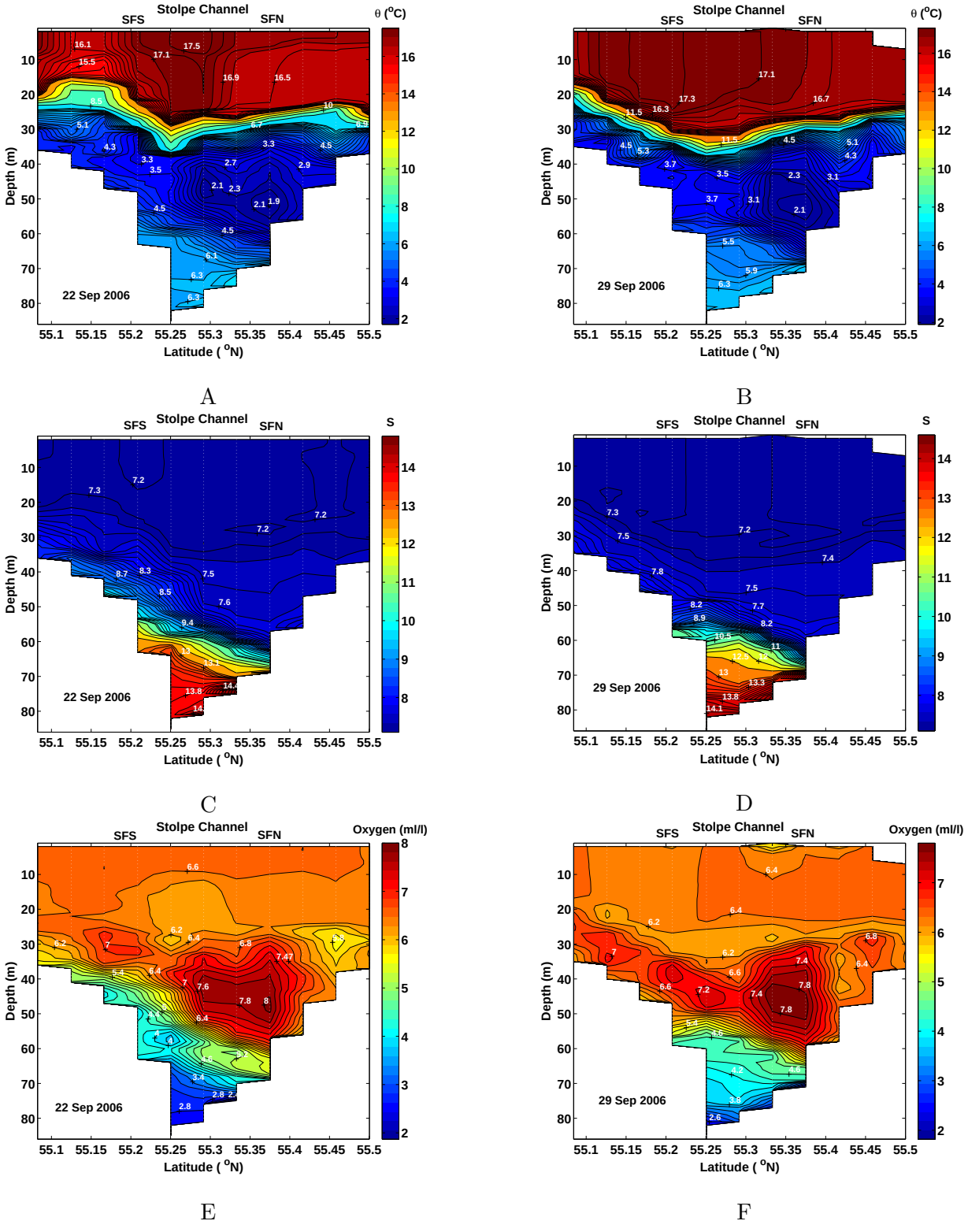

Figure 4.8: The Stolpe Channel: Meridional cross-section at longitude 17.5°E of pot. temperature vs. depth (A, B), salinity vs. depth (C, D) and oxygen vs. depth (E, F) on 22 September 2006 (left panels) and 29 September 2006 (right panels). SFN and SFS mark the locations of the ADCPs. The position of the section is marked in Fig. 1.1.

and δ as part of the *specific volume anomaly*:

$$\alpha(S,t,p) = \alpha(35,0,p) + \delta. \tag{4.3}$$

A reference level of no motion in 8 m depth with a density of 4.3 kg/m^3 was chosen, where the horizontal density gradient was smallest. Nevertheless geostrophic velocities calculated this way were 20 cm/s higher (not shown) than average velocities measured by the ADCPs. Therefore another approach was chosen where current velocities in 30 m measured by the ship-borne ADCP were coupled with the geostrophic currents obtained from hydrographic measurements. Velocities from the ship-borne ADCP (not shown) revealed a westward current between 55.20°N and 55.25°N in the upper 28 m and an eastward current between 55.3°N and 55.4°N. The depth of the currents coincides with the depth of the thermocline in the Stolpe Channel. Hence, velocities for the reference level were taken directly below the eastward current in 30 m depth and averaged between CTD stations. Resulting geostrophic velocities vs. distance are shown in Fig. 4.9 from north to south, now matching with velocities measured by the two moored ADCPs. Maximum geostrophic velocities in eastward directions did not exceed 25.0 cm/s on 22 September 2006 and seven days later the repeat of the section revealed maximum eastward velocities of 24.0 cm/s.

The comparison of the two different methods of acquiring the reference level reveals that maximum velocities of method 1 (level of no motion) are about 30 cm/s higher than velocities of the ADCP-method (ADCP data). The ADCP-method is considered more precise and also more useful as investigated by Rubio et al. (2009), who compared different methods of estimating geostrophic velocities. Rubio et al. (2009) identified the option of ADCP data as a reference level as the preferred method when the investigated area is in a coastal region and therefore rather shallow. Although problems could arise when dealing with low quality ADCP data. Method 1 suggests high eastward velocities at the southern flank of the channel and high westward velocities in the middle of the channel, whereas the ADCP-method suggests high eastward velocities at the lower northern flank of the Stolpe Channel. The ADCP-method captured eastward velocities up to 60 m on the northern flank in the water column, whereas at the repeat transect eastward velocities reached as high as 55 m on the southern flank coincides with the level of high eastward velocities measured by ADCP SFS on the southern flank of the channel (see upper left panel in Fig. 4.10). The calculation of geostrophic velocities explains only to some extent the velocities observed in the Stolpe Channel and are also just a snap shot. To investigate the amount of water transported through the Stolpe Channel over the three months deployment period other methods have to be applied.

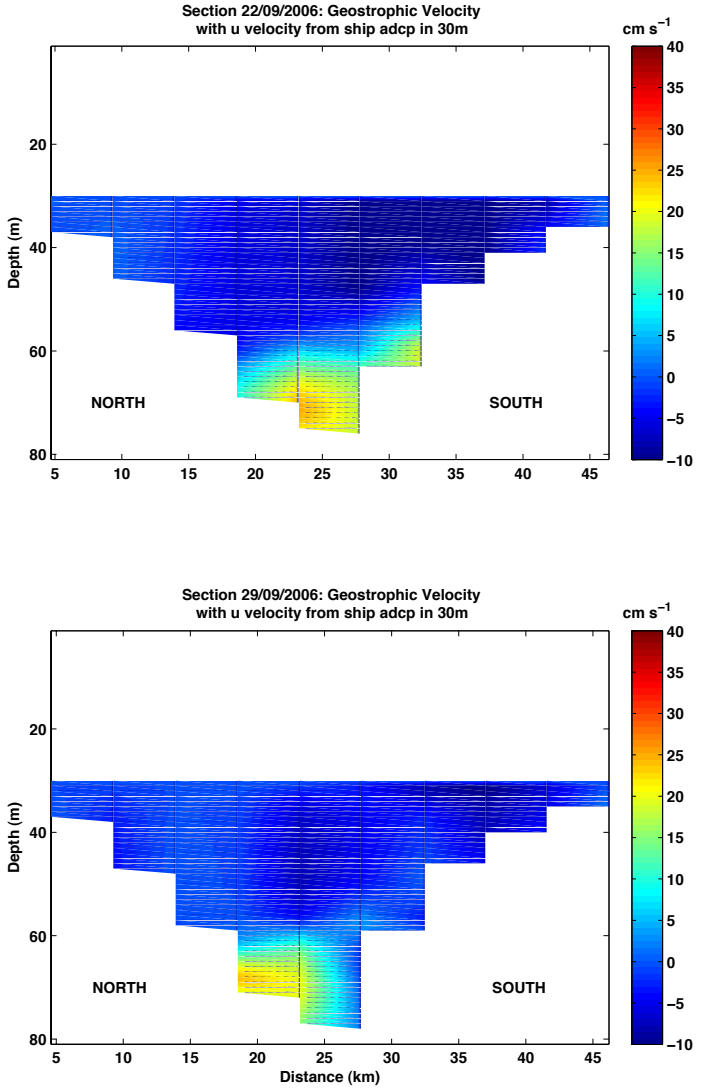

Figure 4.9: Geostrophic velocities (m/s) of the two sections across the channel on the 22 September 2006 (upper panel) and on the 29 September 2006 (lower panel) between the reference level (30 m) and the bottom.

4.3.3 Transports through the Stolpe Channel

The two ADCPs at the outlet of the Stolpe Channel were deployed at 75 m depth along 17.5°E and measured currents in a 1 hour interval at either side of the channel. Their positions are marked in Fig. 1.1. ADCP SFN was deployed at the northern flank of the channel and ADCP SFS was deployed at the southern. Simultaneous data recordings of both ADCPs were conducted between 23 September 2006 and 19 December 2006 (87 days), covering a depth between $25-71$ m. ADCP SFN (see Fig. 4.10 left panel) was a 600 kHz ADCP and therefore covered depths between $25-71$ m, whereas the 300 kHz ADCP SFS covered the whole water column.

Eastward flow of both ADCPs was mainly restricted to lower layers, between $65-71$ m for SFN and between $52-71$ m for SFS (compare Fig. 4.13). Westward flow predominated in the upper layers between $25-65$ m for SFN and $25-52$ m for SFS. Fig. 4.10 (upper right panel) gives the impression that eastward currents reached slightly higher up in the water column until highest eastward velocities were recorded in the beginning of November, but afterwards moved down again until the end of the recording period. On the northern side of the channel on three occasions (4 November 2006, $3-4$ days after the 4 November and on $17-18$ December 2006) a strong easterly flow was recorded throughout the whole water column which succeeded to break up the separation between the upper and lower layer. On the southern side of the channel (Fig. 4.10 upper right panel) the whole water column was dominated by an eastward flow on only two occasions, the 4 November 2006 and $3-4$ days later. It was more often observed that westerly flow dominated the whole water column, especially after the big storm event at the beginning of November.

Model simulations of the eastward currents of SFS indicate the good agreement between modelled and measured velocities (compare Fig. 4.11 with Fig. 4.10 upper right panel). The model was capable of replicating all major events found in the measurements. The velocities were slightly

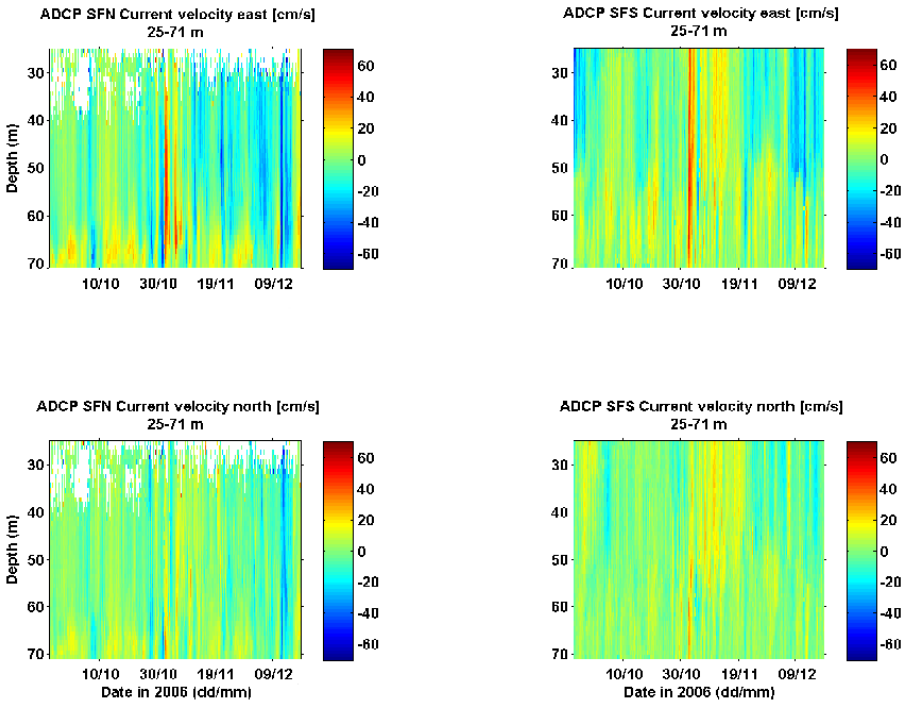

Figure 4.10: Current velocity east in cm/s for SFN (upper left), current velocity east for SFS (upper right), current velocity north for SFN (lower left) and current velocity north for SFS (lower right panel).

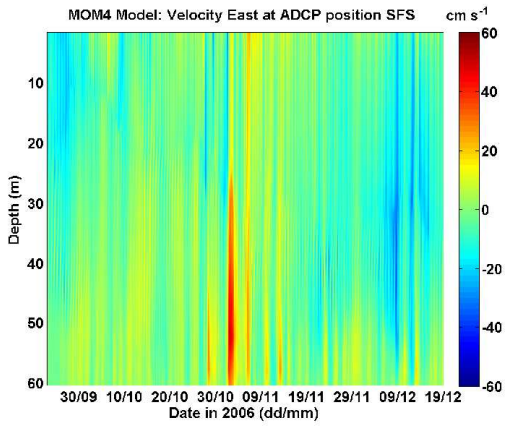

Figure 4.11: Modelled current velocities east of ADCP mooring SFS.

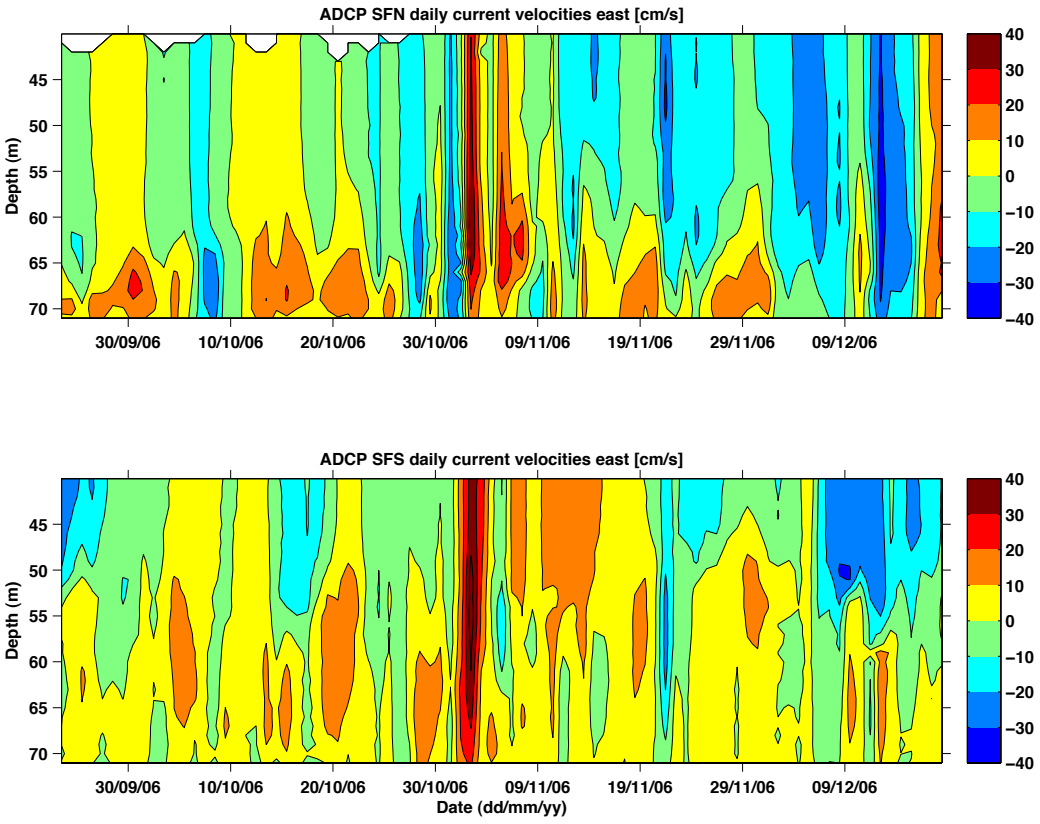

Figure 4.12: Daily zonal current velocities of ADCP moorings SFN and SFS.

lower, but all in all the model results are very good.

The flow of the eastward current seems to be pulse-like, with each pulse-like event lasting about $2-4$ days. This is more obvious in the daily currents in Fig. 4.12. Comparing the height of the eastward flow's upper boundary layer between the northern and southern flank i.e. SFN and SFS, a slope similar to the slope of the salinity/ density gradient in the hydrographic cross-

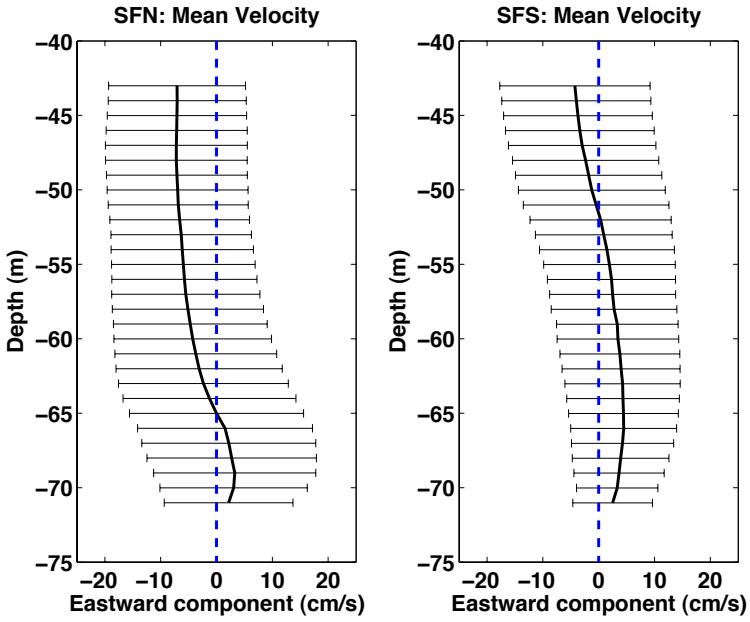

Figure 4.13: Temporal mean (23 September to 19 December 2006) of the current velocity east vs. depth with error bars for SFN (left panel) and SFS (right panel).

section was observed (compare Fig. 4.8). This south-north slope becomes more apparent in Fig. 4.13 indicating that time averaged mean velocities tend to go westward in the top layer and turn eastward in the bottom layer from 52 m to the bottom at SFS and 65 m at SFN. Fig. 4.13 shows that the eastward bottom flow at the northern flank of the channel (left panel) has only a thickness of about 6 m in the vertical, but exhibits a larger range in velocities by higher standard deviations. On the southern flank of the channel the eastward flow reached higher up in the water column with a thickness of 19 m but exhibited slightly slower velocities. After the strong storm event on 4 November 2006 longer periods of westward currents were especially at SFN observed (Fig. 4.12 upper panel). They seemed to be initiated from the surface and are presumably wind driven. Hence, associated steering mechanisms need to be investigated further, i.e. in subchapter 4.3.5.

Fig. 4.13 suggests that the time averaged deep eastward currents are geostrophically balanced; transports are calculated between the bottom of the channel and 52 m (the southern slope) and 65 m (the northern slope) of the channel. Transport velocities between the deepest measurements (71 m) and the deepest point in the middle of the channel (86 m) were depth interpolated across the channel in latitude.

Transports through the Stolpe Channel were calculated as shown in Fig. 4.14 by first calculating the area of the triangle between 52 and 65 m and the distance between each side of the channel

in a depth of 65 m by using Heron's formula [1]. Heron's formula states that the area A of a triangle whose sides have lengths a, b, and c is

$$A = \sqrt{s(s-a)(s-b)(s-c)} \tag{4.4}$$

where s is the semiperimeter of the triangle:

$$s = \frac{(a+b+c)}{2} \tag{4.5}$$

or

$$A = \frac{1}{4}\sqrt{(a^2+b^2+c^2)^2 - 2(a^4+b^4+c^4)}. \tag{4.6}$$

Transports for the triangle in Fig. 4.14 between $52-65$ m on the southern side and 65 m on the northern side of the channel were obtained by calculating the mean u velocity between SFS and SFN. At the southern flank a vertical mean u velocity between $52-65$ m of SFS was calculated and at the northern flank the u velocity of SFN at 65 m was used. The hereby obtained mean u velocity was then multiplied by the area of the triangle. c in equation 4.6 is the distance between the height of 52 m on the southern side and 65 m on the northern side of the channel and b is the distance in 65 m depth between both sides of the channel.

To obtain the real height of a of the triangle under consideration of the latitude, Pythagoras' theorem was used, where the c in equation 4.7 is my a from Heron's formula in 4.6:

$$c = \sqrt{a^2+b^2}. \tag{4.7}$$

a in equation 4.7 is the height of 13 m and b is the lateral distance between the tangent points on the southern side of the channel in 52 and 65 m.

Transports for the layer below ($65-71$ m) were calculated by calculating the area in form of a trapezoid multiplied by the mean velocity of the vertical mean u between 65 and 71 m of SFS and SFN, respectively:

$$A = \frac{a+b}{2} \cdot h, \tag{4.8}$$

where a and b in equation 4.8 are the distance between the northern and southern side of the Stolpe channel in 65 m and 71 m, respectively. The height h is 6 m.

The area below 71 m had to be estimated since no measurements were available for the deepest part of the channel. At first a mean velocity along the latitude was calculated from the two ADCPs' deepest measurements in 71 m depth and also its distance. Then the transport of

[1] http://en.wikipedia.org/wiki/Heron%27s_formula

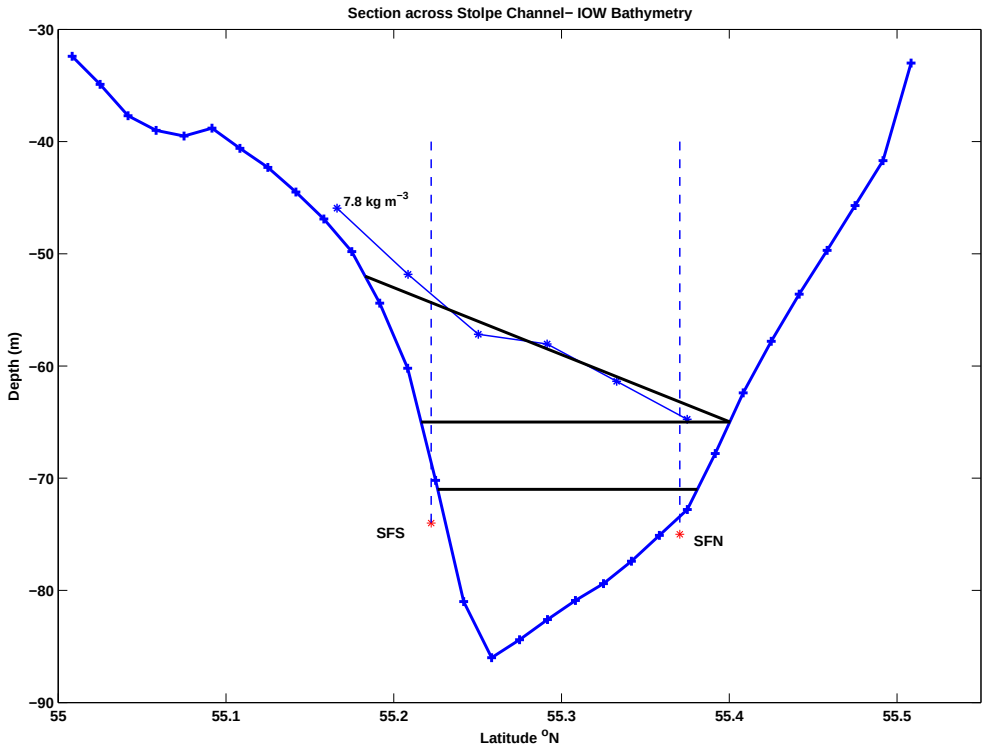

Figure 4.14: Sketch of volume transport calculations through the Stolpe Channel.

the area was calculated by fitting the velocity at each point to its depth within the channel's bathymetry, multiplying it by the distance and then calculating the sum of the result. To get the transport for each time step of the Stolpe Channel below 52 m on the southern flank and 65 m on the northern flank to the bottom all three individual calculated transports had to be added up. The transport calculations were based on hourly current measurements as well as on daily measurements.

Fig. 4.15 shows estimated transports calculated with the above mentioned method from the ADCP current data compared with data extracted from the MOM4 1 nm model at 17.5°E. Both volume transports are based on hourly current values. Modelled transports are calculated by using the 9.5 kg/m^3 isopycnal as a threshold which corresponds to the slope between 52 m on the southern side of the channel and 65 m on the norther side, as opposed to the 7.8 kg/m^3 isopycnal identified in the CTD transects. This discrepancy is due to the fact that the salinity gradient in the model is not as pronounced as in the measurements (see Fig. 4.8 C, D for CTD transects, model transects not shown). Temperatures and salinities in the model are well reproduced by the model, but it has difficulties expressing sharp salinity gradients.

Average eastward transports are of around 5 km^3/day and happen more frequently than westward transports (Fig. 4.15). When transports turn westward, they are in general slightly higher

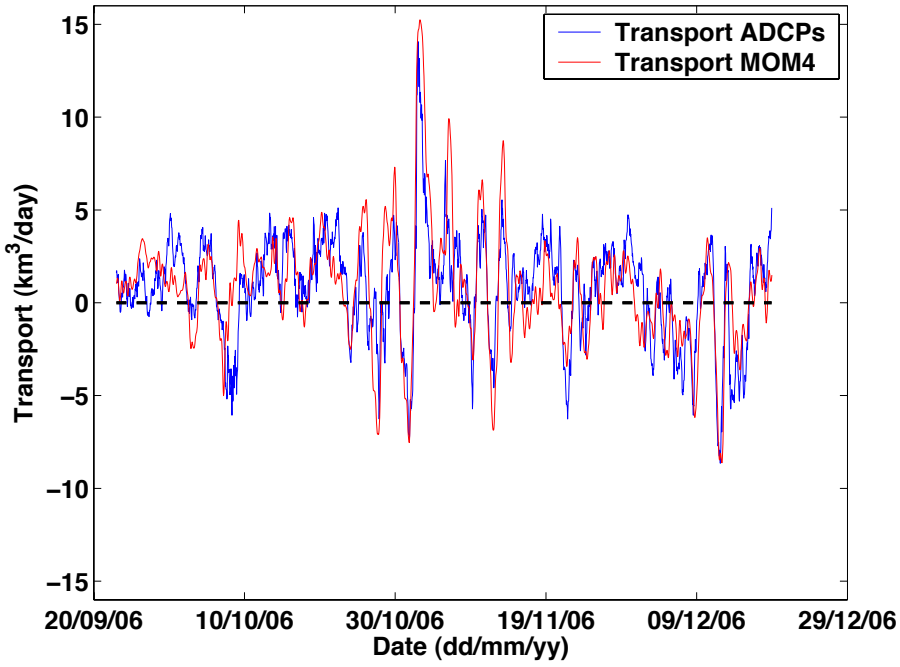

Figure 4.15: Comparison of hourly volume transports through the Stolpe Channel calculated from ADCP measurements with MOM model.

than eastward transports with about 7 km^3/day. During the storm event on 4 November 2006 transports increased suddenly to over 15 km^3/day. Modelled transports reflect the estimated transport values from measured data very well. Largest transports are well and precisely captured by the model, but smaller transport values, especially at the beginning of the recording period, are going in the opposite direction. The model slightly overestimates transports in both eastward and westward directions. This is also visible in Table 4.1 where mean volume transports over the whole recording period are listed. Estimated mean volume transports from measured data are of 0.75 ± 2.32 km^3/d, whereas the model produces mean transports of 0.81 ± 3.15 ^{3}/d. On some occasions the model peaks early compared to the measured values. Cross-correlations between measured and modelled volume transports have a correlation coefficient of 0.79 and no lag.

Table 4.1 not only compares measured and modelled mean volume transport for the 87 days of deployment, but also lists measured transports of $2-4$ days selected for three different occasions. The pulse-like eastward currents led to the question how much water passes the Stolpe Channel in one of these pulse-like events visible in Fig. 4.12, hence for three different occasions the eastward volume transport was calculated from ADCP measurements. The $2-4$ day long strong eastward currents were more prominent and also stronger in ADCP SFN recording ve-

Time Period	Mean Volume Transports ADCPs VoltrpSF$_{ADCP}$ (km^3/d)	Mean Volume Transports Model VoltrpSF$_{9.5}$ (km^3/d)
23/09/2006 - 19/12/2006 (87 days)	0.75 ± 2.32	0.81 ± 3.15
29/09/2006 - 02/10/2006 (75 hours)	1.91 ± 0.93	
14/10/2006 - 17/10/2006 (54 hours)	1.52 ± 1.15	
28/11/2006 - 01/12/2006 (73 hours)	1.78 ± 1.36	

Table 4.1: Comparison of geostrophically balanced mean volume transport across the Stolpe Channel for the whole measuring period between the ADCPs SFN/SFS and modelled transports for densities $\geq$ 9.5 kg/m^3. Examples of mean volume transport of three detailed events.

locities of up to 30 cm/s. Though, eastward velocities in ADCP SFS still measured current velocities of up to 20 cm/s. The results for the three selected events are listed in Table 4.1. The first event lasting from 29 September to 2 October 2006 was the strongest of the three, reaching volume transports of 1.91 ± 0.93 km^3/d. Naturally eastward volume transports of these single events are higher than eastward volume transports over the whole deployment period, where westward currents play a role as well.

The good reproduction by MOM4's volume transports through the Stolpe Channel supports further use of these model simulations for additional investigations regarding the propagation of deep water flow in the Baltic Proper.

4.3.4 Propagation of deep water from the Stolpe Channel to the Eastern Gotland Basin

To estimate how much salt is enclosed in the deep Eastern Gotland basin below 170 m, its total volume has to be calculated first of all. Two different methods will be discussed in the following. The first method uses data from the CTD grid shown in Fig. 1.2 and calculates a volume between $190 - 241.8$ m, developed by Hagen and Feistel (2001). Hagen and Feistel (2001) choose the maximum depth of 241.8 m as a starting point. The area of the horizons above 241.8 m were determined in 26 steps of ΔD = 2 m. The resulting regression of the area is

$$AM(km^2) = 28.16641 * D(m), \tag{4.9}$$

with an interval of $[0 \leq \Delta \leq 52]$ m. The resulting volume-depth regression illustrates a parabolic shape with

$$VM(km^3) = 0.0140832 * D^2(m). \tag{4.10}$$

Fig. 4.16 shows the different volumes calculated of the EGB. The blue stars show measured values from the CTD profiles during the MESODYN project using equation 4.10, were as the

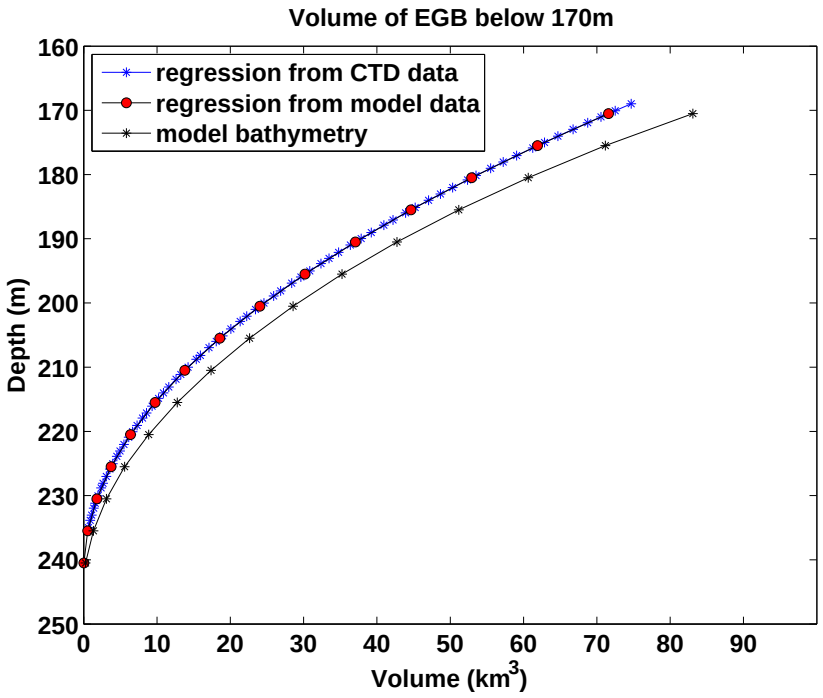

Figure 4.16: Calculated volume of the EGB from CTD data (blue stars) and from model data (red circles). The black line and stars show volume taken from model bathymetry.

red circles are modelled depths from the MOM4 model applied to equation 4.10. The regression calculated by Hagen and Feistel (2001) defines the depth range between 190 and 241.8 m, whereas in this study the regression has now been extrapolated and the volume re-calculated between 170 and 241.8 m. Using the CTD data, equation 4.10 gives a volume of 72.5 km^3 between 170.05 to 241.8 m, the model data results to a slightly smaller volume between $170.5 - 241.8$ m of 71.6 km^3. The second method simply calculates the volume of the deep EGB from the model bathymetry. By retrieving the volume of the deep EGB from the model bathymetry instead of assuming the shape of the basin as parabolic gives a more precise results, since the regression is only an approximation of the real bathymetry. The volume from the model bathymetry between 170.5 and 240.5 m results to a volume of 83.1 km^3. Hence, for further computations the volume obtained from the model bathymetry is used from hereon. With a volume of 83.1 km^3 and an estimated mean volume transport through the Stolpe Channel of 0.75 km^3/d (Table 4.1) it would take around 111 days to fill up the deep EGB below 170 m.

The total salinity in the EGB below 170 m in a volume of 83 km^3 was extracted from the model between 2002 and 2009. Fig. 4.17 (main graph, blue curve) illustrates that the largest influence in the salt content of the deep basin was the deep inflow in 2003, dramatically increasing its salt content in these 7 years of simulation. According to Fig. 4.17 the next bigger and most note-

worthy inflow occurred directly after the end of the measuring campaign in the RAGO project (May 2006 - March 2007). The time period of the inset picture in Fig. 4.17 corresponds exactly to the deployment period of the current meter moorings in the EGB (red curve), highlighted in black is the three months deployment period of the ADCPs in the Stolpe Channel, all part of the RAGO project. The following features can be observed in the inset picture of Fig. 4.17, a strong decrease in salinity between $1-6$ November 2006 followed by a stagnation period with a slight rise in the salt content for the rest of the month. It can be assumed that this is the small inflow observed in the CTD records of the monitoring station BMP271 and inferred from the three temperature sensors of the current meter moorings. Thereafter the general trend is a decrease in salt until end of the measuring period (end of March 2007). The temperature increase recorded by the mid and lower temperature sensor (205 and 220 m) of mooring SE (compare Fig. 4.4) confirms the assumption of a new deep inflow. The red curve in the inset picture shows two more occasions when the salt content remains stable and does not decrease continuously, first the beginning of January 2007 and second during the mid of February 2007.

The increase in salinity during the inflow 2003 amounts to 35,000,000 tons of salt in the EGB and had its maximum at 1.09×10^9 tons salt (1.09 Gt salt) which decreased continuously until the beginning of April 2007. During the deployment period between May 2006 and end of March 2007 the decrease in salt amounted to 5,000,000 tons.

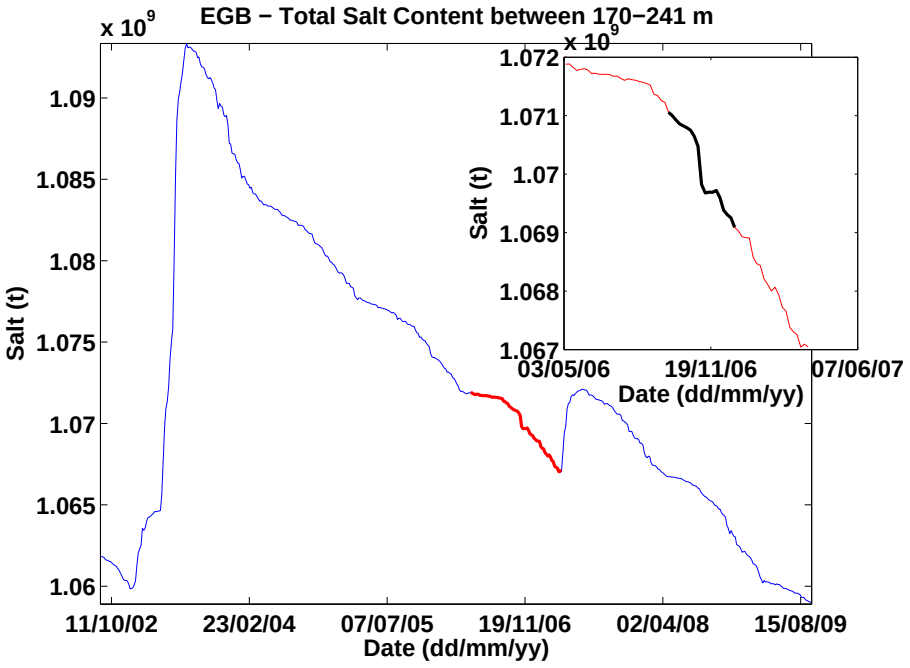

Figure 4.17: Total salt content of the deep EGB greater than 170 m in a volume of 83 km^3.

To answer the question how the salt is transported from the Stolpe Channel into the EGB and which pathways it takes, model simulations with the MOM4 model show the propagation of salt and currents for the temporal average of the ADCPs' deployment period (23 September to 18 December 2006) in Fig. 4.18. Bottom layer salinities and currents split after leaving the Stolpe Channel into two pathways, one part is travelling southeastward into the Gdansk Basin and the other part chooses the deepest pathway towards the Eastern Gotland Basin. This phenomenon was also observed in numerical experiments conducted by Zhurbas et al. (2003) for northerly and easterly winds operating over a period of 10 days and salinities higher than 11 g/kg. Although, in the experiments carried out by Zhurbas et al. (2003) cyclonic eddies formed in the intermediate layer and not at the bottom as seen in Fig. 4.18.

Water masses entering the Gdansk Basin seem to mainly re-circulate in a large eddy before some water masses travel along the 50 m contour to join water masses travelling along the deepest pathway at 55.9°N. Even water masses that travel along the deepest pathway seem to split at 55.5°N and $18.5 - 19$°E into two paths before re-joining with waters from the Gdansk Basin 55.9°N. From there the bottom water then enters the EGB over its eastern flank, arriving first at the SE mooring. The average from model simulations calculated deep circulation in the EGB (visible in Fig. 4.18) confirms the pathway that emerged from the current meter observations. Dense deep water enters the EGB over the eastern flank is then deflected to the right by the Coriolis force and travels round the deep boundary inside the basin in a cyclonic circulation.

Temperature, salinity, density, depth and current data (u and v) were extracted as 5-day means for three selected transects over a period of 7 years (2002 to 2009). The data are expected to provide answers on how much water passes each transect and how much volume and salt is transported through each section on its way to the EGB.

Modelled volume transports (of 5-day mean current values) through all three sections marked in Fig. 4.18 are displayed in Fig. 4.19 with the Stolpe Channel's eastward transport at 17.5°E in black, the Gdansk Basin's southward transport at 55°N in blue and the Hoburg Channel's northward transport at 56°N in red. Only the relevant transport components, important for the transports in the deep Baltic Proper, are investigated in these figures. In Fig. 4.19 A transports between 2002 and 2009 are displayed, whereas Fig. 4.19 B only shows the time period between May 2006 and the end of March 2007. All transports were calculated for salinities greater-than-or-equal 12 g/kg salt, under the assumption that salt less than 12 g/kg salt is not able to travel beyond the Stolpe Channel as deep density currents. This assumption is also supported by the over 87 days time averaged salinity in Fig. 4.18, where the average salinity entering the deep EGB is higher than 12 g/kg salt. The southward volume transport in Fig. 4.19 A reveals

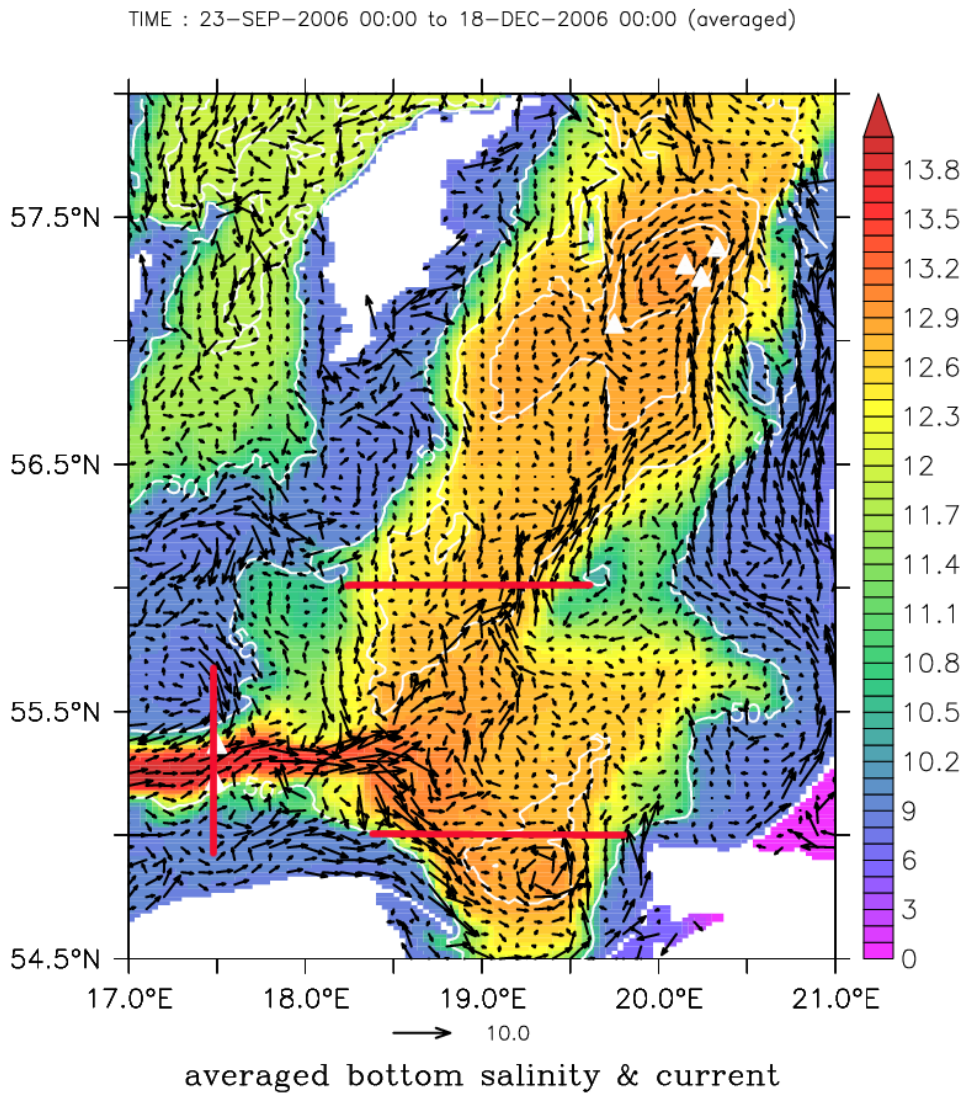

Figure 4.18: Propagation of the deep water in the bottom boundary layer (black arrows) and mean salinity distribution for the Baltic Proper, simulated with MOM4. T, S, depth and currents were extracted as 5-day means for 3 selected transects (red lines). White triangles represent mooring positions.

rhythmic peaks in transports appearing on an annual basis, around autumn/winter each year. The first peak was recognised on 11 October 2002 and the last 6 March 2009; every peak slightly shifts within each year. The corresponding power spectrum (Fig. 5.4 upper right panel in the appendix) reveals 2 peaks, one at about 429 days and the other at about 321 days. These two peaks were apparent in the volume transports of all three transects (Fig. 5.4 all 3 panels in the appendix). By comparing the transports through each of the three sections it becomes obvious that volumes are smallest going through the Stolpe Channel and highest going through

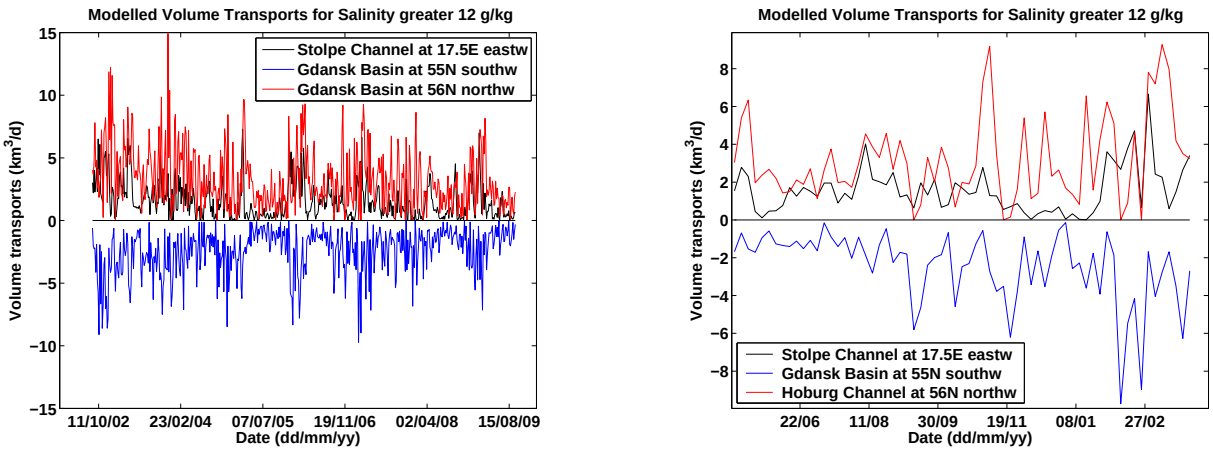

A B

Figure 4.19: Modelled volume transports through three sections in the Baltic Proper, Stolpe Channel at 17.5°E, Gdansk Basin at 55°N and Hoburg Channel at 56°N, positions are marked in Fig. 4.18. A:time period 2002 - 2009, B: time period May 2006 - March 2007. Note, scales between plots slightly differ.

the Hoburg Channel. Peaks of eastward volume transports of 5-day means through the Stolpe Channel in Fig. 4.19 A vary between $4-6$ km^3/d and on two occasions transports rose up to 7 km^3/d in those 7 years. Southward volume transports through the Gdansk Basin vary in peaks between $7-9$ km^3/d. Through the Hoburg channel the northward transports are of around 9.5 km^3/d, except for two occasions where transports increase up to 12 and 15 km^3/d both in December 2002 and 2003, respectively. Fig. 4.19 B shows no seasonal or annual cycle, primarily because the main signals in the power spectrum are of just under a year and somewhat more than a year and the time series was too short to resolve such signals. What is striking is the fact that the storm event at 4 November is only represented by transports through the Hoburg Channel, which expresses transports of over 9 km^3/d that day. The Stolpe Channel shows only a small peak in eastward transports of over 2 km^3/d, but the Gdansk Basin responded with very low southward transports. This will be investigate at a later stage. In general high eastward and northward transports through the Stolpe Channel and Hoburg Channel are responded by the Gdansk Basin with low transports. The Stolpe Channel has maximum eastward transports of 7 km^3/d at the beginning of March, the Gdansk Basin's maximum southward transports of $9-10$ km^3/d are at mid and end of February and the Hoburg Channel has maximum northward volume transports on the 4 November 2006 and at the beginning of March with nearly 10 km^3/d. Salt transports peak at exactly the same time as the volume transports and also reproduce annual cycles. Maximum salinities transported in an eastward direction through the Stolpe Channel are of $0.9-1.0 \times 10^8$ tons/d; on average, peaks are between $0.5-0.8 \times 10^8$ tons/d (see Fig. 4.20 A).

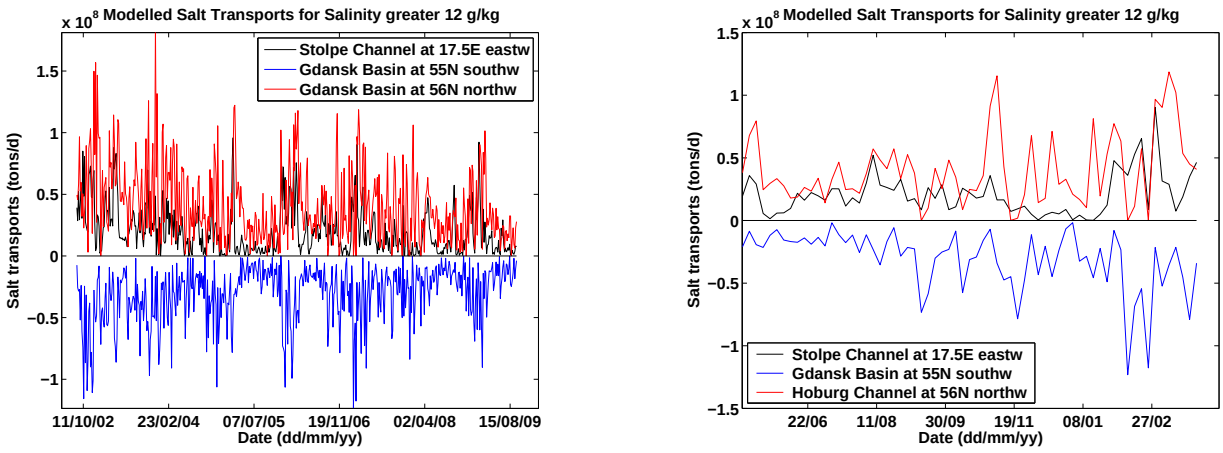

A B

Figure 4.20: Modelled salt transports through three sections in the Baltic proper, Stolpe Channel at 17.5°E, Gdansk Basin at 55°N and Hoburg Channel at 56°N, positions are marked in Fig. 4.18. A:time period 2002 - 2009, B: time period May 2006 - March 2007. Note, scales between plots slightly differ.

Southward salt transports in the Gdansk Basin are larger with maximums of $1.1 - 1.2 \times 10^8$ tons/d at the beginning and end of February, only days before an inflow was registered by the SE mooring's mid and bottom temperature sensors and also by the model results displayed in Fig. 4.17. The peak is shown in detail in Fig. 4.20 B; except from one other occasion where salt transports reached values of 1.1×10^8 tons/d, average peaks were between $0.6 - 1.0 \times 10^8$ tons/d. The Hoburg Channel shows highest northward salinity transports in 2003, when the large inflow occurred. On this occasion a maximum of 1.9×10^8 tons/d was registered. For some reason transports through the other two transects (Stolpe Channel and Gdansk Basin) show an increase in transports in general, but peaks are not as pronounced as in the Hoburg Channel's modelled data. During the RAGO campaign highest eastward salt transports through the Stolpe Channel were registered with 0.9×10^8 tons/d at the end of February, coinciding with second highest southward salt transports through the Gdansk Basin of 1.1×10^8 tons/d. Highest transports through the Gdansk Basin happened a few weeks earlier with 1.1×10^8 tons/d. Northward transports through the Hoburg Channel were highest during the storm event on 4 November 2006 and in the beginning of March 2007 with transport values of 1.2×10^8 tons/d.

It is surprising that volume and salt transports through the Hoburg Channel are highest of all three transports, but it also has to be noted the transports discussed in Fig. 4.19 and in Fig. 4.20 have a salinity of 12 g/kg salt or higher and are either the east (Stolpe Channel), south (Gdansk Basin) and north (Hoburg Channel) components. Mass conservation has not been looked at in

these calculations, solely the transport that is relevant for the salt content in the EGB, when leaving the Stolpe Channel. A closer look at the positions of the three transects in Fig. 4.18 reveals that over the three months average a cyclonic eddy is present in the southern Gdansk Basin, with southward currents at its western boundary and a northward currents along its eastern boundary which wasn't taken into account in this approach. In the Hoburg Channel transect, two separate currents join up and therefore increasing the flow, but also the east end of the transect lies in a re-circulating anti-cyclonic eddy. At its western end another re-circulating eddy is visible. Both eddies feed the northward current at 56°N with additional water and thus increase its transports. Despite the fact that some of the transports through the three transects are rather high it is interesting to know if and how they are correlated with one another and with the salt content of the deep EGB. To be able to cross-correlate the different data sets (modelled and measured volume and salt transports), 5-day means of the hourly and daily data sets were created. To make things easier, short names are introduced for the different data sets and an overview given in the abbreviations: for the Stolpe Channel 5-day mean volume transports both eastward/westward and also solely eastward with salinities greater-than-or-equal 12 g/kg will be called $\mathrm{VoltrpSF}_{12}$ and $\mathrm{VoltrpSF}_{12P}$, respectively. Salt transports will be referred to in the same manner: $\mathrm{SaltrpSF}_{12}$ and $\mathrm{SaltrpSF}_{12P}$. Daily volume transports through the Stolpe Channel of the data set greater than 9.5 kg/m^3 will be called $\mathrm{VoltrpSF}_{9.5}$ for both

Time Series A	Time Series B	Time	Correlation Coefficient	Time Series B lags Time Series A by (Days)
$\mathrm{VoltrpSF}_{12P}$/ $\mathrm{SaltrpSF}_{12P}$	SalEGB_{170}	2002 - 2009	0.9	0
$\mathrm{VoltrpSF}_{9.5P}$	SalEGB_{170}	Sep - Dec 2006	0.95	0
$\mathrm{VoltrpSF}_{ADCP}$	$\mathrm{VoltrpSF}_{9.5}$	Sep - Dec 2006	0.79	0
$\mathrm{VoltrpSF}_{ADCP}$	$\mathrm{VoltrpSF}_{12}$	Sep - Dec 2006	0.79	5
$\mathrm{VoltrpSF}_{ADCP}$	SalEGB_{170}	Sep - Dec 2006	0.66	15
$\mathrm{VoltrpSF}_{ADCP}$	$\mathrm{Voltrp55}_{12N}$	Sep - Dec 2006	0.67	20
$\mathrm{Voltrp55}_{12N}$	SalEGB_{170}	2002 - 2009	0.81	0
$\mathrm{Voltrp55}_{12N}$	$\mathrm{Voltrp56}_{12P}$	2002 - 2009	0.77	15
$\mathrm{Voltrp56}_{12P}$	$\mathrm{Voltrp55}_{12N}$	2002 - 2009	0.65	25
$\mathrm{Voltrp56}_{12P}$	SalEGB_{170}	2002 - 2009	0.79	0
$\mathrm{VoltrpSF}_{ADCP}$	$\mathrm{Voltrp56}_{12P}$	Sep - Dec 2006	0.60	20
$\mathrm{VoltrpSF}_{ADCP}$	$\mathrm{Voltrp56}_{12P}$	Sep - Dec 2006	0.59	15
$\mathrm{VoltrpSF}_{ADCP}$	$\mathrm{Voltrp56}_{12P}$	Sep - Dec 2006	0.56	0

Table 4.2: Cross-correlations of measured and modelled volume and salt transports of Stolpe Channel, Gdansk Basin and Hoburg Channel and salt content EGB.

eastward and westward transports, and $\text{VoltrpSF}_{9.5P}$ for only eastward transports. Estimated daily deep volume transports from ADCP measurements, eastward and westward, will be called VoltrpSF_{ADCP}. The 5-day mean volume and salt transports in the Gdansk Basin, in both northerly and southerly (positive and negative transports), as well as only southerly directions (negative transports), will be called: Voltrp55_{12}, Saltrp55_{12} and Voltrp55_{12N}, Saltrp55_{12N}. The 5-day mean northerly and southerly and solely northerly (positive) volume and salt transports through the Hoburg Channel at 56°N will be called Voltrp56_{12}, Saltrp56_{12} and Voltrp56_{12P}, and Saltrp56_{12P} in the following. The 5-day mean salt content of the deep Eastern Gotland Basin below 170 m will be called SalEGB_{170}. The results of the cross-correlations are compiled in Table 4.2.

The 15 day lag between the Stolpe Channel and the EGB (Table 4.2) implies that by estimating the distance between the two locations (about 350 km), water is transported with a velocity of around 27 cm/s. This is in fact much faster than the average calculated velocities shown in Fig. 4.18. By looking at the correlations altogether (Table 4.2) the following implications on the pathways of the deep water can be made. It seems that water from the Stolpe Channel more often takes the direct pathway, transporting water directly into the EGB (implied from no lag and a correlation coefficient with modelled volume transports of 0.95). Water re-directed through the Gdansk Basin is possibly re-circulating there before being transported through the northern parts of the Gdansk Basin towards the Hoburg Channel. From there it is transported directly into the EGB, implied by the high correlation between the Hoburg Channel and the EGB and the absence of a lag. Although, it is possible that smaller lags are not captured or probably filtered out by the 5-day means, as smaller lags cannot be resolved with this method. The lag between the measured data in the Stolpe Channel and the Hoburg Channel of 20 days needs some explanation, since the lag between measured transports and the salt content of the EGB have only a lag of 15 days, which corresponds with the second peak and same lag between VoltrpSF_{ADCP} and the salt content of the EGB. The 20 day lag could be caused by water masses which leave the Stolpe Channel towards the deepest pathway but are split and take a detour through the western part of the Gdansk Basin first. The third peak of no lag could be the result of internal seiches, which have a period of 2 days (Samuelsson and Stigebrandt, 1996).

Volume and Salt transports (calculated from 5-day means) are the positive volume and salt transports through the Stolpe Channel and Hoburg Channel taken from Fig. 4.21, Fig. 4.22 and Fig. 4.25, the negative is the southerly transport through the Gdansk Basin from Fig. 4.23 and Fig. 4.24 and displayed in Table 4.3. Focusing on the eastward volume transport through the Stolpe Channel first, an amount of 3874 km^3 of water passes through the deep channel in 7

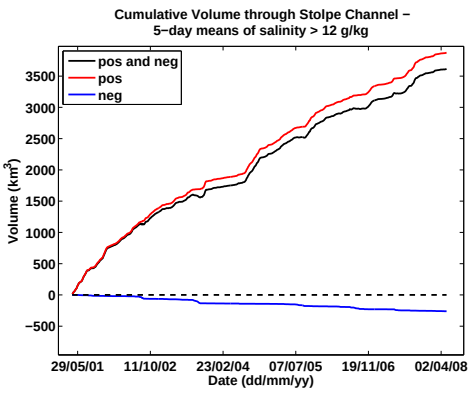

(a) 2002 – 2009

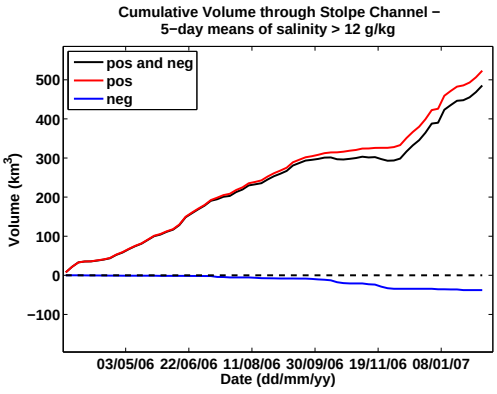

(b) May 2006 – March 2007

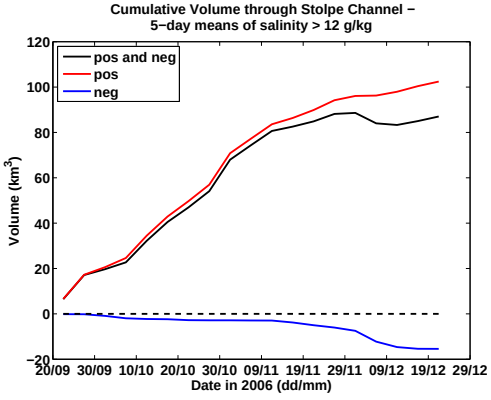

(c) September to December 2006

Figure 4.21: Cumulative positive (eastward, red), negative (westward, blue) and both positive/negative (black) volume (km^3) through Stolpe Channel at 17.5°E for salt $\geq$ 12 g/kg; position is marked in Fig. 4.18. Note, scales between plots differ.

years, carrying 50.19 Gt of salt with it. During the deployment period between May 2006 and March 2007 523.2 km^3 of water were transported with the eastward current carrying 6.88 Gt of salt. In Fig. 4.22 b it becomes obvious that the eastward flow does not increase steadily but has a stagnation phase, visible in form of a plateau, where westward flows dominate. This is visible in Fig. 5.5 b (in the appendix) showing volumes for salinities of less than 12 g/kg salt that during this time a general westward direction prevails (black line). The overall mass balance for the time period May 2006 to March 2007 highlights that westward currents predominate eastward currents, Fig. 5.7 b in the appendix and Table 4.4, transporting more water out of the Stolpe Channel than into the Baltic Proper. For this time period 6.7 Gt of salt are transported through dense bottom currents into the Baltic Proper, Fig. 4.22 b. Even in the short time period of 87 days (September to December 2006, Fig. 4.22 c) 1.4 Gt of salt are transported eastward through the Stolpe Channel. These 1.4 Gt of salt could be seen as a stagnation period for salt transported

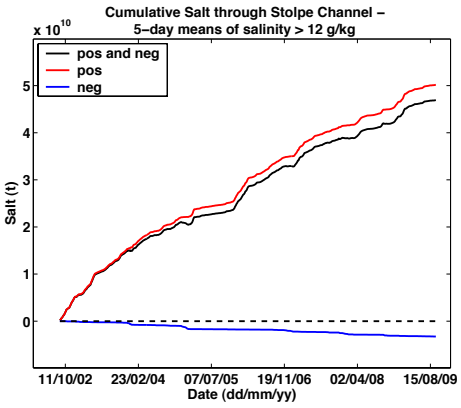

(a) 2002 – 2009

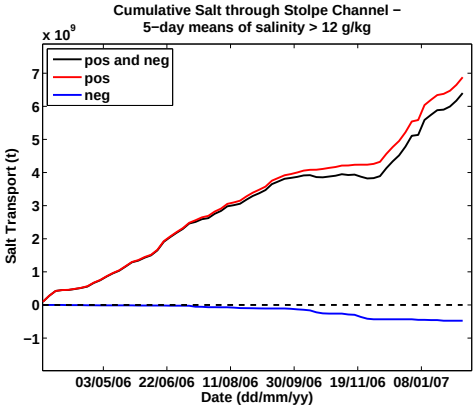

(b) May 2006 – March 2007

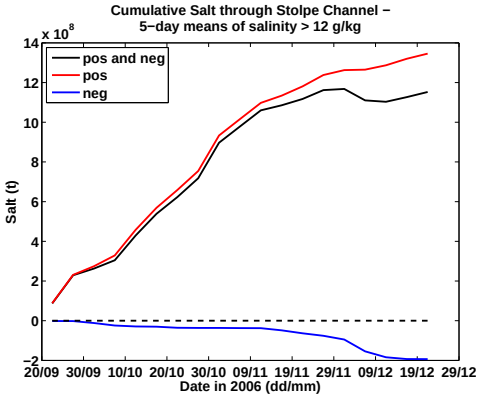

(c) September to December 2006

Figure 4.22: Cumulative positive (eastward, red), negative (westward, blue) and both positive/negative (black) salt load (t) through Stolpe Channel at 17.5°E for salt $\geq$ 12 g/kg. Note, scales between plots differ.

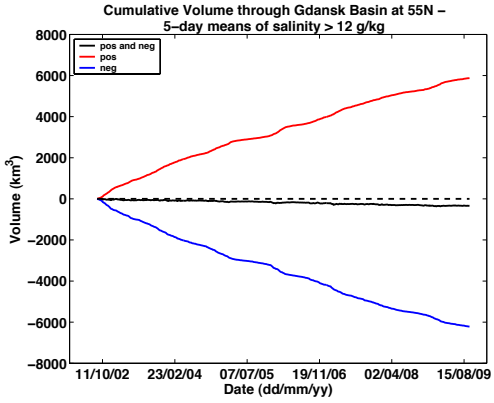

(a) 2002 – 2009

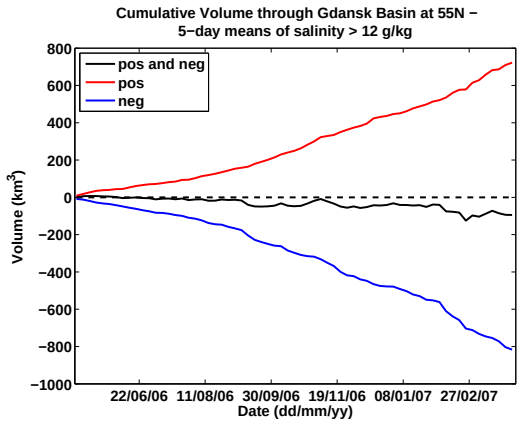

(b) May 2006 – March 2007

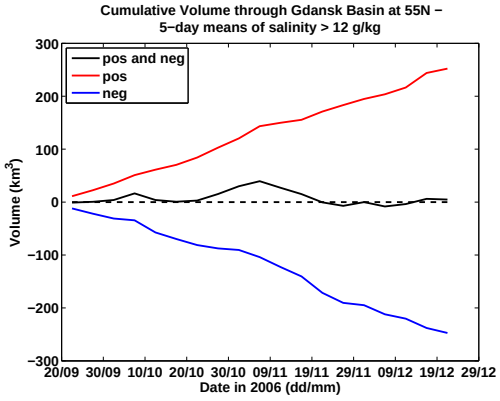

(c) September to December 2006

Figure 4.23: Cumulative positive (eastward, red), negative (westward, blue) and both positive/negative (black) volume (km^3) through Gdansk Basin at 55°N for salt $\geq$ 12 g/kg. Note, scales between plots differ.

eastward, since nearly 4 Gt of salt were transported through the channel until September 2006 and from January and March 2007 another nearly 3 Gt were transported eastward Fig. 4.22 b. By examining the three different time periods of the Stolpe Channel, it can be assumed that for short time periods more salt is transported out of the channel than into the Baltic Proper (Fig. 5.8 b, c). Over the 7 years, however, the inflows of different strength (compare Fig. 4.17) showed a slight domination of salt import into the Baltic Proper over an export. Table 4.4 shows a total of 6.7 Gt of salt are carried through to the Baltic Proper. It is hard to say how much of the water ends up in the Gdansk Basin and passes through the Hoburg Channel, since both transects have a recirculation in their system.

The cumulative volume and salt load of the Gdansk basin's dense bottom water for salt greater-than-or-equal 12 g/kg are mass balanced in itself (Fig. 4.23 a-c). Nearly as much is going into the basin (southward volume/salt) as is going out (northward volume/salt). For the 7 year period

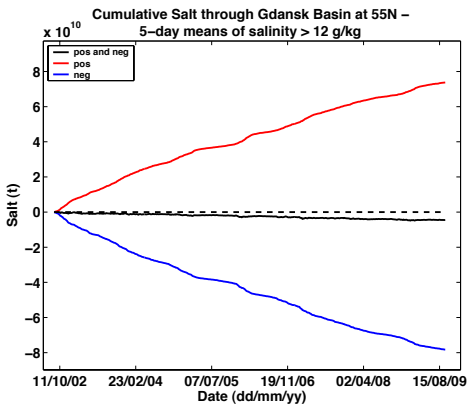

(a) 2002 – 2009

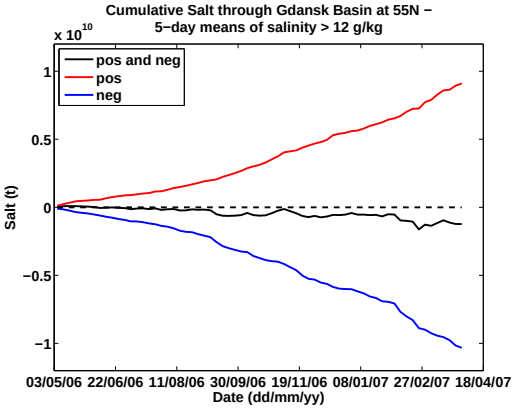

(b) May 2006 – March 2007

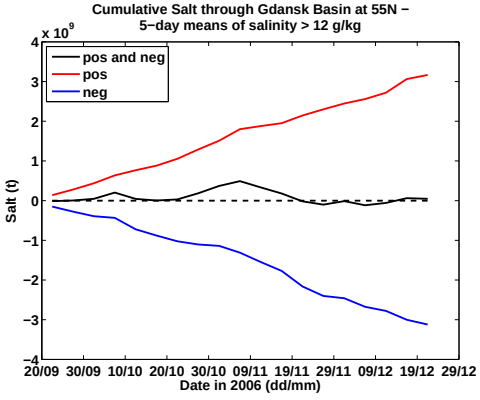

(c) September to December 2006

Figure 4.24: Cumulative positive (eastward, red), negative (westward, blue) and both positive/negative (black) salt load (t) through Gdansk Basin at 55°N for salt $\geq$ 12 g/kg. Note, scales between plots differ.

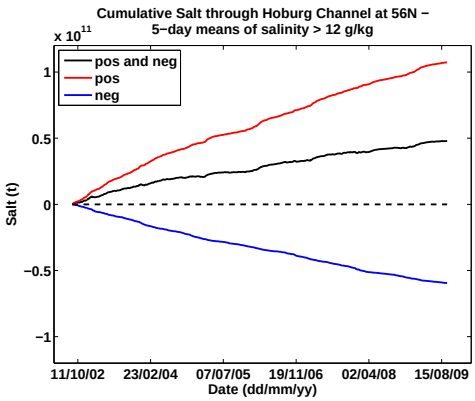

(a) 2002 – 2009

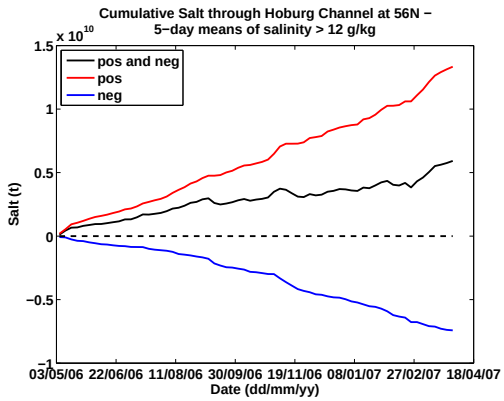

(b) May 2006 – March 2007

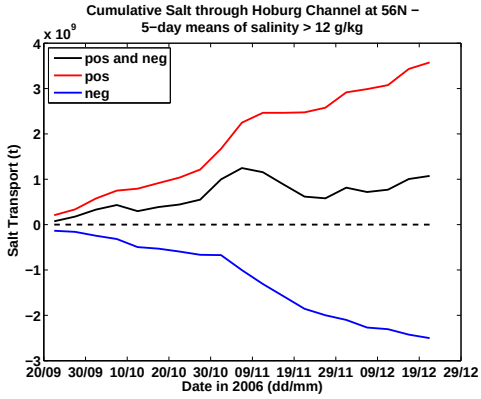

(c) September to December 2006

Figure 4.25: Cumulative positive (eastward, red), negative (westward, blue) and both positive/negative (black) salt load (t) through Hoburg Channel at 56°N for salt $\geq$ 12 g/kg. Note, scales between plots differ.

6212 km^3 enter the basin on its western flank, 5876 km^3 are leaving the basin on its eastern flank and 336 km^3 stay (Fig. 4.23 a). The salt amount balances to 78.24 Gt going in, 73.77 Gt leave the basin and 4.47 Gt stay inside (Fig. 4.24 a). Looking at the shorter time scales, during May 2006 and March 2007 94 km^3 stay in the basin with 817 km^3 transported in and 722 km^3 transported out. The amount of salt that stays in the basin is lower as well, with 1.23 Gt staying in the basin, while 10.33 Gt are transported in and 9.10 Gt transported out (Fig. 4.24 b). Only during the short period between September and December 2006 more salt is transported out than in (0.05 Gt, Fig. 4.24 c).

Cumulative volume and salt of the Hoburg Channel at 56°N are much higher than cumulative volume and salt of the other two transects. Volumes and salt loads displayed in Table 4.3 and Fig. 4.25 let assume a salt load of 47.98 Gt stays in the channel for the 7 years, with 107.41 Gt going northward balanced by only 59.43 travelling southward. Even for the time between May

Time Period	Stolpe Channel at 17.5°E Eastward Transport	Gdansk Basin at 55°N Southward Transport	Hoburg Channel at 56°N Northward Transport
		Total Volume Transport (km^3)	
2002 - 2009	3874	-6212	8578
May 2006 - March 2007	523.20	-816.56	1065
Sep - Dec 2006	102.42	-247.33	285.15
		Total Salt Transport (t)	
2002 - 2009	5.02×10^{10} (50.19 Gt)	-7.82×10^{10} (-78.24 Gt)	1.07×10^{11} (107.44 Gt)
May 2006 - March 2007	6.88×10^{9} (6.88 Gt)	-1.03×10^{10} (-10.33 Gt)	1.33×10^{10} (13.34 Gt)
Sep - Dec 2006	1.35×10^{9} (1.35 Gt)	-3.12×10^{9} (-3.12 Gt)	3.58×10^{9} (3.58 Gt)

Table 4.3: Cumulative modelled volume (km^3) and salt (t) through sections displayed in Fig. 4.18. Positive transport is either eastward (Stolpe Channel) or northward (Hoburg Channel), negative transport is southward (Gdansk Basin).

2006 and March 2007 5.91 Gt remain in the channel. For the three months between only 1.07 Gt remain. The volume displays similar high values (Table 4.3) with remaining 3791 km^3 for the 7 year period, 466 km^3 for the 10 months period during the deployment of the moorings and volume of 84 km^3 for the 3 months period. Looking at the location of the section in Fig. 4.18, the reason for the high loads becomes clear. The eastern end of the transect lies partly inside a large, anti-cyclonic eddy, which makes it difficult to calculate its true northward load. Besides, the transect ends before it reaches the 50 m isobath and therefore makes a proper mass balance calculation impossible. Additionally, according to Meier (2007) only a small fraction of the general surface outflow travels along the east coast of Gotland, when in fact the majority travels along its west coast through the West Gotland basin.

Hourly transport data from the model corresponds well with hourly volume transports estimated from the ADCP measurements, visible in Fig. 4.15. The question now arises what temporal resolution in model simulations is necessary to resolve discovered fluctuations. Hence, the three different model data sets of volume and salt transports were compared for the time period September to December 2006: hourly/daily transports with densities ≥ 9.5 kg/m^3; 5-day transports with salt ≥ 12 g/kg; 5-day mean transports created from the daily values (to allow a direct comparison). Both 5-day data sets, $\mathrm{VoltrpSF}_{9.5}$ and $\mathrm{VoltrpSF}_{12}$, are of similar values, which are compared in Fig. 4.26 and Table 4.5. All 5-day mean volume transports are considerably smaller than hourly as well as daily transports. This has to be taken into consideration in the evaluation of the 5-day mean volumes and salt load through the Stolpe Channel, Gdansk Basin and Hoburg Channel presented before. To estimate how much transports from the different data sets vary from one another, the 5-day means were compared for two different time periods in the analysis

	Time Period	Salt $\geq$ 12 g/kg	Salt $<$ 12 g/kg	Whole Water Column
	2002 - 2009	3614	-5422	-1809
VoltrpSF_{12} (km^3)	May 2006 - March 2007	485	-1388	-902
	Sep - Dec 2006	87	-654	-567
	2002 - 2009	3874	18,516	22,391
VoltrpSF_{12P} (km^3)	May 2006 - March 2007	523	2096	26,189
	Sep - Dec 2006	102	558	660
	2002 - 2009	-260	-23,939	-24,199
VoltrpSF_{12N} (km^3)	May 2006 - March 2007	-38	-3484	-3521
	Sep - Dec 2006	-15	-1212	-1226
	2002 - 2009	46.9	-40.2	6.7
SaltrpSF_{12} (Gt)	May 2006 - March 2007	6.4	-11.7	-5.3
	Sep - Dec 2006	1.2	-5.9	-4.8
	2002 - 2009	50.2	176.2	226.4
SaltrpSF_{12P} (Gt)	May 2006 - March 2007	6.9	19.8	26.7
	Sep - Dec 2006	1.4	5.0	6.3
	2002 - 2009	-3.3	-216.5	-219.7
SaltrpSF_{12N} (Gt)	May 2006 - March 2007	-0.5	-31.5	-32.0
	Sep - Dec 2006	-0.2	-10.9	-11.1

Table 4.4: Mass balance of modelled cumulative volume (km^3) and salt (Gt) with salt $\geq$ 12 g/kg, salt $<$ 12 g/kg and whole water water column of Stolpe Channel.

that follows and compiled in Table 4.1: over the 87 day deployment period of the ADCPs, as well as for a period of one year (June 2006 to June 2007). Hourly volume transports were regarded as 100% and then daily and 5-day mean transports were compared in relation to those hourly values. Eastward/ westward daily and 5-day transport means of $\text{VoltrpSF}_{9.5}$ and VoltrpSF_{12} over the 87 day period from September to December 2006 are all very similar. Hourly and daily volume transports ($\text{VoltrpSF}_{9.5}$) are both 100%. In contrast, 5-day transports of $\text{VoltrpSF}_{9.5}$ are of 99.8% and 5-day transports of VoltrpSF_{12} are 112.8% of the hourly ($\text{VoltrpSF}_{9.5}$) volume transports. This high value of 112.8% is due to the very small westward transports in the VoltrpSF_{12} data set. 5-day means of $\text{VoltrpSF}_{9.5}$ produce slightly higher westward transports. Significant differences become obvious when eastward and westward transports are examined separately for the 87 day period. Table 4.5 highlights that daily eastward volume transports ($\text{VoltrpSF}_{9.5P}$) are 89% of hourly values, eastward 5-day means ($\text{VoltrpSF}_{9.5P}$) are still 86.9%, but 5-day means of VoltrpSF_{12P} are only 60.5%. These large differences between the two 5-day means arise as a consequence of the way they are calculated. 5-day means of eastward (and westward) volume transports of $\text{VoltrpSF}_{9.5}$ are created from daily eastward (and westward) volume transports, whereas in contrast VoltrpSF_{12} transport values are already extracted as 5-day means from the

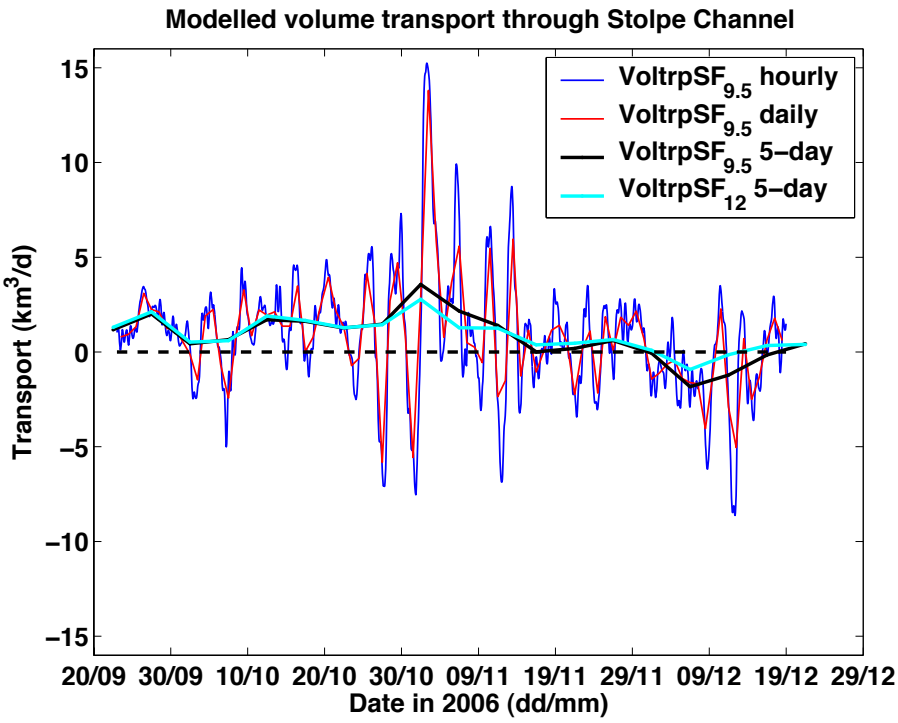

Figure 4.26: Deep volume transports across the Stolpe Channel from model data. Hourly (blue) and daily transport values (red) were derived from densities higher 9.5 kg/m^3, 5-day transports (cyan) from salinities higher 12g/kg.

model. Negative (westward) daily transports (VoltrpSF$_{9.5N}$) are 80% of the hourly values. The 5-day westward transports of VoltrpSF$_{9.5N}$ are 24% smaller than hourly values between September and December 2006. Comparing the 5-day values of eastward transports (VoltrpSF$_{9.5P}$) and westward transports (VoltrpSF$_{9.5N}$) separately, in Table 4.5, higher volume transports are noted for 5-day transports derived from the hourly/daily data set. The discrepancy in the two 5-day data sets results from the different way these values were obtained. Eastward (and also westward) 5-day means were derived from the daily eastward volume transports and from daily the westward volume transports. However eastward and also westward transports from VoltrpSF$_{12P}$ and VoltrpSF$_{12N}$, were already extracted from the model as 5-day means and then sorted in positive (eastward) and negative (westward) transports. Had eastward (and also westward) 5-day averaged VoltrpSF$_{9.5}$ transports been generated from the eastward/westward currents presented in Fig. 4.26 as the black line, 5-day volume transports VoltrpSF$_{9.5P}$ and VoltrpSF$_{9.5N}$ would have been of similar magnitude as the original 5-day VoltrpSF$_{12}$ data set (the light blue line).

Fig. 4.26 shows westward transports of VoltrpSF$_{12N}$ on one occasion only. This is reflected in the westward volume transports of VoltrpSF$_{12N}$, which are of only 16.7% and therefore 83.3%

Direction Transport	Time Period	Hourly $VoltrpSF_{9.5}$ (km^3/d)	%	Daily $VoltrpSF_{9.5}$ (km^3/d)	%	5-Day $VoltrpSF_{9.5}$ (km^3/d)	%	5-Day $VoltrpSF_{12}$ (km^3/d)	%
Eastw./Westw.	Sep	0.81	100	0.81	100	0.81	99.8	0.92	112.8
Eastward	-	1.78	100	1.59	89.1	1.55	86.9	1.08	60.5
Westward	Dec 2006	-0.97	100	-0.78	80.0	-0.74	76.1	-0.16	16.7
Eastw./Westw.	June 2006	1.54	100	1.54	98.2	1.52	97.2	1.51	96.8
Eastward	-	2.18	100	2.04	93.6	2.03	93.1	1.59	73.1
Westward	June 2007	-0.64	100	-0.50	78.3	-0.51	79.2	-0.11	17.0

Table 4.5: Hourly, daily, 5-day mean Volume Transports through the Stolpe Channel and their percentage in relation to hourly values. Hourly values considered as 100%.

smaller than hourly transports, compare Table 4.5.

This analysis reveals that 5-day values extracted from the model are insufficient to represent realistic magnitudes of volume transports of the Stolpe Channel and also importantly, the 5-day mean data sets are not able to resolve fluctuations frequently found in the range of $2-4$ days. This explains why, for example, the high transport values in the Stolpe Channel on the 4 November 2006 are not visible in Fig. 4.19 nor in Fig. 4.26. The 5-day mean has its peaks before and therefore is not able to capture the strong storm event (compare Fig. 4.26).

Summing up, 5-day means underestimate transport volumes and are not able to precisely reproduce observed fluctuations that are on a time scale of $2-4$ days. But how are these observed fluctuations generated? In the following the role of local wind fields will be analysed.

4.3.5 Current fluctuations within the Stolpe Channel - steering mechanism

Internal and external forcing mechanisms in the Baltic Proper i.e. the EGB, were investigated by Samuelsson and Stigebrandt (1996), using sea level gauges (SL) and a sea level model. They classified fluctuations in the sea level with periods between a few days and several years into either internally or externally forced motions. Varying sea level in the Skagerrak/ Kattegat region and freshwater supply from the North Sea were classified by Samuelsson and Stigebrandt (1996) as external forcing and resulted for 50 - 80% of the total sea level variances in the Baltic Proper. Associated periods longer than one month are externally forced, because shorter periods are choked by the narrow straits of the Kattegat (Stigebrandt, 1980). Such long externally forced oscillations are similar to open basin oscillations with increasing amplitudes from the node in the mouth to the inner part (a quarter-wave-length oscillator).

In contrast varying air pressure, wind and density in the Baltic Sea are characterised as internal

forcing. Seiches for example have periods of two days and/ or shorter and thus may contribute to the daily averages in sea level variations. Hence, Samuelsson and Stigebrandt (1996) discovered that most of the variance for short periods originates from internal forcing but may induce some variance of longer periods. In other words, periods of shorter than 1 month in the sea level are due to internal forcing. Furthermore Samuelsson and Stigebrandt (1996) detected the Baltic Sea oscillates like a closed basin for short periods. From a kinematical point of view these oscillations reflect the first natural seiche mode, with a maximal variability at the extreme ends in the north and south and minimum in the Baltic Proper (a half-wave-length oscillator). Among other things, this is the reason to use records of the Swedish coastal station Landsort to describe changes in the filling level of the Baltic Proper. For longer periods the internal forced oscillations are kinematically similar to an open bay with increasing amplitudes from the mouth and inwards. Samuelsson and Stigebrandt (1996) explain the shift in kinematics of internally forced oscillation with the limited transport capacity of the straits in the mouth for "high frequency" motion.

Turning back to the changes in deep currents of the Stolpe Channel, significant peaks in periods found in the along-slope and across-slope current components of ADCPs SFN, SFS (Fig. 5.10), as well as in the current meter moorings SE and NE deployed in the EGB (Fig. 5.11, Fig. 5.12 in the appendix) are all shorter than one month. An exception is mooring SW (Fig. 5.13 in the appendix) with a peak around 40 days in the across-slope components. Hence, these time series of deep currents point to the conclusion that internal forcing could be the main steering mechanism and therefore investigations, especially in the Stolpe Channel, are focused on internal forcing, i.e. wind and density changes.

Accordingly daily eastward currents of ADCPs SFN and SFS (Fig. 4.12) were observed to be pulse-like, with each pulse-like event lasting for about 2 - 4 days, as already discussed in chapter 4.3.3. Here, however, the role of changes in the regional wind conditions will be analysed in more detail to understand the response of deep current fluctuations above topographic slopes of the eastern Stolpe Channel. Hypothetically, it is expected that such deep currents follow roughly bathymetric contours due to the conservation of their potential vorticity.

Hence, to obtain the along-slope (Fig. 4.27 B, C) and across-slope components of the currents, u and v were rotated anti-clockwise by 28° to follow the 75 m isobath. These current components were then compared with the regional wind velocity along the main axis of the Baltic Proper, denoted <U>38 (line between red dots in Fig. 4.28). <U>38 results from averaging the records of the meteorological stations Arkona Buoy in the Arkona Basin (AB) and Hoburg (HB), with positions shown in Fig. 4.28. Both wind series were rotated by 180° to match the currents, i.e

now a positive wind is travelling in an eastward direction and a negative in a westward direction. Finally the resulting averaged wind components were rotated anticlockwise by 38° to obtain the forcing parallel to the main axis of the Baltic Proper.

The wind's effect on well mixed and also stratified elongated basins was extensively studied by Csanady (1973), Bennett (1974), Krauss (1979), Krauss and Brügge (1991), Fennel (1986) and Winant (2004) for comparable basins like the Great Lakes as well as coastal upwelling regions. Their main findings provide the base for the following discussion on obtained results from the Stolpe Channel: The surface layer responds with an Ekman transport to the right (perpendicular) to the wind, which also leads to a sea level rise on the right hand side of the channel (in wind direction) and a fall on the left hand side. At the same time downwelling

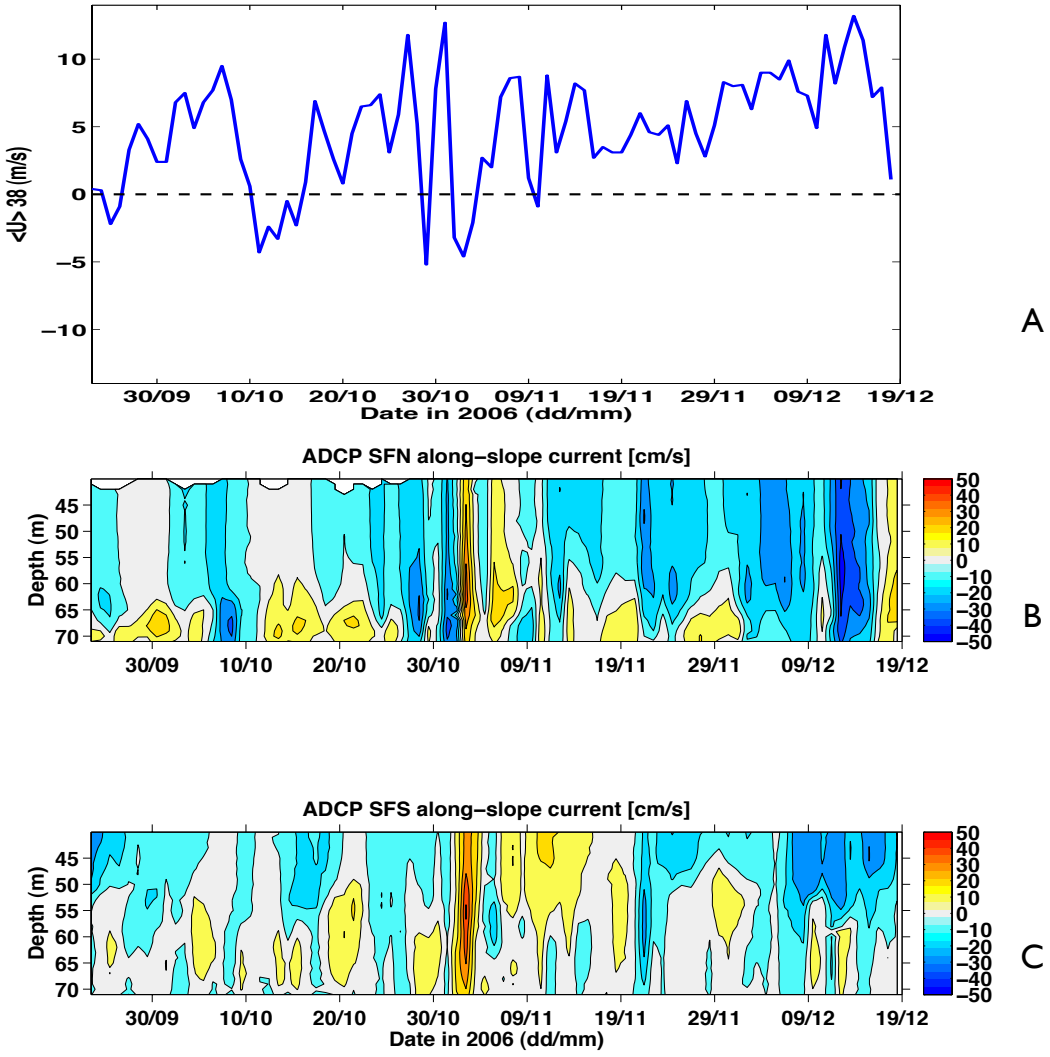

Figure 4.27: A: Daily wind u rotated by 38° and averaged between Arkona and Hoburg. Daily along-slope current velocities for SFN (Fig. 4.27 B) and SFS (Fig. 4.27 C). Positive values in A, B and C depict eastward directions, negative values westward directions.

occurs on the right hand side, which is compensated by upwelling on the left hand side. Coastal jets are established in wind direction on both sides of the channel to be compensated by a return flow in the central and deep areas of the basin. Comparable current situations could be observed in the Stolpe Channel. The eastward deep current core measured by SFN was detected in depths between 65 - 71 m, (Fig. 4.27 B), while at ADCP SFS it were recorded between 52 - 68 m (Fig. 4.27 C). The eastward currents at SFN lagged <U>38 by one day, whereas at SFS they responded immediately and went simultaneously with the regional wind <U>38. But on both sides of the channel eastward currents always lasted for 2 - 4 days, acting pulse-like. Every time the regional wind turned westward, expressed as a negative peak in Fig. 4.27 A, the along-slope components of SFN (Fig. 4.27 B) recorded enhanced eastward bottom currents. On the 25 September, 11 - 15 October, 29 October, 1 - 3 November and 10 November 2006 westward winds were observed and subsequently strong eastward currents were recorded between 27 September and 3 October, 12 - 18 October, 2 - 3 November and 6 - 8 November 2006, Fig. 4.27 B. Associated amplitudes were somewhat stronger in the north than in the south, whereas their overall velocity was of the same magnitude. However, the eastward deep current occupied a thicker deep layer in the south than in the north. The rapid changes in the regional wind from 27 to 31 October, alternating from east to west to east were not reflected by the deep currents of SFN. Instead SFN showed two strong cores of westward currents on 29 and on 31 October 2006. Only the for 3 days lasting strong westward wind at the beginning of November was responded to immediately by strong eastward currents through the whole water column. From around 10 November until the end of the current series solely eastward winds were measured, steadily increasing from 19 November until 15 December 2006. During this time two events of eastward bottom currents were recorded, the first between 18 - 20 November and the second between 26 November and 1 December 2006. The rest of the recording time was mainly characterised by westward currents. Even though the general trend was a continuous increase of <U>38, regular drops in the wind speed occurred. These weakened winds coincided with eastward currents, for example around the 19 and 29 November and 11 December 2006. This could lead to the assumption that prolonged weak eastward winds prioritise density driven boundary currents.

Along-slope currents of SFS in Fig. 4.27 C draw a different pictured than the currents in SFN. Eastward bottom currents in SFS are much more influenced by the sea level gradients acting on the basin scale (compare Fig. 4.30 A) and appear higher up in the water column (52 - 68 m). Thus, the deep along-slope currents at SFS display different characteristics in time and magnitude to along-slope currents at SFN. The only event that affected both measuring sides in the same manner was accompanied by strong westward winds during the beginning of November.

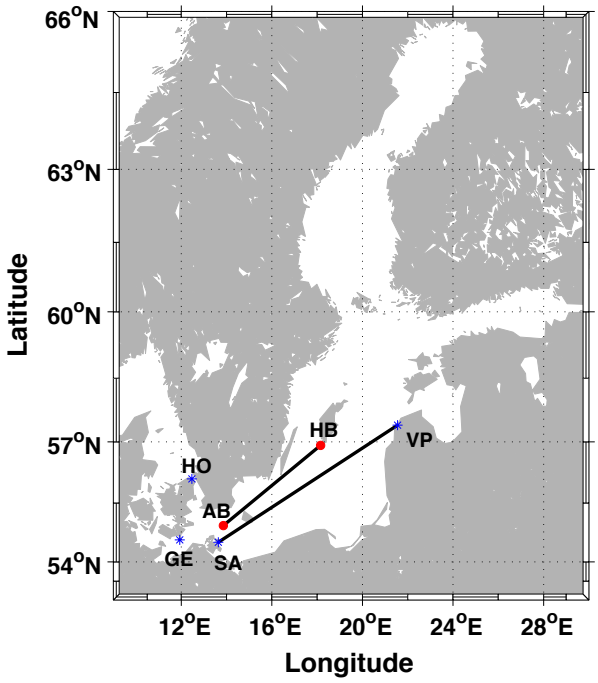

Figure 4.28: Baltic Sea map with positions of SL gauges (blue stars) Ventspils (VP), Sassnitz (SA) and their SL difference (black line) and gauges Hornbaek (HO), Gedser (GE); meteorological stations (red dots) Hoburg (HB) and Arkona buoy in the Arkona basin (AB). Line between AB and HB depicts average wind <U>38.

Its nature was highly barotropic, since the strong eastward currents occupied the whole water column between 42 and 71 m. On the southern side of the Stolpe Channel lower velocity magnitudes than on the northern side prevail.

The afore discussed theory of continuous winds on elongated basins also applies on the basin scale when westward regional winds (<U>38) establish higher sea level anomalies in the southwest than in the northeast of the Baltic Sea. The enlarged hydrostatic pressure in the southwest releases deep down-gradient currents towards the northeast to affect the intensity of such eastward overflow events at the eastern sill of the Stolpe Channel. Associated intrusions of salty and often well oxygenated deep water into the Baltic Proper modifies, via upward entrainment, the stratification conditions. Consequently, the thickness of such eastward currents recorded at SFN (65 - 71 m) coincides with the deep layer observed in Fig. 4.7 at BMP222 for the profiles conducted in January, May and November 2006. Throughout the summer a thermocline builds up with a warm surface layer measured at BMP222 in July 2006 and at the end of September 2006 (Fig. 4.8), whilst the prevailing 2-layer system is replaced by a 3-layer system. Once the air finally cools the surface layer and destroys the warm thermocline, some time between September and November, the 2-layer system is reinstalled. The hydrographic profiles in Fig. 4.8 provide

a good example of the three-layer case comprising of low temperatures from winter convection and high oxygen concentrations below the thermocline in 30 - 60 m. The deep layer establishes a strong meridional slope, reaching into shallower depths on the southern side of the channel than on the northern side. According to Krauss and Brügge (1991), Paka (1996) and Paka et al. (1998) an Ekman transport occurs perpendicular to the wind and produces a sea level rise to the right of the wind in wind direction, i.e. the southern slope of the channel, whereas on the northern side the sea level is slightly lower. Paka et al. (1998) concluded that the fanning out of the deep isopycnals on the southern side and the compressed isopycnals on the northern side is caused by this surface Ekman transport in combinations with a reversed Ekman transport induced by bottom friction. Remarkably, the deep salinity/density gradient in Fig. 4.8 C, D coincides with the depth of eastward travelling bottom currents observed in SFN and SFS. Regarding the position of SFN within the Channel, Fig. 4.8 illustrates densely compressed isohalines/ isopycnals between 65 - 70 m, whereas on the southern side at SFS the fanned out isohalines/ isopycnals exist in depths of around 52 - 60 m. Unfortunately the very bottom layer of each CTD cast is lost due to the nature of measuring techniques and therefore is not captured in the transect. Comparing the meridional slope of the isohalines/isopycnals of Fig. 4.8 C and Fig. 4.8 D with the positions of the two ADCPs and assuming a geostrophic adjustment, it becomes apparent why eastward currents appear at the bottom of the measurements in SFN, but higher up in the water column in SFS. Vertically compressed isohalines/ isopycnals explain the increased intensity of deep eastward currents on the northern slide compared to those on the southern slide, compare Fig. 4.9.

On the basin scale a continuous blowing wind, mainly towards east, moves water masses into the same direction and creates a positive sea level difference in the Baltic Proper. Turns the wind towards west (<U>38<0), a negative sea level difference in the Baltic Proper is created, i.e. the seal level in the southwest Baltic is higher than in the Baltic Proper. The difference of the filling level was calculated between Ventspils (VP) and Sassnitz (SA, SL Δ(VP-SA)) and their positions marked in Fig. 4.28. To what extent the regional wind influences the sea level and also the deep currents will be investigated in the following.

For a direct comparison between the regional wind <U>38 and the sea level difference between Ventspils and Sassnitz (SL Δ(VP-SA)) both time series have to be standardised. The standardisation is achieved by subtracting the mean value of each parameter over the period examined and dividing by the standard deviation ($z = (Y - Y_{mean})/Y_{std}$). Fig. 4.29 A shows how well the sea level reacts to <U>38. Both standardise time series act most of the time simultaneously, which is also expressed by a high correlation coefficient R=0.89, no lag in the cross-correlation and a

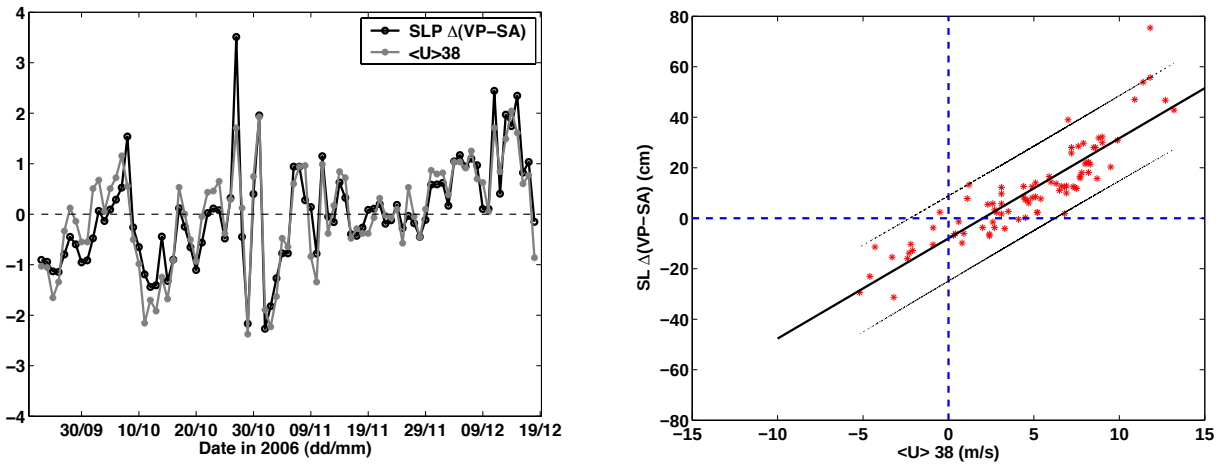

A B

Figure 4.29: A: Standardised time series of <U>38 (grey) and SL Δ(Ventspils-Sassnitz) (black). B: Regression wind <U>38 (Arkona-Hoburg) with SL Δ(Ventspils-Sassnitz). The two fine lines correspond to the 95% confidence interval of the regression line (thick line).

coefficient of determination of R^2=80.1%. Hence it can be affirmed that the wind immediately steers the sea level.

The regression in Fig. 4.29 B (after Hagen and Seifert (2009)) between the wind <U>38 vs. sea level difference Ventspils-Sassnitz (SL Δ(VP-SA)) reveals that winds of higher than 2.5 m/s create a positive sea level difference in the Baltic Proper, i.e. Ventspils. Regional winds of lower magnitude create a positive sea level in the southwest Baltic, i.e. Sassnitz. If the wind is the major factor for steering the sea level, the question is how feasible is it to deduce a dependency between the sea level difference and the deep currents in the Stolpe Channel? Looking at the ADCPs individually on both sides of the channel, their correlations with <U>38 as well as SL Δ(VP-SA) reveals an interesting picture. Here, in (Fig. 4.30 A) the correlation coefficients of <U>38 with u SFN and with u SFS between 43 - 71 m show how the correlation between the currents and the regional wind changed with every depth layer. The correlation was repeated for SL Δ(VP-SA) with u SFN and u SFS to illustrate the changing connection between the currents and the sea level with depth. All correlations were calculated in 1 m steps. It becomes apparent that the regional wind had a greater influence on SFN's east velocity component than the sea level down to a depth of 64 m, with the negative correlation being highest between 43 - 50 m. The influence of the sea level increased from 64 m and gained priority down to 70 m. Comparatively, at SFS the influences of the regional wind and the sea level between 43 and 58 m were rather small; neither had a significant dominant effect on the currents. Although, the correlation of both the wind and the sea level with the u-component of SFS increased

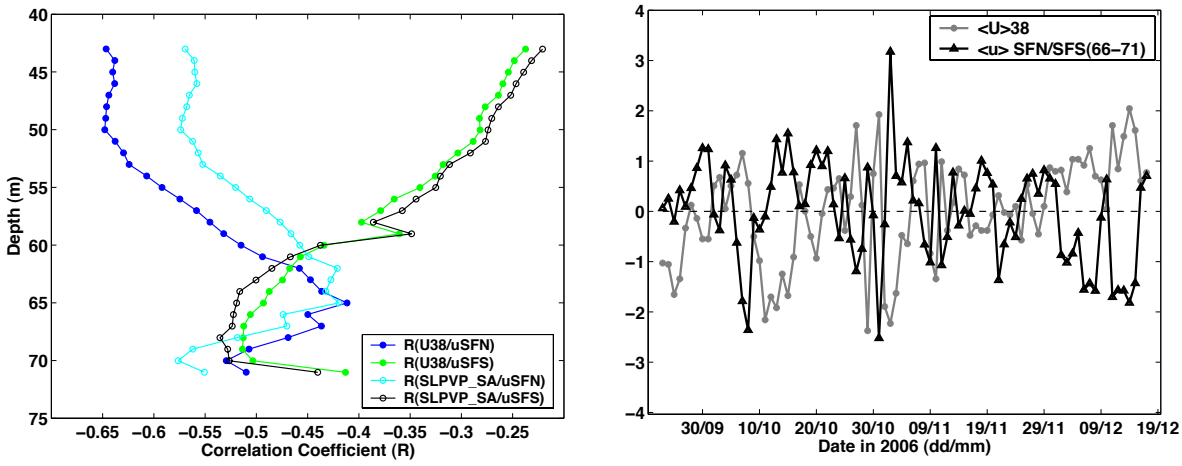

A B

Figure 4.30: A: Correlation coefficients of <U>38 with u SFN (blue)/ u SFS (green) and SL Δ(Ventspils-Sassnitz) with u SFN (cyan)/ u SFS (black) in 1 m steps between 43-71 m. B: Standardised time series of <U>38 (grey) and depth averaged mean current of SFN and SFS (66-71 m, black).

continuously with depth, apart from a sharp jump at 59 m. This jump coincides with the sharp salinity/ density gradient in Fig. 4.8. From 62 m down to 70 m the influence of the sea level increased slightly in contrast to the regional wind. It can be concluded the influence of the wind in the upper layer is predominant at the northern side of the channel, whereas on the southern side the Ekman transport induced by the Coriolis force is the prevailing influence. At 71 m a drop in the correlation is visible on both sides of the channel, implying that the bottom boundary layer reached up to this depth and therefore has a thickness of about 4 m. This thick bottom boundary layer could support Paka et al. (1998) theory of a bottom friction induced Ekman transport. From 59 m down to 70 m the negative correlation of the u-component SFS with both the wind and the sea level continuously increased. On the northern side of the channel the high negative correlation between the wind and the eastward current as well as with the sea level first decreased and only increased again below the jump in 65 m. This jump also coincides with the salinity/ density gradient in Fig. 4.8. Due to the strong negative correlation between the sea level and the two ADCPs in depths greater than 66 m, the mean between the vertical averaged u-velocities (66 - 71 m) of SFN and SFS was created to get an overall deep boundary current. This detrended deep zonal current, now called <u>SFN/SFS(66-71), is cross-correlated with the regional wind by R=-0.63 and has no lag. How well the wind and the deep zonal current are counteracting is displayed in the standardised series of <U>38 and <u>SFN/SFS(66-71) in Fig. 4.30 B. On one occasion the deep current went accordingly with the wind around 27 - 29

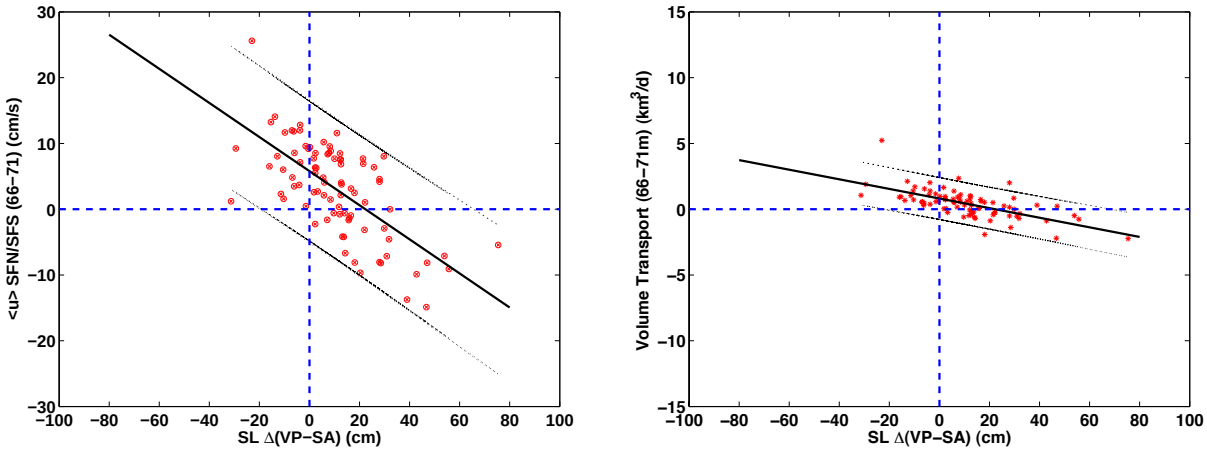

A B

Figure 4.31: Regression SL Δ (Ventspils-Sassnitz) with measured depth averaged zonal velocity from ADCPs (A). SL Δ (Ventspils-Sassnitz) with volume transport (66 − 71 m) (VoltrpSF$_{ADCP66-71}$) Stolpe Channel (B). The two fine lines correspond to the 95% confidence interval of the regression line (thick line).

November, but in general winds and currents counteracted.

The regression between SL Δ(VP-SA) and the vertical averaged eastward velocity between 66 and 71 m (<u> SFN/SFS, 66-71)) in Fig. 4.31 (after Hagen and Seifert (2009)) delivers a correlation coefficient of R=-0.68 and a coefficient of determination of R^2=45.8%. The negative correlation implies that a positive SL Δ(VP-SA), i.e. higher water levels in the Baltic Proper than in the southwest Baltic, caused a negative (westward) flow of deep currents and a negative SL Δ(VP-SA) caused eastward flowing deep currents, compare Fig. 4.31. Negative SL Δ(VP-SA) with maximum sea level differences of 30 cm, i.e. higher water levels in the southwest Baltic than in the Baltic Proper, only triggered a positive deep current. Whereas on the other hand positive SL Δ(VP-SA) with a higher sea level in the Baltic Proper rose to 60 cm and in one case even to 80 cm difference. Positive SL Δ(VP-SA) caused not only negative (westward) deep currents, but also positive (eastward) currents. Although, these positive currents were only caused by positive sea level differences of 30 cm at most and could be the reason why the correlation does not rise above R=-0.68. The correlation between SL Δ(VP-SA) and the estimated volume transport between 66 - 71 m (Fig. 4.31B) as well as SL Δ(VP-SA) vs. the modelled volume transport VoltrpSF$_{9.5}$ (Fig. 4.32A) are slightly less correlated, with a correlation coefficient of R=-0.65 and R^2=42.7% and R=-0.64 and R^2=41.1%, respectively. Interestingly the correlation between the wind <U>38 and the modelled volume transport VoltrpSF$_{9.5}$ in Fig. 4.32B are just marginally better (R=-0.65 and R^2=42.3%) than the correlation of SL Δ(VP-SA) with VoltrpSF$_{9.5}$. Although the correlations between SL Δ(VP-SA) and the estimated volume trans-

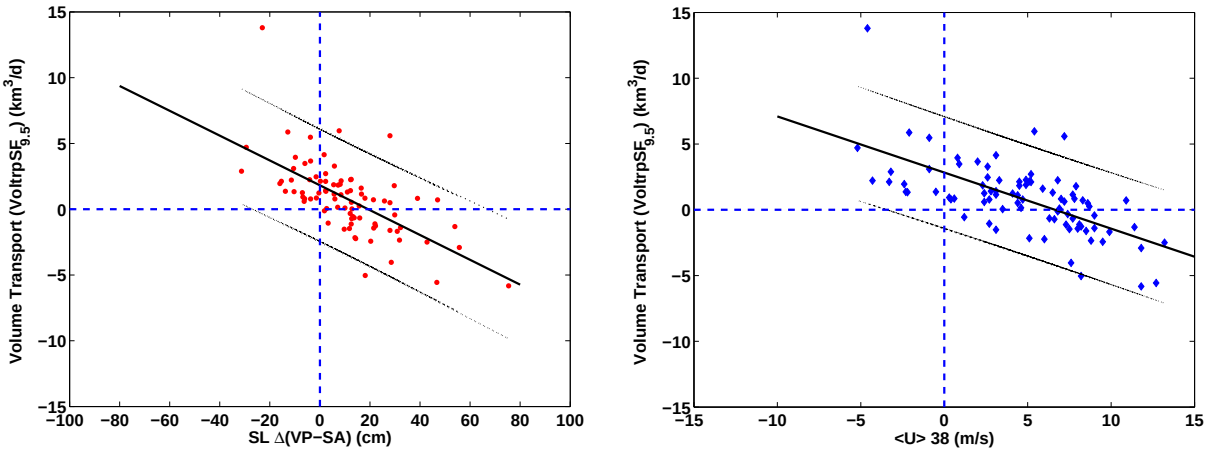

A B

Figure 4.32: Regression SL Δ(Ventspils-Sassnitz) with pos./neg. volume transport below 9.5 kg/m^3 Stolpe Channel (VoltrpSF$_{9.5}$) (A); and wind <U>38 (Arkona-Hoburg) with pos./neg. volume transport below 9.5 kg/m^3 Stolpe Channel (VoltrpSF$_{9.5}$) (B). The two fine lines correspond to the 95% confidence interval of the regression line (thick line).

ports (66-71 m) as well as the correlation with the modelled volume transports are nearly the same, the transport volumes of the estimated transports are naturally smaller, due to its restricted volume mass. Modelled volume transports occupy a volume between the 9.5 kg/m^3 density interface and the bottom at 86 m and estimated transports occupy a volume between 66 - 71 m.

Power spectral densities were calculated to see if before discussed fluctuations are also visible in the density spectra of the ADCPs and in the wind. Welch's method of the FFT (fast Fourier transform) was used for both the along-slope and across-slope components of the currents' vertical mean in 65 - 71 m for ADCP SFN and 52 - 71 m for SFS (Fig. 5.10 in the appendix). The frequency spectra of the currents, calculated for hourly values, hourly values with a 12 h low-pass filter and daily averages, showed a very similar behaviour for low frequencies. Comparisons with the frequency spectrum of the regional wind <U>38 (Fig. 5.9 in the appendix) revealed that the most prominent peak in the spectrum of the wind (3.7 days) was also reflected in the spectra of the along-slope components of SFN (4.0 days) and SFS (3.7 days). This confirms again that the deep current fluctuations are mainly wind driven.

Chapter 5

Discussion and Conclusions

5.1 Deep water intrusions

The exceptional warm inflow event of winter 1997/1998 was investigated with the help of a unique data set combining time series observations from two moorings located at the basin's rim and two high-resolution CTD surveys conducted just before and during the late-stage of the inflow.

The temperature and velocity records obtained at 170 m depth by the moorings NE and SW suggest an inflow period from end of November 1997 to start of May 1998 at mooring NE, and from December 1997 to the end of May 1998 for mooring SW. Highest temperatures were measured between mid and end of March. The inflow occurred in several pulses of warm water, associated with strongly enhanced current velocities. Correlations of temperature and velocity data at the two stations suggest that signals detected between NE and SW travel with a speed of approximately 0.03 m/s along isobaths. Amplitudes of both temperature and velocity signals had significantly decreased by the time the signal arrived at position SW. During the pulses, velocities are roughly aligned with the local topography. However, it is important to point out that the measurements were conducted about 50 m above the bottom, i.e. possibly outside dense bottom gravity currents.

Notable differences were observed between the strong inflow in 1993, and the inflow discussed here. The 1993 inflow analysed by Zhurbas and Paka (1997), Zhurbas and Paka (1999) and Kuzmina et al. (2005) was a cold water inflow with intrusions interleaving in and below the halocline. Inflowing water was found only above 180 m at the eastern rim of the EGB, i.e. approximately 70 m above the deepest part of the basin. In contrast, the warm inflow of the winter 1997/1998 entirely replaced the deep water in the EGB. In addition, the inflow in form of

warm-water intrusions dominated the hydrography in and below the halocline at intermediate depths. The advective creation of temperature variance on isopycnals in this region was found to be an effective mechanism to also create strong vertical temperature gradients. Although the flow remained stably stratified, due to a strong vertical salinity gradient, the inverse temperature stratification generated this way resulted in stratification parameters favouring diffusive convection. A simple analysis of the intrusions' decay time scale indeed suggests enhanced mixing; however, it is likely that additional turbulent shear mixing due to the intrusions contributes to this. Stratification patches with Turner angles in the diffusive convective regime were strongly localised, often captured only in a single CTD cast. This could be interpreted as a result of distortion of initially spatially coherent intrusions by mesoscale eddies, reported to be omnipresent in the Baltic Proper (Reißmann, 2005).

The diffusivities for salt and heat computed from budgets for the lowest part of the basin are of the order of 10^{-5} m^2/s, and therefore comparable to the values previously found by Axell (1998) using a similar method, and by Lass et al. (2003) using turbulence microstructure observations at a somewhat shallower location in the EGB. An interesting conclusion drawn from this is that the presence of the ongoing inflow activity further up in the water column does apparently not cause a significant increase in mixing in the deep layers. This confirms the ideas of Axell (1998) that deep water mixing is mainly driven by downward radiation of wind generated internal waves, provided that the inflow itself does not generate internal waves. Second, the diffusivities of salt and heat in the deep water were found to be surprisingly similar, a fact that clearly relativizes the importance of double-diffusion for deep water mixing. A likely reason is the prevalence of boundary mixing in the deepest parts of the basin that may cause an important contribution to the net vertical mixing through highly energetic processes occurring at large Reynolds numbers (see e.g. Ledwell and Hickey (1995)). Under such conditions the differences in the molecular diffusivities of salt and heat are negligible, and their effect would probably not be felt in a basin-scale budget. This argument does, however, not contradict the possible importance of double-diffusive effects at shallower depths, where intrusions are observed to be stronger and more frequent, and boundaries are remote.

5.2 Deep boundary currents

The cold and oxygen-rich inflow observed in the Stolpe Channel in May 2006 reached intermediate layers in the EGB in September of the same year, where high oxygen and temperature variations were measured in intermediate layers (100 - 200 m). Temperatures of the hydrographic

cross-sections, conducted in September 2006, agreed well with temperatures measured by the top sensor of all three moorings. The top temperature sensors of all three moorings captured the inflow first, whose lenses of cold water are well recognisable in the hydrographic cross-sections of the EGB.

The two ADCPs SFN and SFS deployed at the outlet of the Stolpe Channel revealed a separation of the water column in the three months temporal mean. Eastward flow predominates in depths between 65 - 71 m at SFN and 52 - 71 m at SFS. Westward flow predominates in the upper layers, above 65 and 52 m, respectively. The general separation of the water column was only destroyed by strong wind events.

Hourly and daily transports, calculated from ADCP measurements between 52 - 71 m on the southern side and 65 - 71 m on the northern side of the Stolpe Channel, agreed well with modelled hourly and daily volume transports below the 9.5 kg/m^3 isopycnal. Due to a very weak density gradient in the model the 9.5 kg/m^3 isopycnal corresponded to 52 - 65 m south-north slope rather than the 7.8 kg/m^3 isopycnal from hydrographic transects. Apart from the weak salinity/ density gradient, the overall salinities and also temperatures were represented well in the model. All larger peaks in estimated hourly and daily volume transports were also captured by the modelled transports, both well correlated with R=0.79.

Pathways of the dense bottom water through the Baltic proper can be derived from cross-correlations between volume transports through the Stolpe Channel at 17.5° E, the Gdansk Basin at 55° N, the Hoburg Channel at 56° N and the salt content of the EGB: Highest correlations implied that water from the Stolpe Channel most often takes the direct pathway, transporting water directly into the EGB. Water masses that are re-directed into the Gdansk Basin probably re-circulate there before being transported through the northern parts of the Gdansk Basin towards the Hoburg Channel. From there the bottom water is transported directly into the EGB. The circulation between the northern part of the Gdansk Basin and the Hoburg Channel is rather complicated. Not all water masses choose the deepest pathway, but split and travel slightly further east through the northern part of the Gdansk Basin before rejoining in the Hoburg Channel. Similar results were achieved by Krauss and Brügge (1991), Zhurbas et al. (2003) and Zhurbas et al. (2008) who modelled the deep water flow from the Stolpe Channel and the Bornholm Deep for different wind directions. For winds from the north dense bottom water choose the deepest pathway into the EGB. For easterly, and north-northwesterly winds some parts of the dense water were diverted into the Gdansk Basin instead of the deepest pathway into the EGB. During the deployment period of the ADCPs the wind direction of the regional wind (<U38>,<V>38) across the Baltic Proper mainly came from a northwesterly direction

and only turned towards southwesterly after the 15 November 2006. Meier (2007) experienced a separation of the dense water in his model results when leaving the Stolpe Channel, where one part chose the deepest pathway towards the EGB while the other travelled towards the Gdansk Basin.

The position of the Hoburg Channel transect in the model was not ideally chosen for the budget calculations. In its current position (see Fig. 4.18) the eastern end of the transect catches a large eddy with re-circulating water masses, thus creating artificially larger transports. Ideally the transect should cover at least the area between the 50 m isobath to create good boundary conditions for the mass balance. For the above mentioned reasons the transect at 56°N is not taken into an account in the discussions apart from the above mentioned cross-correlations.

Volume transports computed by Krauss and Brügge (1991) through the Stolpe Channel for winds from the north amounted to 30 - 40 km^3/d in the mid layers and 20 km^3/d in the bottom layer. For winds from the east transport volumes produced similar results, but magnitudes are halved. In this study peaks in eastward volume transports reached between 5 and 10 km^3/d mainly for winds from a northwesterly direction. Only once a strong wind from north-northeast created a volume transport of 15 km^3/d. Comparisons between volume transports from this study and transports acquired by Krauss and Brügge (1991) are suitable only to a limited extent, since Krauss and Brügge (1991) used idealised wind conditions in their study with continuous winds from a given directions, whereas this study uses realistic wind conditions with fluctuating winds. Naturally, transports resulting from constant winds achieve higher magnitudes than transports from fluctuating winds. Volume transports estimated below the 7.9 kg/m^3 isopycnal by Borenäs et al. (2007), ranging from 0.32 - 1.69 km^3/d, are more in the order of magnitude of the transports calculated in this study. Kouts and Omstedt (1993) estimated a transport of 2.16 km^3/d with an average salinity of 14 g/kg, which are still in the vicinity of estimated transports from the ADCPs.

Fluctuating winds blowing over the Baltic Proper account for the observed pulse-like deep water currents in the Stolpe Channel. As described by Krauss and Brügge (1991) it was observed that the surface layer and consequential the sea level are acting in the same direction as the wind. The deep layer, however, acts in the opposite direction. Although, during periods of, for example, low eastward winds (the wind was rotated by 180 ° to match the currents), eastward currents were observed, where westward currents would be expected instead to match the theory. Krauss and Brügge (1991) concluded that a wind blowing constantly in a certain directions produces a counter current in the lower or bottom layer. By switching the wind off in their model the strong directional transport broke down into eddies and topographically controlled

irregular motions. This, however could not be observed in the ADCP data.

From the correlations below, the following flow mechanism can be derived: The regional wind steers the sea level (correlation between the wind <U>38 and sea level difference: R= 0.89) and to a smaller extend influences a counter flow of the deep currents between 66 - 71 m (correlation between <U>38 and <u>SFN/SFS(66-71): R= -0.63). The deep current is more influenced by changes in the sea level (correlation between SL Δ(VP-SA) and <u>SFN/SFS(66-71): R= -0.68). Correlations of the sea level difference with estimated transports between 66 - 71 m and modelled transports below the 9.5 kg/m^3 isopycnal are all slightly less correlated (R= -0.65) than the deep velocities. Separate correlations of each ADCP with the regional wind and sea level difference reveal a stronger influence of the wind in the upper layer on the norther side of the channel, while on the southern side the Ekman transport induced by the Coriolis force is predominant.

Pulse-like currents in the Stolpe Channel are partly driven by the regional wind, i.e. up to 50 % and partly driven by sloping density gradients of dense water masses in the bottom of the channel and therefore resulting geostrophic currents. The height of the eastward flow's upper boundary at SFN (65 m depth) and SFS (52 m) was similar to the slope of the salinity/ density gradient observed in the hydrographic cross-sections. Resulting effects of a sloping density gradient on bottom currents was studied by Paka et al. (1998) and confirm their observations that the current fluctuations are density driven, when wind velocities are low. The frequency spectra of the along-slope current of SFN and SFS reveal that the 2 - 4 day long current fluctuations originate from changes in the regional wind. Each of these fluctuations transport a volume of around 1.78 $\pm$ 1.15 km^3/d eastwards. These 2 - 4 day long fluctuations transport nearly the same amount in a single event as the 3-monthly mean of 0.75 $\pm$ 2.32 km^3/d from estimated transports (0.81 $\pm$ 3.15 km^3/d from modelled transports) and are essential for the ventilation of the deep EGB. Comparisons of the regional wind's frequency spectrum with the frequency spectra of the ADCPs show a reflection of its most prominent peak in the spectrum of the wind (3.7 days) in the spectra of the deep along-slope components of SFN (4.0 days), SFS (3.7 days), in the across-slope component of the three current meters in the EGB and in the along-slope components of the mid and bottom sensor of mooring NE, in mooring SW and in the sea level fluctuations of the Landsort gauge observed by Hagen and Feistel (2004).

5.3 Future Outlook

To catch the spatial dimensions intrusions and their effects on mixing, comprehensive microstructure measurements in intermediate layers and bottom boundary layers would be useful.

For operational purposes a simple estimation of volume transports can be deducted from linear regressions of the regional wind and sea level differences in the Baltic Proper. In cases where realistic model simulations of the deep Baltic Sea are set up to reproduce and substitute observations, a high temporal resolution is crucial to obtain adequate results. Modelled hourly and daily volume and salt transports through the Stolpe Channel (available from June 2006 to June 2007) reproduce these 2 - 4 day fluctuations very well. Whereas the 5-day mean volume transport from the 7 year data set (2002 - 2009) of the Stolpe Channel, Gdansk Basin and Hoburg Channel are not able to resolve these fluctuations. Not only short term fluctuations cannot be resolved by the 5-day values, but also volume and salt transport magnitudes in general are highly underestimated (Fig. 4.26), particularly for westward transports. It can be concluded that a high temporal resolution is very desirable for precise model simulations for future projects.

Bibliography

Axell, L. B., 1998. On the variability of Baltic Sea deepwater mixing. Journal of Geophysical Research 103 (C10), 21,667–21,682.

Baines, P. G., 2002. Two-dimensional plumes in stratified environments. J. Fluid Mechanics 471, 315–337.

Beljaars, A. C. M., 1995. The parametrization of surface fluxes in large-scale models under free convection. Quarterly Journal of the Royal Meteorological Society 121, 255–270.

Bennett, J. R., 1974. On the dynamics of wind-driven lake currents. Journal of Physical Oceanography 4, 400–414.

Bergström, S., Carlsson, B., 1993. Hydrology of the Baltic Basin - Inflow of fresh water from rivers and land for the period 1950 - 1990. SMHI Reports Hydrology No. 7, SHMI, Norrköping.

Borenäs, K., Hietala, R., Laanearu, J., Lundberg, P., 2007. Some estimates of the Baltic deepwater transport through the Stolpe Trench. Tellus 59A (2), 238–248.

Brogmus, W., 1952. Eine Revision des Wasserhaushaltes der Ostsee. Kieler Meeresforschungen 9 (1), 15–42.

Csanady, G. T., 1973. Wind-induced barotropic motions in long lakes. Journal of Physical Oceanography 3, 429–438.

Elken, J., 1996. Deep water overflow, circulation and vertical exchange in the Baltic Proper. Report Series No. 6, Estonian Marine Institute, Tallinn.

Feistel, R., Hagen, E., 1995. On the GIBBS thermodynamic potential of seawater. Progress in Oceanography 36 (4), 249–327.

Feistel, R., Matthäus, W., Hagen, E., 2003a. Temporal and spatial evolution of the Baltic deep water renewal in spring 2003. Oceanologia 45 (4), 623–642.

Feistel, R., Nausch, G., Hagen, E., 2003b. The Baltic inflow of autumn 2001. In Festschrift zum 65. Geburtstag von Wolfgang Matthäus (eds W. Fennel and B. Hentzsch). Meereswissenschaftliche Berichte No. 54, Institut für Ostseeforschung, Warnemünde.

Feistel, R., Nausch, G., Hagen, E., 2006. Unusual Baltic inflow activity in 2002-2003 and varying deep-water properties. Oceanologia 48 (S), 21–35.

Feistel, R., Nausch, G., Matthäus, W., Łysiak-Pastuszak, E., Seifert, T., Sehested, I. S. H. I., Mohrholz, V., Krüger, S., Buch, E., Hagen, E., 2004. Background data to the exceptionally warm inflow into the Baltic Sea in late summer of 2002. Marine Science Reports No. 58, Baltic Sea Research Institute, Warnemünde.

Feistel, R., Nausch, G., Mohrholz, V., Łysiak-Pastuszak, E., Seifert, T., Matthäus, W., Krüger, S., Hansen, I. S., 2003c. Warm waters of summer 2002 in the deep Baltic Proper. Oceanologia 45 (4), 571–592.

Fennel, W., 1986. On the dynamics of coastal jets. In: Rapp. P.-v. Réun. Cons. int. Explor. Mer 186. pp. 31–37.

Fennel, W., Seifert, T., Kayser, B., 1991. Rossby radii and phase speeds in the Baltic Sea. Continental Shelf Research 11 (1), 23–36.

Fischer, H., Matthäus, W., 1996. The importance of the Drogden Sill in the Sound for major Baltic inflows. Journal of Marine Systems 9 (3-4), 137–157.

Franck, H., Matthäus, W., Sammler, R., 1987. Major inflows of saline water into the baltic sea during the present century. Gerlands Beitr. zur Geophysik 96, 517–531.

Griffies, S. M., Hallberg, R. W., 2000. Biharmonic Friction with a Smagorinsky-Like Viscosity for Use in Large-Scale Eddy-Permitting Ocean Models. Monthly Weather Review 128, 2935–2946.

Griffies, S. M., Harrison, M. J., Pacanowski, R. C., Rosati, 2004. A Technical Guide to MOM4. Princeton, USA.

Griffies, S. M., Pacanowski, R. C., Schmidt, M., Balaji, V., 2001. Tracer conservation with an explicit free surface method for z-coordinate ocean models. Monthly Weather Review 129, 1081–1098.

Hagen, E., 2004. Beobachtungen fluktuierender Randströme im Östlichen Gotlandbecken der Ostsee. In: Meeresumwelt-Symposium 2004. Bundesamt für Seeschifffahrt und Hydrographie, Hamburg, pp. 127–138.

Hagen, E., Feistel, R., 2001. Spreading of Baltic deep water: A case study for the winter 1997-1998. Marine Science Reports No. 45, Baltic Sea Research Institute, Warnemünde.

Hagen, E., Feistel, R., 2004. Observations of low-frequency current fluctuations in the deep water of the Eastern Gotland Basin/Baltic Sea. Journal of Geophysical Research 109 (C03044), doi:10.1029/2003JC002017.

Hagen, E., Seifert, T., 2009. Tiefe Randströmungen im Östlichen Gotland Becken der Ostsee. Final project report, Leibniz Institute for Baltic Sea Research.

Hela, I., 1944. Über die Schwankungen des Wasserstandes in der Ostsee mit besonderer Berücksichtigung des Wasseraustausches durch die dänischen Gewässer. Annales Academiæ Scientiarum Fennicæ A, Mathematica-Physica 28, 1–108.

HELCOM, 1993. First Assessment of the State of the Coastal Waters of the Baltic Sea. In: Baltic Sea Environment Proceedings. Baltic Marine Environment Protection Commission, Helsinki, no. 54.

HELCOM, 2009. Total and regional Runoff to the Baltic Sea. Internet, http://www.helcom.fi/BSAP_assessment/ifs/ifs2009/en_GB/Runoff.

Huppert, H. E., 1971. On the stability of double-diffusive layers. Deep-Sea Research 18 (10), 1005–1022.

Jackett, D., McDougall, T. J., Feistel, R., Wright, D. G., Griffies, S. M., 2006. Algorithms for density, potential temperature, conservative temperature, and the freezing temperature of seawater. Journal of Atmospheric Ocean Technology 23 (12), 1709–1728.

Jacobsen, T. S., 1980. Sea water exchange of the Baltic - measurements and methods. The Belt Project. Tech. rep., National Agency of Environmental Protection, Denmark.

Janssen, F., Schrum, C., Backhaus, J. O., 1999. A climatological dataset of temperature and salinity for the North Sea and the Baltic Sea. Deutsche Hydrografische Zeitschrift Supp. 9.

Knudsen, M., 1900. Ein hydrographischer Lehrsatz. Annalen der Hydrographie und Maritimen Meteorologie 28 (7), 316–320.

Kouts, T., Omstedt, A., 1993. Deep water exchange in the Baltic Proper. Tellus 45A, 311–324.

Krauss, W., 1979. A semispectral model for the computation of meoscale processes in a stratified channel of variable depth. Deutsche Hydrografische Zeitschrift 32, 173–189.

Krauss, W., Brügge, B., 1991. Wind-produced water exchange between the deep basins of the Baltic Sea. Journal of Physical Oceanography 21 (3), 373–384.

Kuzmina, N., Rudels, B., Stipa, T., Zhurbas, V., 2005. The Structure and Driving Mechanism of the Baltic Intrusions. Journal of Physical Oceanography 35 (6), 1120–1137.

Large, W. G., McWilliams, J. C., Doney, S. C., 1994. Oceanic vertical mixing: a review and a model with a nonlocal boundary layer parameterization. Review of Geophysics 32, 363–403.

Lass, H. U., Prandke, H., Liljebladh, B., 2003. Dissipation in the Baltic Proper during winter stratification. Journal of Geophysical Research 108 (C6), 3187, doi:10.1029/2002JC001401.

Ledwell, J. R., Hickey, B. M., 1995. Evidence for enhanced boundary mixing in the Santa Monica Basin. Journal of Geophysical Research 100 (C10), 20,665–20,679.

Lehmann, A., Hinrichsen, H.-H., 2000. On the wind driven and thermohaline circulation of the Baltic Sea. Physics and Chemistry of the Earth (B) 25 (2), 183–189.

Matthäus, W., 1984. Climatic and seasonal variability of oceanological parameters in the Baltic Sea. In: Beiträge zur Meereskunde. pp. 29–49, h. 51.

Matthäus, W., 1993. Major inflows of highly saline water into the Baltic Sea - A review. In: paper presented at Statutory Meeting of International Council for Exploration of Sea. Int. Counc. for the Explor. of the Sea, Dublin, Ireland, Sept. 23 to Oct. 1,1993, p. 10 pp.

Matthäus, W., Franck, H., 1992. Characteristics of major Baltic inflows - a statistical analysis. Continental Shelf Research 12, 1375–1400.

Matthäus, W., Lass, H. U., Francke, E., Schwabe, R., 1983. Zur veränderlichkeit des volumen- und salztransports über die sarsser schwelle. Gerlands Beitr. zur Geophysik 92, 407–420.

Matthäus, W., Nehring, D., Feistel, R., Nausch, G., Mohrholz, V., Lass, H. U., 2008. The Inflow of Highly Saline Water into the Baltic Sea. In: State and Evolution of the Baltic Sea, 1952-2005. Ed. by R. Feistel, G. Nausch and N. Wasmund. John Wiley & Sons, Inc. Hoboken, New Jersey, pp. 265–309.

Meier, H. E. M., 2007. Modeling the pathways and ages of inflowing salt- and freshwater in the Baltic Sea. Estuarine, Coastal and Shelf Science 74, 610–627.

Meier, H. E. M., Kauker, F., 2003. Sensitivity of the Baltic Sea salinity to the freshwater supply. Climate Research 24, 231–242.

Meier, H. E. M., Kauker, F., 2003b. Modeling decadal variability of the Baltic Sea: 2. Role of freshwater inflow and large-scale atmospheric circulation for salinity. Journal of Geophysical Research 108 (C11,3368), doi:10.1029/2003JC001799.

Millero, F., Feistel, R., Wright, D. G., McDougall, T., 2008. The composition of standard seawater and the definition of the reference-composition salinity scale. Deep-Sea Research I 55, 50–72.

Mohrholz, V., Dutz, J., Kraus, G., 2006. The impacts of exceptionally warm summer inflow events on the environmental conditions in the Bornholm Basin. Journal of Marine Systems 60, 285–301.

Omstedt, A., Axell, L. B., 1998. Modeling the seasonal, interannual and long-term variations of salinity and termperature in the Baltic Proper. Tellus 50A, 637–652.

Özgökmen, T. M., Fischer, P. F., Johns, W. E., 2006. Product water mass formation by turbulent density currents from a high-order nonhydrostatic spectral element model. Ocean Modelling 12, 237–267.

Paka, V. T., 1996. Thermohaline Structure of Waters at Sections in the Slupsk Furrow. Okeanologiya (Moscow) 36 (2), 207–217.

Paka, V. T., Zurbas, V. M., Golenko, N. N., Stefantsev, L. A., 1998. Effect o the Ekman Transport on the Overflow of Saline Waters through the Slupsk Furrow in the Baltic Sea. Izvestiya, Atmospheric and Oceanic Physics 34 (5), 641–648.

Piechura, J., Beszczyńska-Möller, A., 2004. Inflow waters in the deep regions of the southern Baltic Sea - transport and transformations, corrected version. Oceanologia 46 (1), 113–141.

Pond, S., Pickard, G. L., 1983. Introductory Dynamical Oceanography, 2nd Edition. Pergamon Press, Oxford.

Reissmann, J. H., 1999. Bathymetry of four deep Baltic basins. Ocean Dynamics 51 (4).

Reißmann, J. H., 2002. Integrale Eigenschaften von mesoskaligen Wirbelstrukturen in den tiefen Becken der Ostsee. Meereswissenschaftliche Berichte No. 52, Institut für Ostseeforschung, Warnemünde.

Reißmann, J. H., 2005. An algorithm to detect isolated anomalies in three-dimensional stratified data fields with an application to density fields from four deep basins of the Baltic Sea. Journal of Geophysical Research 110 (C12018), doi:10.1029/2005JC002885.

Reissmann, J. H., 2006. On the representation of regional characteristics by hydrographic measurements at central stations in four deep basins of the Baltic Sea. Ocean Science 2 (1), 71–86, http://www.ocean-sci.net/2/71/2006/.

Reissmann, J. H., Burchard, H., Feistel, R., Hagen, E., Lass, H. U., Mohrholz, V., Nausch, G., Umlauf, L., Wieczorek, G., 2009. Vertical mixing in the Baltic Sea and consequences for eutrophication - a review. Progress in Oceanography 82, 47–80.

Rubio, A., Gomis, D., Jordà, G., Espino, M., 2009. Estimating geostrophic and total velocities from CTD and ADCP data: Intercomparison of different methods. Journal of Marine Systems 77, 61–76.

Ruddick, B., 1983. A practical indicator of the stability of the water column to double-diffusive activity. Deep-Sea Research A 30 (10), 1105–1107.

Samuelsson, M., Stigebrandt, A., 1996. Main characteristics of long-term sea level variability in the Baltic Sea. Tellus 48A, 672–683.

Schinke, H., Matthäus, W., 1998. On the causes of major Baltic inflows - an analysis of long time series. Continental Shelf Research 18, 67–97.

Schmidt, M., Fennel, W., Neumann, T., Seifert, T., 2008. Description of the Baltic Sea with numerical models. In: State and Evolution of the Baltic Sea, 1952-2005. Ed. by R. Feistel, G. Nausch and N. Wasmund. John Wiley & Sons, Inc. Hoboken, New Jersey, pp. 583–624.

Seifert, T., Tauber, F., Kayser, B., 2001. A high resolution spherical grid topography of the Baltic Sea - revised edition. In: Baltic Sea Science Conference, Stockholm, November, 25-29 2001; Poster #147. http://www.io-warnemuende.de/topography-of-the-baltic-sea.html.

Smagorinsky, J., 1963. General circulation experiments with the primitive equations: I. The basic experiment. Monthly Weather Review 91 (3), 99–164.

Smagorinsky, J., 1993. Some historical remarks on the use of nonlinear viscosities. In: Large Eddy simulation of Complex Engineering and Geophysical Flows. Ed. by B. Galperin and S. A. Orszag. Cambridge University Press, pp. 3–36.

Stewart, R. H., 2004. Introduction to Physical Oceanography. Internet, http://www.oceanworld.tamu.edu/resources/ocng_textbook/contents.html, department of Oceanography, Texas A&M University, ©1997-2005.

Stigebrandt, A., 1980. Barotropic and baroclinic response of a semi-enclosed basin to bartropic forcing from the sea. In: Fjord Oceanography. Ed. by H. J. Freeland, D. M. Farmer and C. D. Levings. Plenum, New York, pp. 151–164.

Stigebrandt, A., 1987. A Model for the Vertical Circulation of the Baltic Deep Water. Journal of Physical Oceanography 17 (10), 1772–1785.

Stigebrandt, A., Lass, H. U., Liljebladh, B., Alenius, P., Piechura, J., Hietala, R., Beszczynska, A., 2002. DIAMIX- an experimental study of diapycnal deepwater mixing in the virtually tideless Baltic Sea. Boreal Environment Research 7, 363–369.

Thiel, G., 1938. Strombeobachtungen in der westlichen Ostsee im Juli 1936. Tech. Rep. 58, Aus dem Archiv der Deutschen Seewarte und des Marineobservatoriums.

Turner, J. S., 1965. The coupled turbulent transport of salt and heat across a sharp density interface. Int. J. Heat Mass Transfer 8, 759–767.

Turner, J. S., 1979. Buoyancy Effects in Fluids. Cambridge University Press.

Welander, P., 1974. Two-layer exchange in an Estuary Basin, with special reference to the Baltic Sea. Journal of Physical Oceanography 4 (4), 542–556.

Wieczorek, G., Hagen, E., Umlauf, L., 2008. Eastern Gotland Basin case study of thermal variability in the wake of deep water intrusions. Journal of Marine Systems 74, S65–S79.

Winant, C. D., 2004. Three-Dimensional Wind-Driven Flow in an Elongated, Rotating Basin. Journal of Physical Oceanography 34, 462–476.

Wüst, G., Noodt, E., Hagmeier, E., 1957. Ergebnisse eines hydrographisch-produktionsbiologischen Längsschnitt durch die Ostsee im Sommer 1956. Kieler Meeresforschungen 13, 163–185.

Wyrtki, K., 1954. Der große Salzeinbruch in die Ostsee im November und Dezember 1951. Kieler Meeresforschungen 10, 19–25.

Zhurbas, V., Elken, J., Väli, G., 2008. Pathways of Suspended Particles Released in the Bottom Boundary Layer of the Bornholm Deep, Baltic Sea (Numerical Simulations). In: US/EU-Baltic International Symposium 2008, 27-29 May. 2008 IEEE/OES, Tallin, pp. 1–5, 10.1109/BALTIC.2008.4625495.

Zhurbas, V., Oh, I., Paka, V., 2003. Generation of cyclonic eddies in the Eastern Gotland Basin of the Baltic Sea following dense water inflows: numerical experiments. Journal of Marine Systems 38, 323–336.

Zhurbas, V., Paka, V., 1997. Mesoscale thermohaline variability in the Eastern Gotland Basin following the 1993 major Baltic inflow. Journal of Geophysical Research 102 (C9), 20,917–20,926.

Zhurbas, V., Paka, V., 1999. What drives thermohaline intrusions the Baltic Sea? Journal of Marine Systems 21, 229–241.

Acknowledgement

First and foremost, I would like to thank my advisor, Dr. Eberhard Hagen for his constant support and encouragement on this research project. Then I would like to thank Dr. Torsten Seifert and Dr. Martin Schmidt for their support on the model, providing me with model data and introducing me to Ferret. Without Günter Plüschke, Toralf Heene and the crew of the Professor Albrecht Penck the measuring campaigns would have not been possible. Thanks to the IT department for their support and providing me with data from the IOW data base. Then I would like to thank Dr. Lars Umlauf and my fellow PhD students from room 214 for our fruitful discussions. Then I would like to thank my thesis committee, Dr. Rainer Feistel, Dr. Falk Pollehne and Dr. Klaus Peter Koltermann for their help and advice. Furthermore I would like to thank all other friends and colleagues from my time in Rostock and IOW I haven't mentioned so far. I would like to thank Dr. Birgit Klein for her proof reading and advice. Holger Giese was very helpful in the initial stages of the project and provided me with instrumentation. Dr. Ivan Kuznetsov and Dr. Mayya Gogina helped to get the thesis printed and submitted. Dr. Sunke Schmidtko I would like to thank for his proof reading. In my new work at the Scottish Environment Protection agency my boss Dr. Alan Hills and colleague Dr. Ted Schlicke supported me during the writing up period and thanks to all my other friends at SEPA. I would also like to thank my family and friends I haven't mentioned yet for their moral support and understanding over these years. Thanks to the reviewers and to the Deutsche Forschungsgemeinschaft, who funded this project "Tiefe Randströmungen im Östlichen Gotlandbecken der Ostsee", HA 1900/ 3-1/2.

Appendix

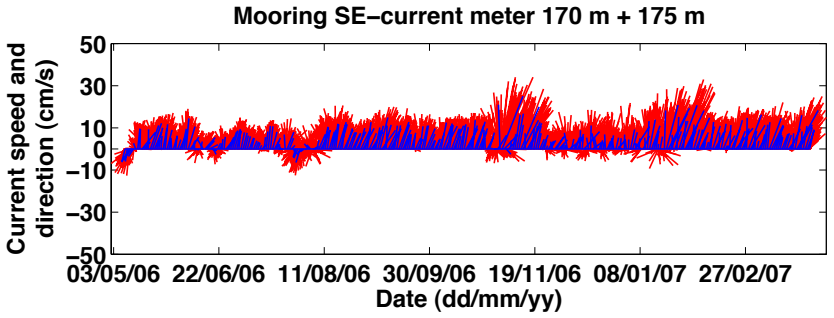

(a) Current meter 175 m

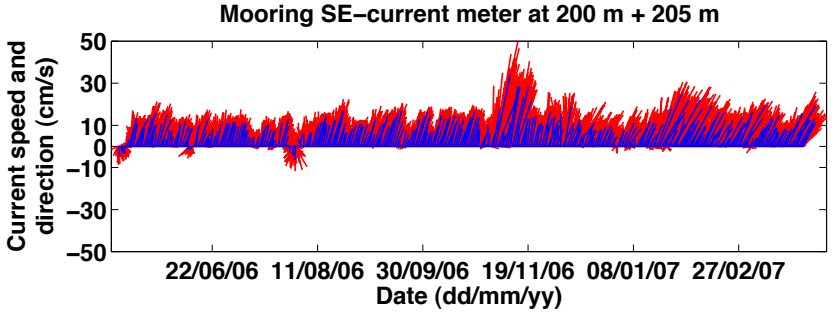

(b) Current meter 200 m

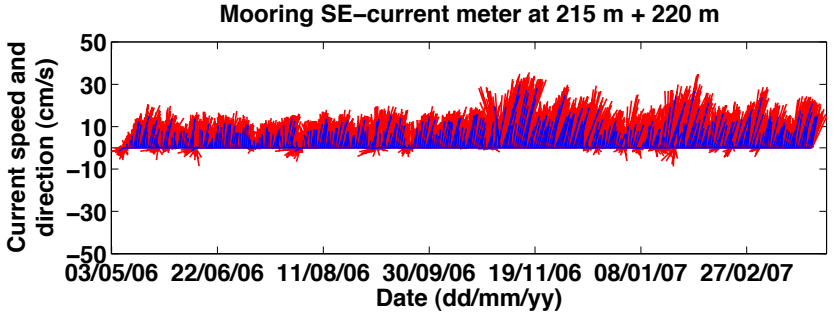

(c) Current meter 220 m

Figure 5.1: Stick plot of currents mooring SE. Hourly values (red), daily values (blue).

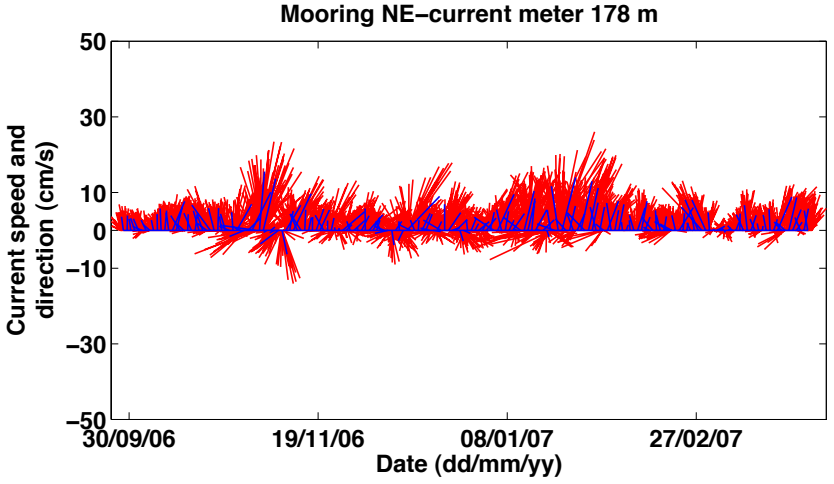

(a) Current meter 178 m

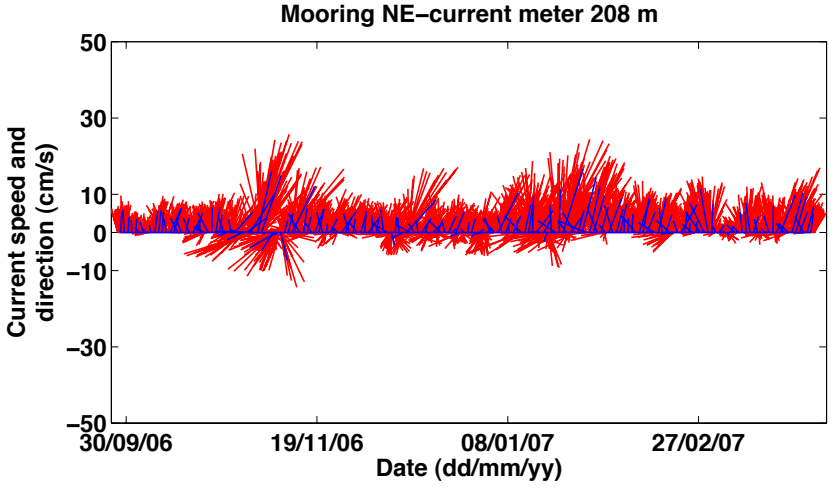

(b) Current meter 208 m

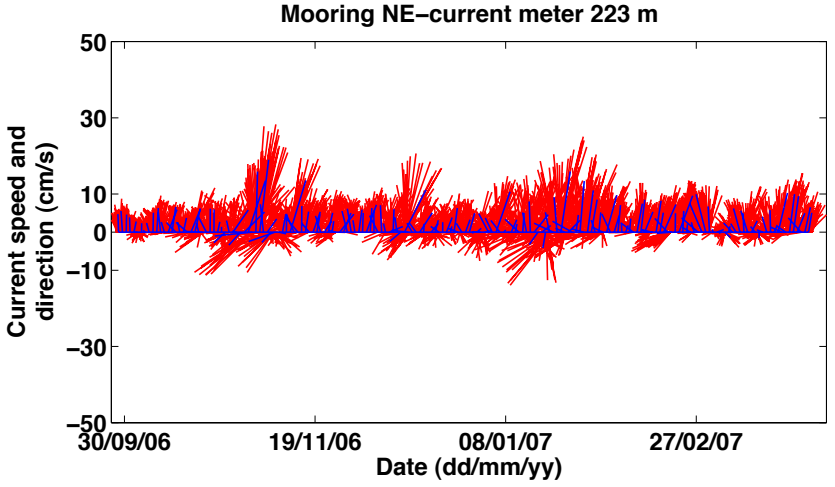

(c) Current meter 223 m

Figure 5.2: Stick plot of currents mooring NE. Hourly values (red), daily values (blue).

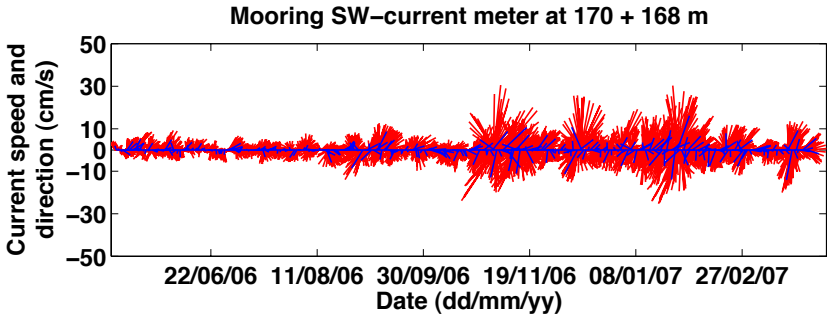

(a) Current meter 105 m

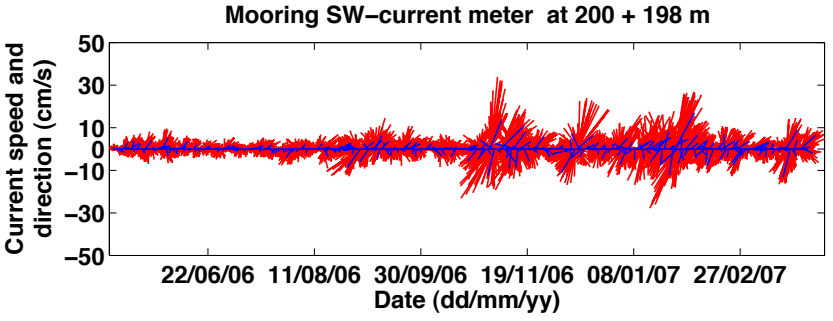

(b) Current meter 205 m

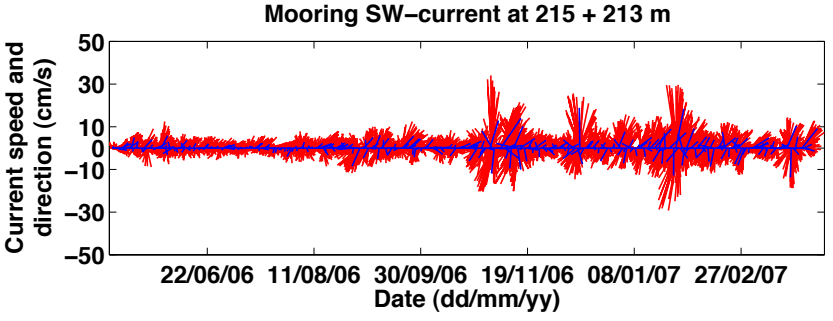

(c) Current meter 215 m

Figure 5.3: Stick plot of currents mooring SW. Hourly values (red), daily values (blue).

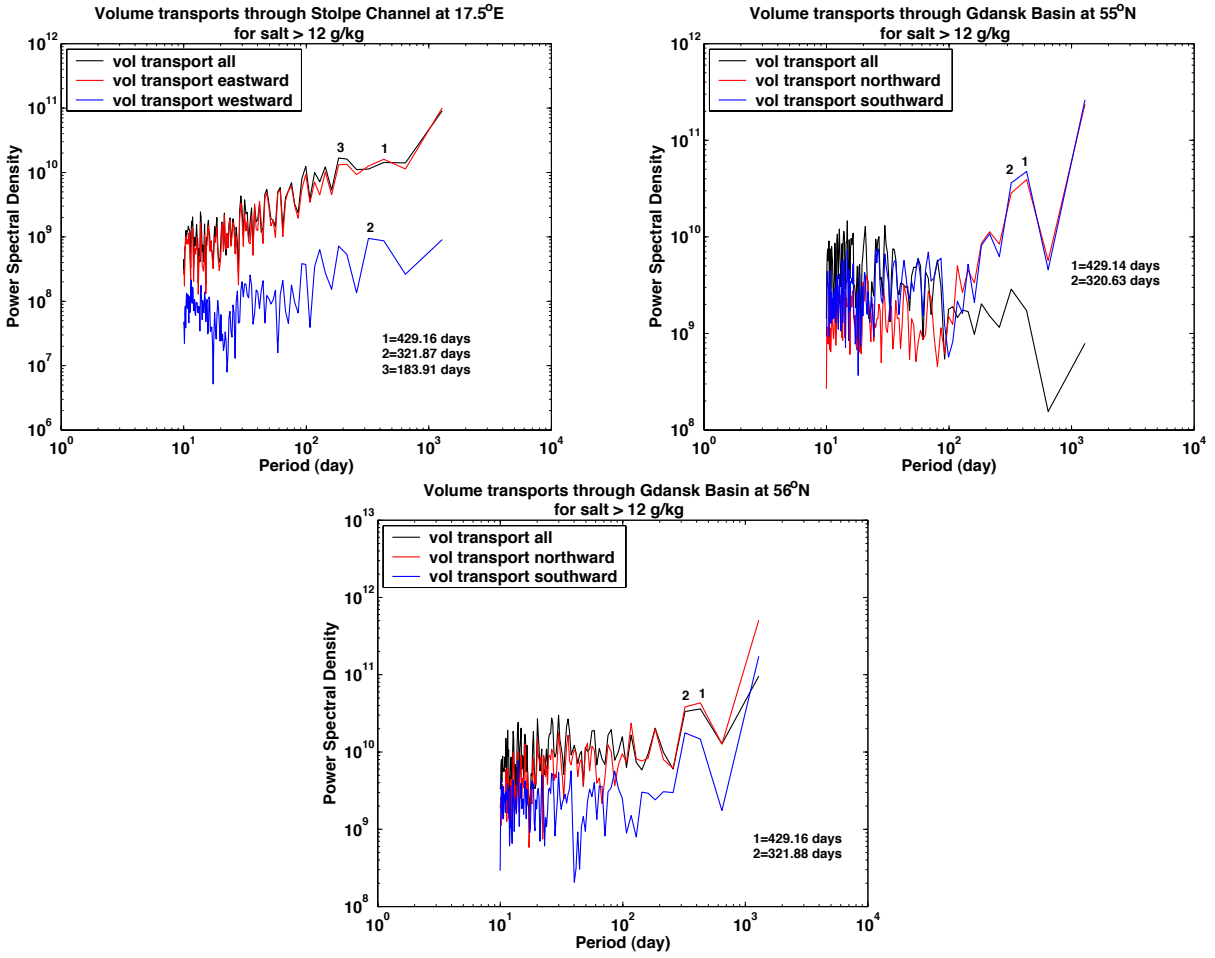

Figure 5.4: Power Spectra of modelled volume transports of the three transects marked in Fig. 4.18. Stolpe Channel in top left panel, Gdansk Basin in top right panel and Hoburg Channel in lower panel.

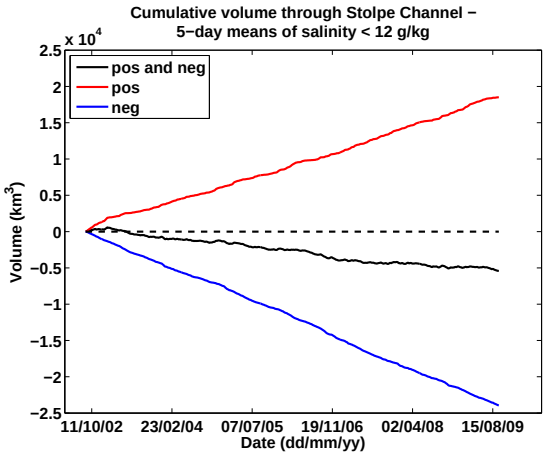

(a) 2002 – 2009

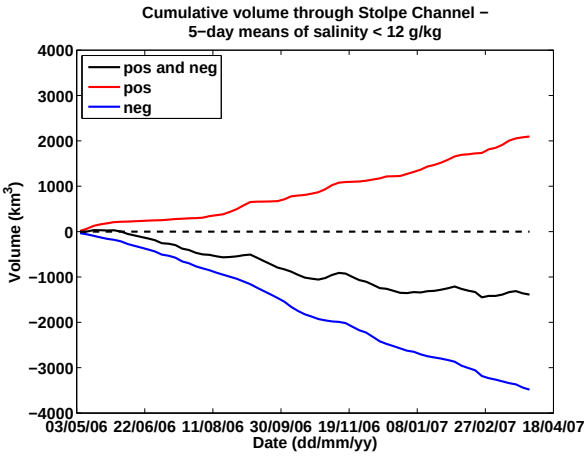

(b) May 2006 – March 2007

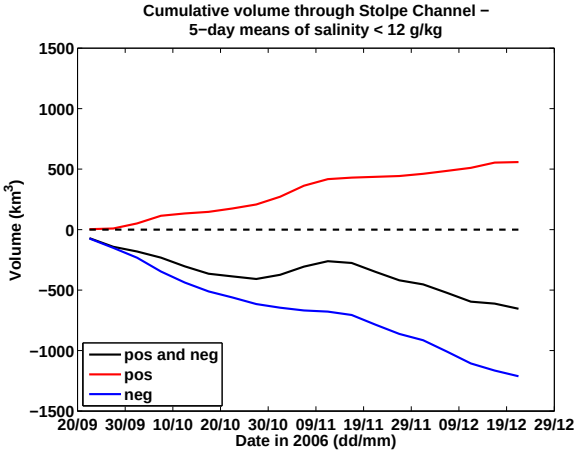

(c) September to December 2006

Figure 5.5: Cumulative positive (eastward, red), negative (westward, blue) and both positive/negative (black) volume (km^3) through Stolpe Channel at 17.5°E for salt < 12 g/kg; position is marked in Fig. 4.18. Note, scales between plots differ.

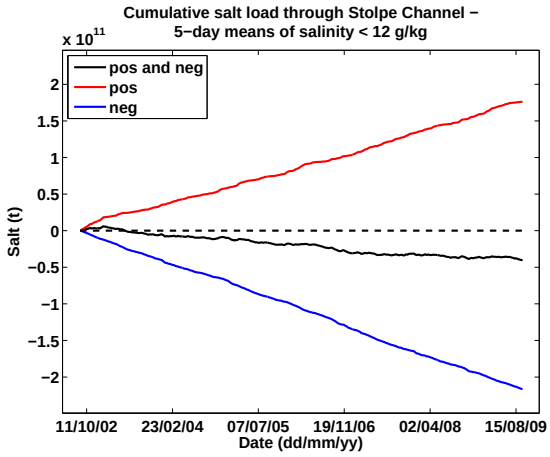

(a) 2002 – 2009

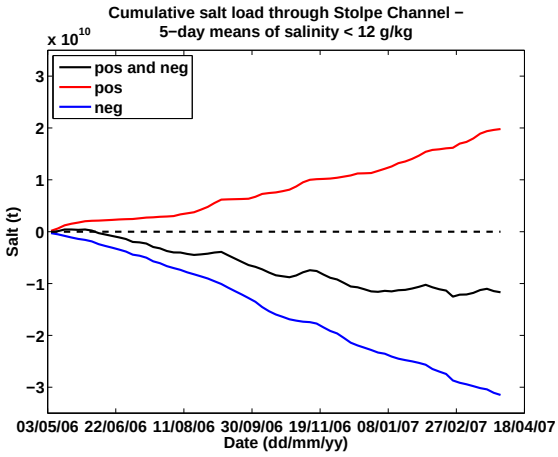

(b) May 2006 – March 2007

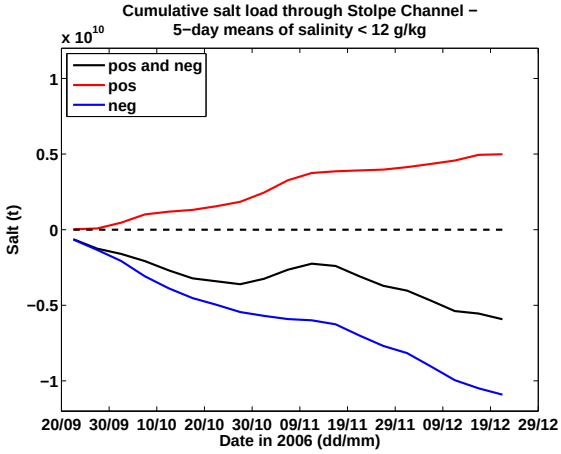

(c) September to December 2006

Figure 5.6: Cumulative positive (eastward, red), negative (westward, blue) and both positive/negative (black) salt load (t) through Stolpe Channel at 17.5°E for salt < 12 g/kg. Note, scales between plots differ.

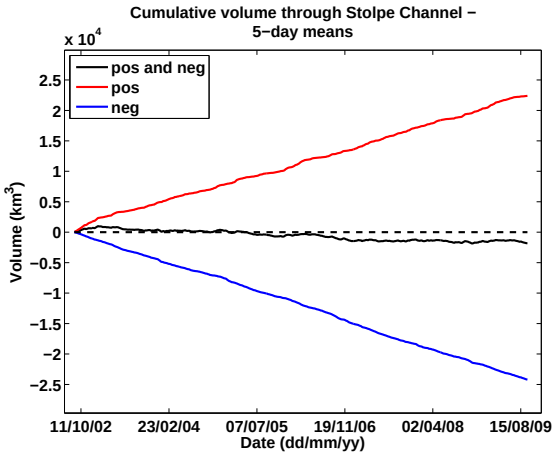

(a) 2002 – 2009

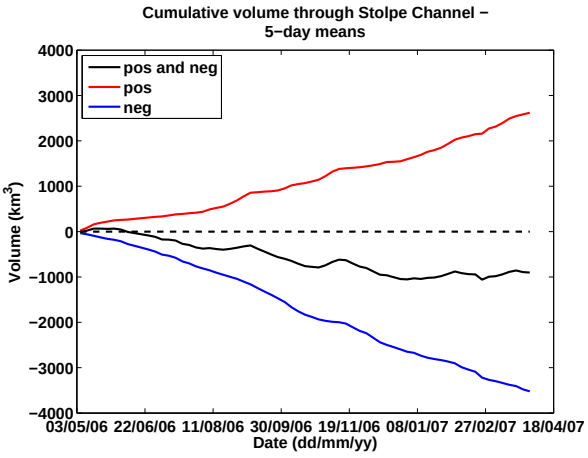

(b) May 2006 – March 2007

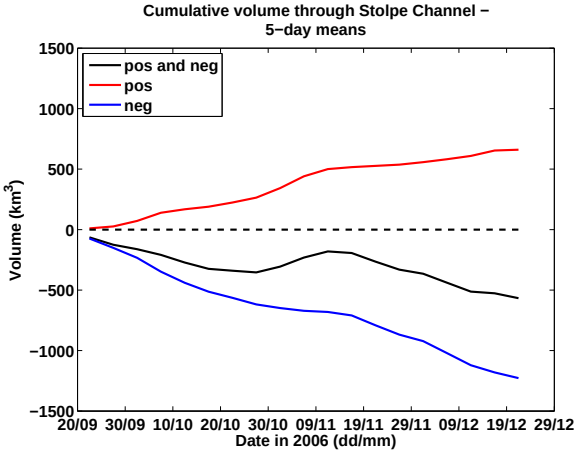

(c) September to December 2006

Figure 5.7: Cumulative positive (eastward, red), negative (westward, blue) and both positive/negative (black) volume (km^3) through Stolpe Channel at 17.5°E for whole water column; position is marked in Fig. 4.18. Note, scales between plots differ.

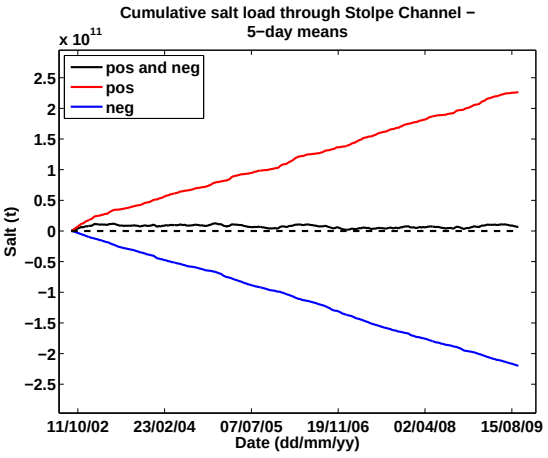

(a) 2002 – 2009

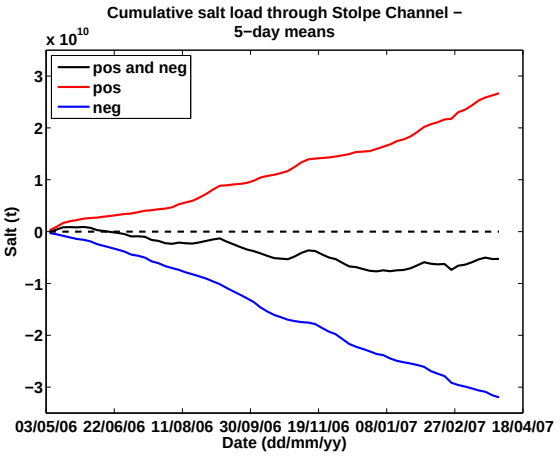

(b) May 2006 – March 2007

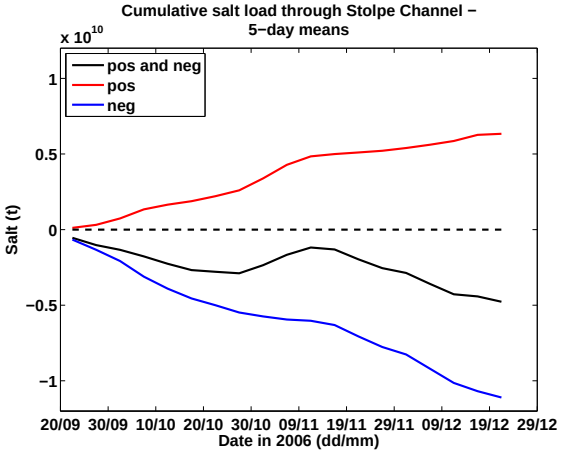

(c) September to December 2006

Figure 5.8: Cumulative positive (eastward, red), negative (westward, blue) and both positive/negative (black) salt load (t) through Stolpe Channel at 17.5°E for whole water column. Note, scales between plots differ.

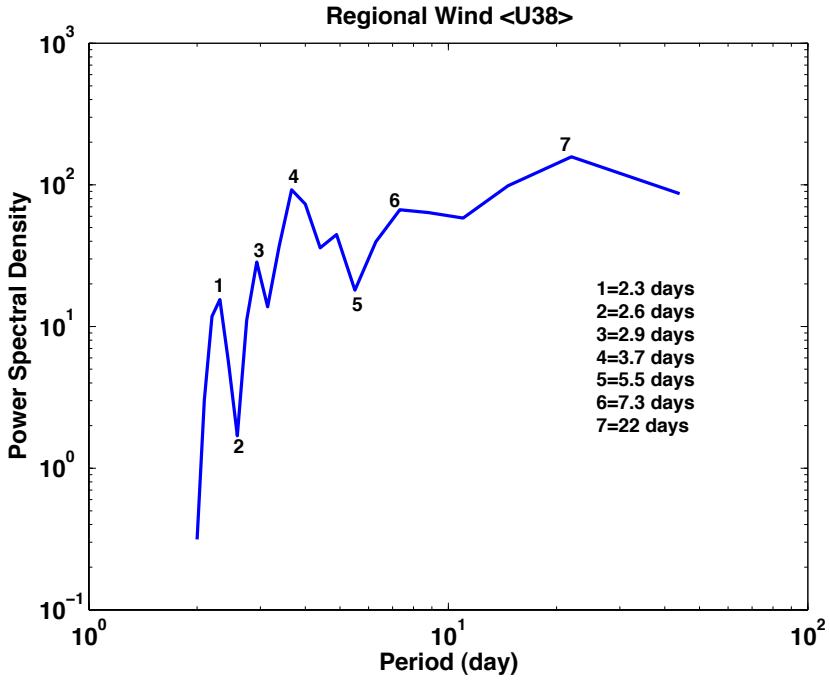

Figure 5.9: Power spectrum of averaged wind <U>38.

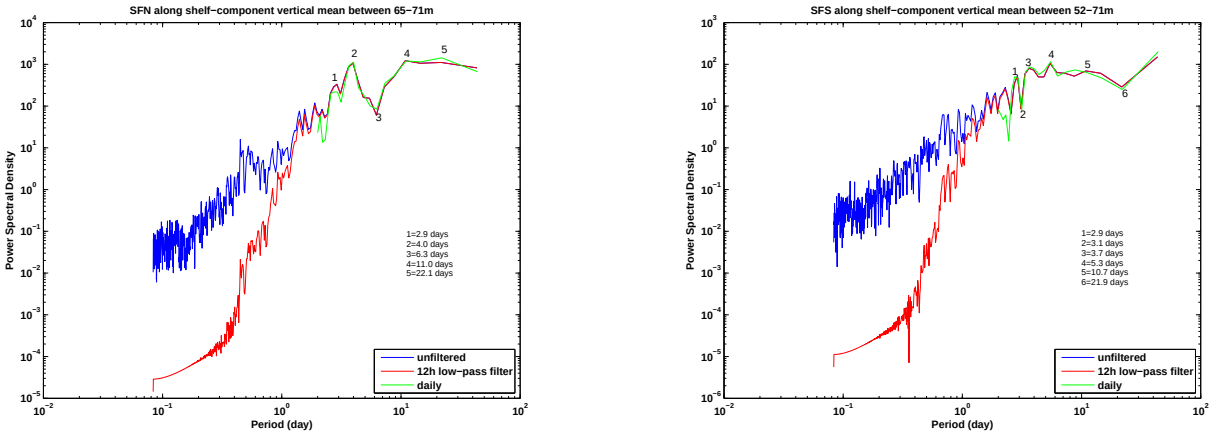

A B

Figure 5.10: The Stolpe Channel: Power spectra of the along-slope vertical mean currents of (A) SFN (between 65-71 m) and (B) SFS (between 52-71 m) for a period from 23 September to 19 December 2006.

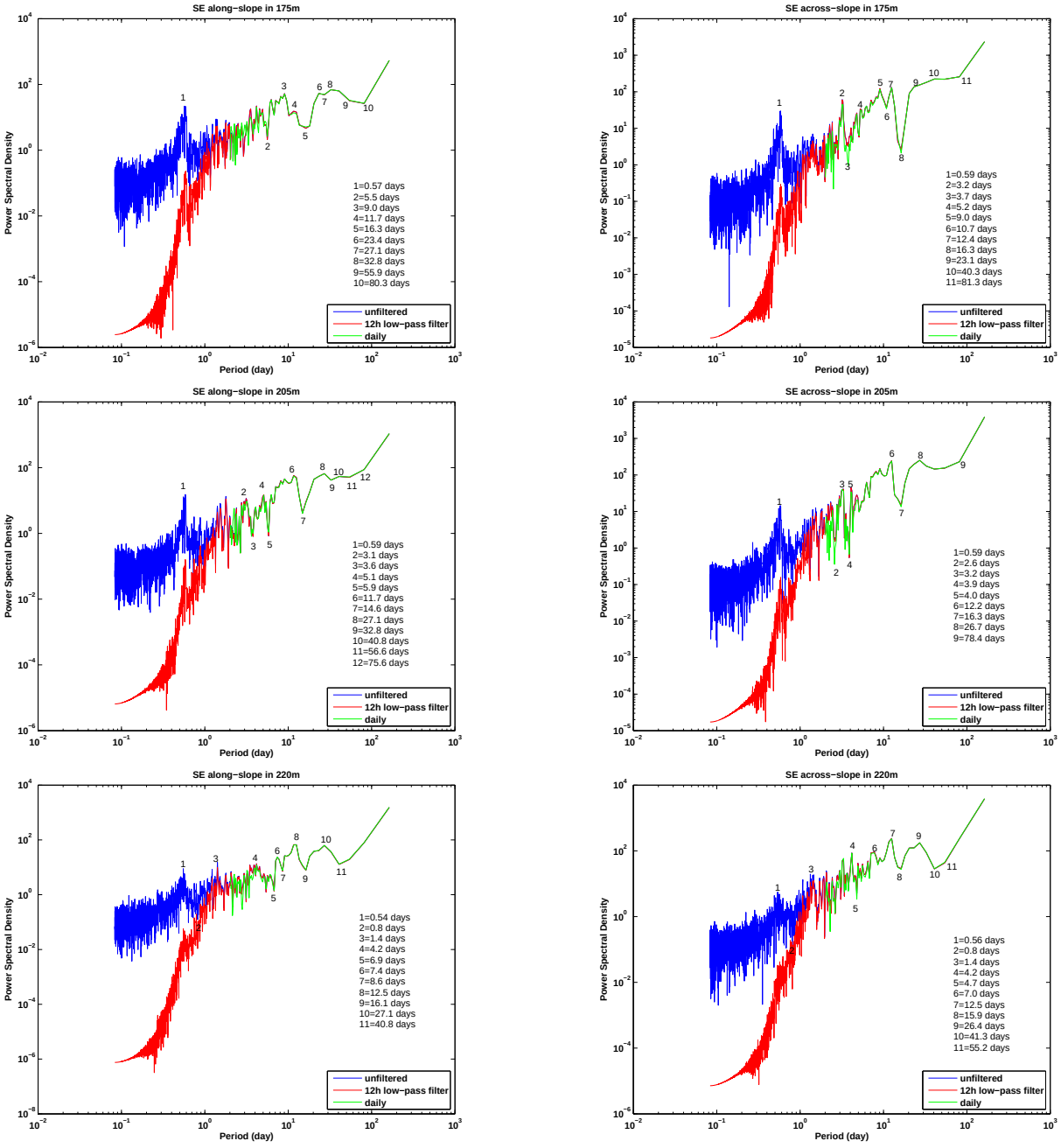

A B

Figure 5.11: Mooring SE: Spectra in 175 m, 205 m and 220 m of the along-slope current component (A) and the across-slope current component (B) for a period from 8 May 2006 to 30 March 2007.

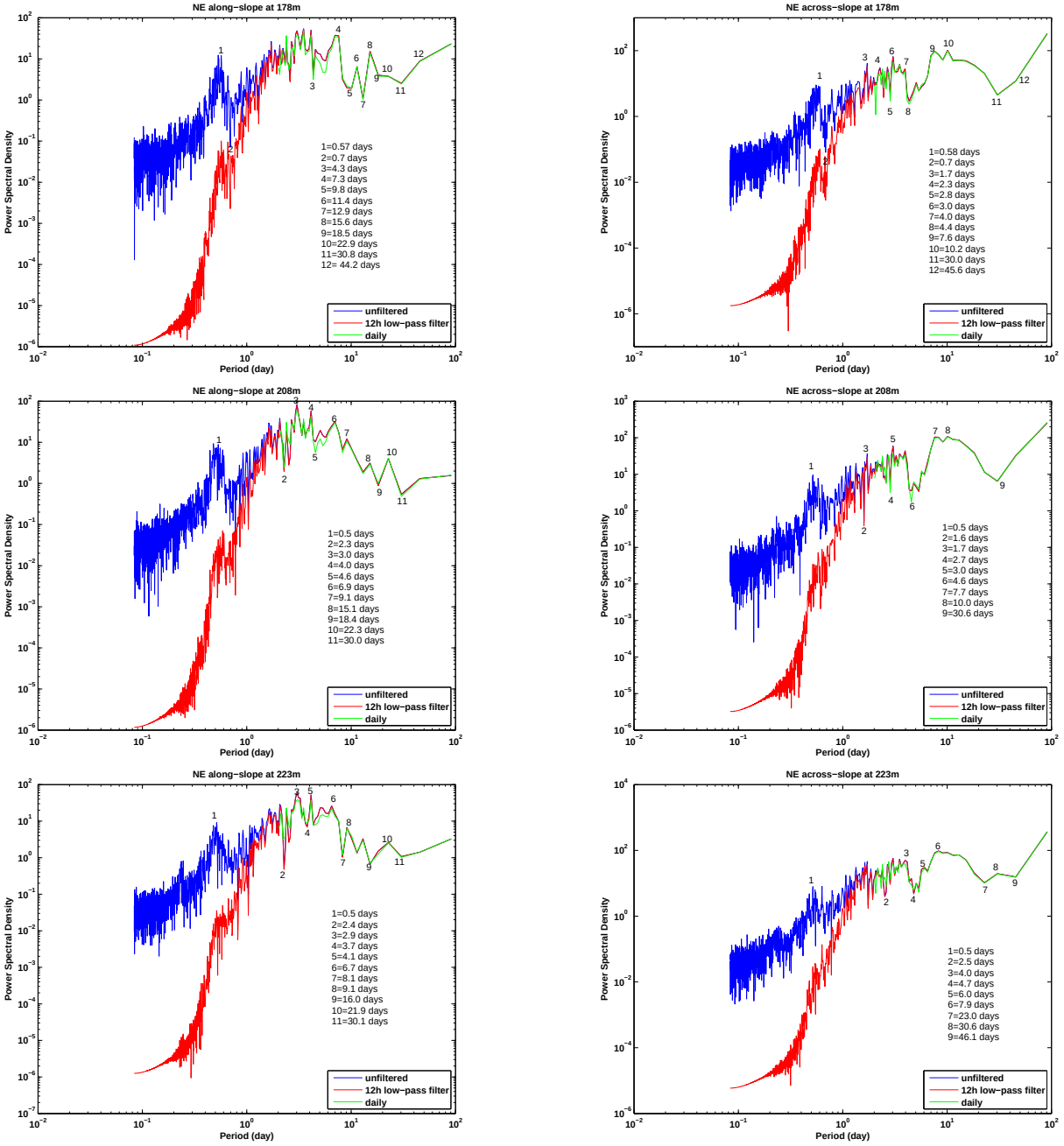

A B

Figure 5.12: Mooring NE: Mooring SE: Spectra in 178 m, 208 m and 223 m of the along-slope current component (A) and the across-slope current component (B) for a period from 28 September 2006 to 29 March 2007.

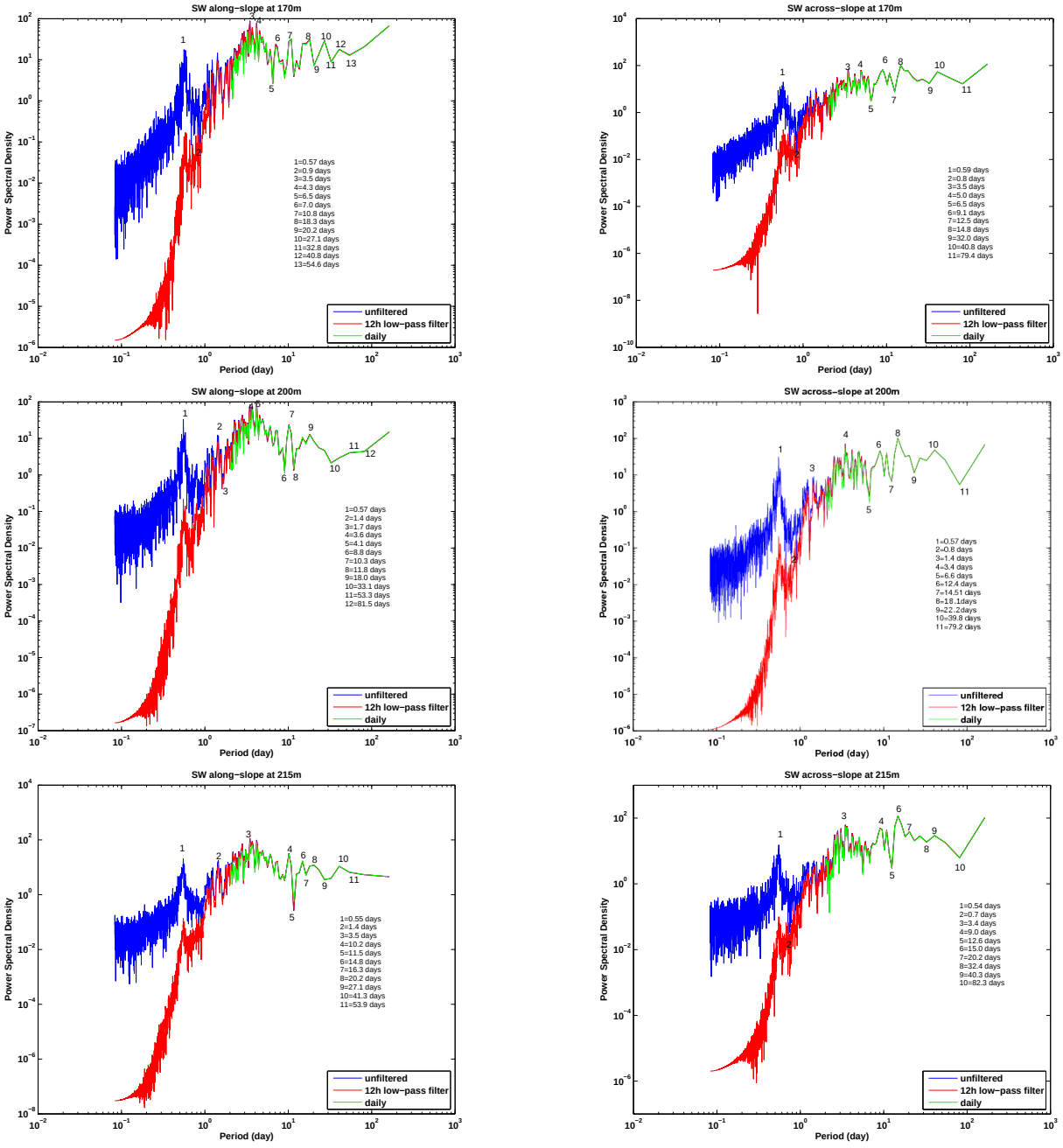

A B

Figure 5.13: Mooring SW: Spectra in 175 m, 205 m and 220 m of the along-slope current component (A) and the across-slope current component (B) for a period from 8 May 2006 to 30 March 2007.